# Advanced diagnostic tools for analysing processes in metal ion batteries

## Atomic force microscopy and positron annihilation spectroscopy for lithium ion and magnesium ion batteries

Legerstee, W.J.

**DOI**
10.4233/uuid:e7cf8afe-2b0b-4260-8308-df5633cecda7

**Publication date**
2025

**Document Version**
Final published version

**Citation (APA)**
Legerstee, W. J. (2025). *Advanced diagnostic tools for analysing processes in metal ion batteries: Atomic force microscopy and positron annihilation spectroscopy for lithium ion and magnesium ion batteries*. [Dissertation (TU Delft), Delft University of Technology]. https://doi.org/10.4233/uuid:e7cf8afe-2b0b-4260-8308-df5633cecda7

**Important note**
To cite this publication, please use the final published version (if applicable).
Please check the document version above.

# Advanced diagnostic tools for analysing processes in metal ion batteries

*Atomic force microscopy and positron annihilation spectroscopy for lithium ion and magnesium ion batteries*

**Walter Legerstee**

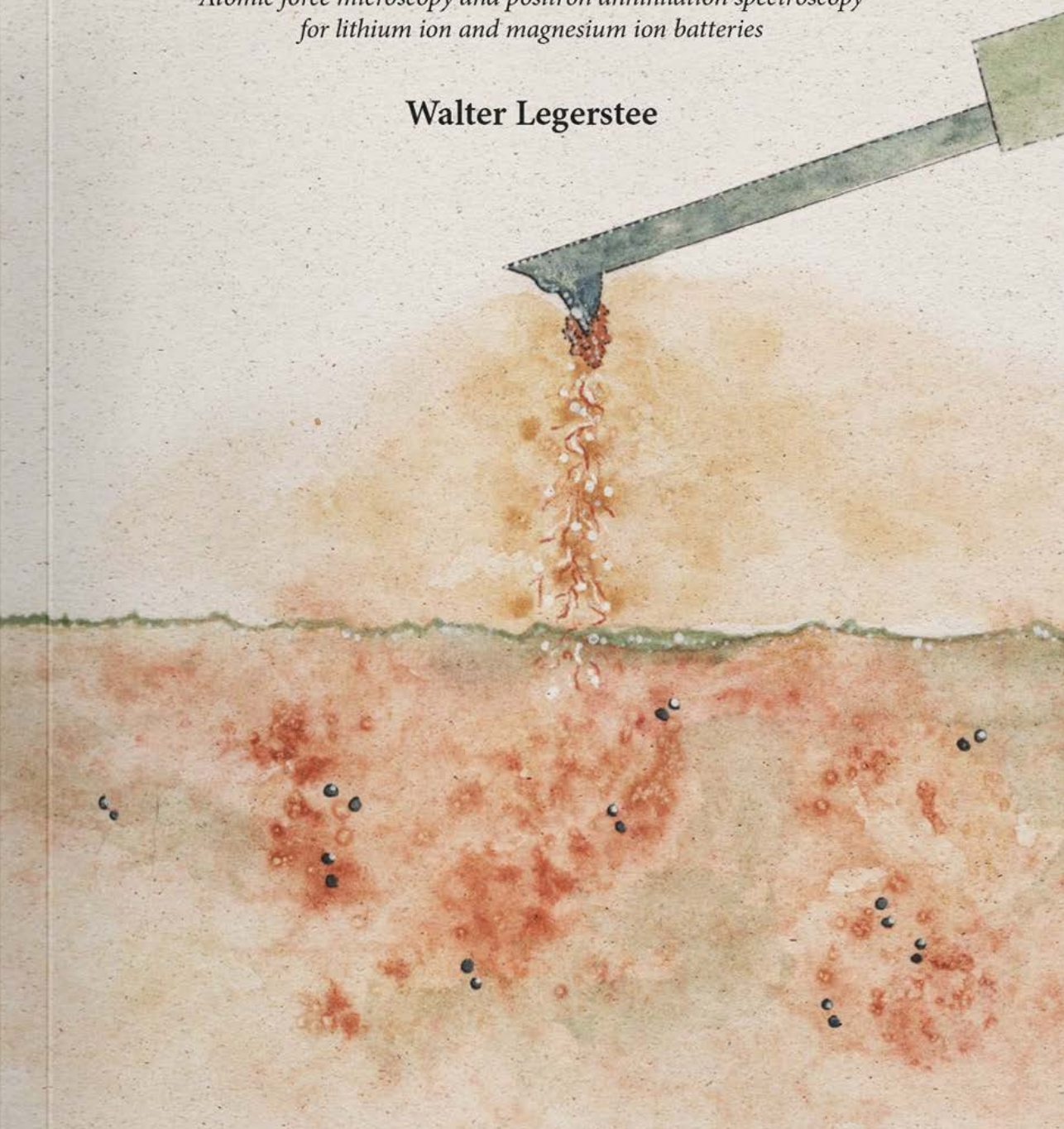

# Advanced diagnostic tools for analysing processes in metal ion batteries

*Atomic force microscopy and positron annihilation spectroscopy for lithium ion and magnesium ion batteries*

**Walter Legerstee**

ISBN: 978-90-835527-0-5

Cover and artwork: © Elma Hogeboom 2025
Layout and design by © Sıla Akçakoca 2025 for GreenThesis
Proudly printed on 100% recycled paper.

GREENTHESIS



A tree has been planted for every copy of this thesis.

# ADVANCED DIAGNOSTIC TOOLS FOR ANALYSING PROCESSES IN METAL ION BATTERIES

## ATOMIC FORCE MICROSCOPY AND POSITRON ANNIHILATION SPECTROSCOPY FOR LITHIUM ION AND MAGNESIUM ION BATTERIES

PROEFSCHRIFT

ter verkrijging van de graad van doctor
aan de Technische Universiteit Delft
op gezag van Rector Magnificus prof.dr.ir.T.H.J.J. van der Hagen,
voorzitter van het College voor Promoties,
in het openbaar te verdedigen op
donderdag 3 juli 2025 om 12:30 uur

door

Walter Jacob LEGERSTEE
Bachelor of Science In Toegepaste Natuurkunde
Technische Hogeschool Rijswijk

Dit proefschrift is goedgekeurd door de promotors

Samenstelling promotiecommisie:

| | |
|---|---|
| Rector Magnificus ` | voorzitter |
| Dr. E. M. Kelder | Technische Universiteit Delft, promotor |
| Prof. dr. E.H. Brück | Technische Universiteit Delft, promotor |

Onafhankelijke leden:

| | |
|---|---|
| Dr. S. W.H. Eijt | Technische Universiteit Delft |
| Dr. Y. Gonzalez-Garzia | Technische Universiteit Delft |
| Prof. dr. ir. A. Urakawa | Technische Universiteit Delft |
| Prof. dr. W. Wieczorek | Warsaw University of Technology, Warsaw, Poland |
| Dr. F. Vullum-Bruer | Sintef, Norway |

Reserve lid:

| | |
|---|---|
| Prof. dr. S. J. Picken | Technische Universiteit Delft |

***"We need a renewables revolution,***
***not a self-destructive fossil fuel resurgence"***

*Antonio Guterres, United Nations Secretary-General,*
*06 February 2023*

# Abbreviations

| | |
|---|---|
| ac-SECM | alternating current Scanning Electrochemical Microscopy |
| AFM | Atomic Force Microscopy |
| AFMAB | Atomic Force Microscope Accessible Battery |
| a-Si | Amorphous silicon |
| CE | Counter electrode |
| $C_d$ | Discharge capacity |
| $C_{max}$ | Maximum capacitance without fracture |
| c-Si | Crystaline silicon |
| DBPAS | Doppler Broadening Positron Annihilation Spectroscopy |
| DMC | Dimethyl carbonate |
| E | Youngs modulus |
| EC | Ethylene carbonate |
| EIS | Electrochemical Impedance Spectroscopy |
| $f_0$ | Resonance frequency of a harmonic oscillating cantilever |
| $f_{Li}$ | Shifted resonance frequency caused by added lithium on the tip |
| $f_n$ | Relative resonance shift |
| FEM | Finite Element Method |
| FFT-EIS | Fast Fourier Transform Electrochemical Impedance Spectroscopy |
| FFT-SEIM | Fast Fourier Transform Scanning Electrochemical Impedance Microscopy |
| $k_{eff}$ | Effective spring constant of an oscillating cantilever |
| KPFM | Kelvin Probe Force Microscopy |
| $LiPF_6$ | Lithium hexafluorophosphate |
| $m_{eff}$ | Effective mass for the first mode of an oscillating cantilever |
| $m_{cantilever}$ | Cantilever mass |
| $m_{li}$ | Mass of the lithium added on the cantilever tip |
| p | Impulse of an electron |
| PAS | Positron Annihilation Spectroscopy |
| ppm | parts per million |
| Q-factor | Quality factor of oscillation |
| $R_c$ | Responsivity |
| RE | Reference electrode |
| SCM | Scanning Capacitance Microscopy |
| SECM | Scanning Electrochemical Microscopy |
| SEIM | Scanning Electrochemical Impedance Microscopy |
| SEM | Scanning Electron Microscopy |
| $S_{ins}$ | Sensitivity |
| S-parameter | Low momentum shape parameter |
| STM | Scanning Tunneling Microscopy |
| UME | Ultra Micro Electrode |
| $\Delta V_{alloying}$ | Volume change due to alloying |
| $V_{pores}$ | Pore volume |
| VEP | Variable Energy Positron beam |
| WE | Working electrode |
| W-parameter | High momentum wing parameter |
| XRD | X-ray differaction |

# TABLE OF CONTENTS

# CHAPTER ONE

*Introduction*

# Introduction

In addition to the unpredictable availability of green energy, the temporary storage of this energy forms an indispensable value to overcome the missing links in the future energy supply chain. In contrast to a fossil energy driven grid, the difference between energy supply and demand will depend on the yield from green sources such as wind turbines, solar cells, tidal energy, etc. Both the availability of energy from these sources and the use of electrical energy undergo significant fluctuations on different time scales: due to seasonal influences throughout the year, difference between weekdays and weekends, as well as throughout the day. Figure 1 gives an example of a daily energy fluctuation caused by differences in wind and solar energy yields over the day. For the differences on a longer time scale, solutions will have to be found at a national or regional level as part of the grid, while the fluctuations on a short time scale can better be accommodated locally, possibly even at a private level. For both storage issues, batteries are an important link between the generation- and usage-fluctuations that affect the grid, but even on a smaller scale for securing and regulating energy availability in an individual home or business.

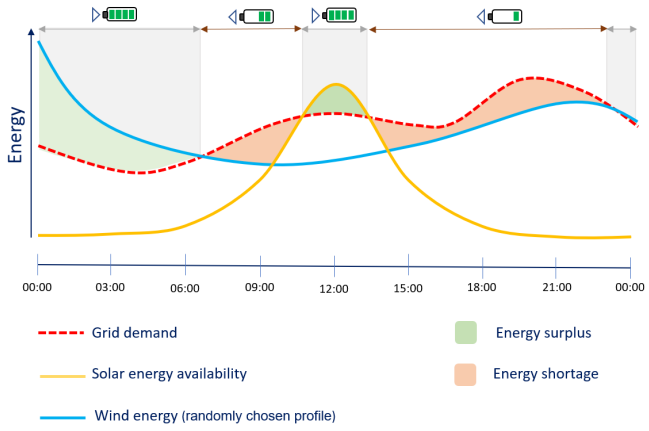


Figure 1.1: example of fluctuations in energy yield and demand over the day

In addition to the need for batteries to moderate the grid, the electrification of transportation is being deployed at a rapid pace, which means that the demand for batteries is high and will continue to grow in the coming years. In order to meet this enormous future need, in addition to increasing the energy density, extend the cycle life and improve the performance of the state of the art batteries, researchers are looking for new battery chemistries and new electrode materials and electrolyte

solutions that are abundant and preferably have a low impact on the environment. To conduct this research, scientists continually use new research methods and measuring techniques that reflect the need to directly monitor processes taking place in the battery and the changes that occur in electrode materials, the so-called 'operando' research. Although the range of research techniques has expanded enormously in recent decades, additional techniques and methods are desirable. By applying methods simultaneously, new insights are created that are based on complementary information. This thesis therefore provides an impetus to expand techniques with new possibilities and to further develop new and existing techniques.

## How do rechargeable metal ion batteries work

Today, the lithium ion (Li-ion) battery is the most widely used rechargeable energy storage system and is used in small electronics, portable devices, computing and telecommunications, among others. Especially in recent years, there has been tremendous growth due to use in the automotive industry for electrifying mobility and transport. Despite the dominant presence of Li-ion batteries in the battery landscape, more and more attention is being paid to batteries based on other ions, and even the first non-lithium ion batteries are slowly entering the market (Northvolt, 2024, Altris 2024, Natron 2024). Because only a specific ionic charge carrier in the electrolyte shuttles back and forth ('rocks') between the electrodes during charging and discharging without causing a significant change In the transporting electrolyte composition, this type of battery is called a 'Rocking Chair Battery' (Megahed & Scrosati, 1994). Various ions can be used as energy carriers. In addition to a small number of non-metallic ions ($NH_4^+$, $F^-$, $Cl^-$), most are metallic in nature, with a focus on the lighter metals (e.g. $Li^+$, $Na^+$, $K^+$, $Mg^{2+}$, $Zn^{2+}$, $Ca^{2+}$, and $Al^{3+}$). Collectively, this latter type of battery is called a metal ion battery, the principle of which is shown schematically in Figure 1.2. Here the various components a battery is composed of are indicated, such as the negative electrode (typically but erroneously referred to as the anode), the positive electrode (typically but erroneously referred to as the cathode) - which both are the active materials for hosting ions, the current collectors, for transporting electrons back and forth, and the separator housing the electrolyte, separating the electrodes allowing ions to pass and at the same time preventing internal shorts by blocking electron transfer. All these components are processed into separate films and stacked on top of each other in a compact manner to form an electrochemical cell. The most commonly used embodiments are the cylindrical cell, in which the foil package is wound and placed in a cylindrical can, the prismatic

cell, in which the foil package is folded into a flat geometry and placed in a box-shaped embodiment, and the pouch cell in which foil packages are placed. stacked alternately on top of each other and placed in an airtight bag or 'pouch'. However, the final embodiment of a battery is chosen on practical reasons largely determined by the application, the underlying chemistry, materials, morphology, and electrode geometry, which finaly determine how the battery will perform.

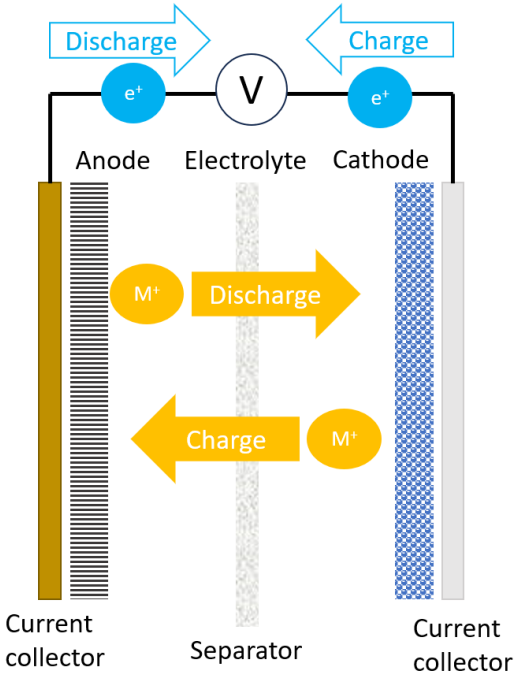


Figure 1.2: Principle of metal Ion batteries

## Processes and parameters that influence performance of a battery

Beside environmental circumstances and operation conditions, the performance of batteries is influenced by various factors, such as technical design (Yamada et al. 2020), material choice and properties (Mei et al 2019), electrochemical processes (Xu et al. 2007), morphology of electrode materials (Wei et al. 2021; Zao et al. 2018) , interface properties (Wang et al. 2024; Pan et al. 2017; Aurbach, 2000) and many others, all on macro, micro and nano scales. Characteristics such as power density, energy density, maximum C-rate and cycle life are used to quantify battery

performance, but doesn't provide information about the underlying causes of performance loss, aging and limitations that occur during battery use. To understand this in detail, complementary and advanced measuring techniques need to be applied at different situations and time scales for analysing the various processes, including reversible as well as irreversible (ageing) processes. Some measurements are performed on one or more components of a battery in an isolated setting to study specific processes, while other measurements focus on the processes caused by the interplay between the components in the entire assembled battery. The scala of measurements that scientists work with, extends from measurements on a single crystal or a well-defined sample surface (Tepavsevic et al. 2020; Takeuchi et al. 2015), to measurements on processes in a fully assembled battery during operation, the so called 'operando measurements' (Grant & Dwyer, 2022; Harks et al. 2015). The combination of these different techniques is necessary to be able to analyze, explain and model the complex processes, and to provide the necessary insights into the functioning of a battery under different circumstances.

The electrode materials of a battery are assembled in the form of foils, often as a coated current collector by the so called casting method (Hawley & Li, 2019), but there is increasing interest in advanced deposition techniques (Mills et al. 2014), stand-alone foils (Chen et al. 2021), or pure metallic electrodes (Wei et al. 2022). In all situations the thickness and the surface area of an electrode material are important performance parameters on the macro scale. The surface influences the exchange of ions at the interface between electrode and electrolyte, while the thickness partly influences the path that an ion and an electron have to travel, i.e. the accessibility of the host material for ions and electrons.

If we zoom-in into the electrode material to sub-millimeter dimensions other features play an important role in the performance of a battery. Dependent on the way the electrode material is prepared, parameters like porosity, particle size, morphological forms, structures and electrical contact are decisive for performance, and several measurement techniques are used for research on these parameters (Barai et al. 2019). When we zoom in more we reach the world of sub-micron and nanoscale, where again battery performance is Influenced by several parameters. Again, on this level, specialized techniques are used for research and analysis (Harks et al. 2015).

## Development of characterization techniques

The research described in this thesis investigates whether two measurement methods, namely Scanning Probe Microscopy (SPM) and Positron Annihilation Spectroscopy (PAS), can be used or expanded in order to further contribute to battery research.

### Scanning Probe Microscopy

Scanning Probe Microscopy (SPM) is a general name for measurements based on the principle of generating an image of a scanned surface while one or more parameters are measured, where a certain parameter is used to determine and control the probe distance from the sample surface. The first SPM based system was the Scanning Tunneling Microscope (STM) introduced by Binning and Rohrer in 1979 (Binnig et al, 1982). It uses a sharp needle-like tip which is scanned in close contact over the surface, while the lift height of the tip is controlled by the tunneling current between tip and sample. Because the tunneling current is used in a closed-loop control system for height determination the STM technique is limited to conductive samples in vacuum. In 1986 Binnig and his co-workers (Binnig et al, 1986) developed a more advanced system based on the combined principles of the STM and the stylus profilometer, the Atomic Force Microscope (AFM) which uses a cantilever with a very sharp tip at the end to scan and map a sample surface with a lateral resolution of 30Å and a vertical resolution of less than 1Å. The bending of the cantilever is measured by laser reflection on the end of the cantilever and used to moderate and control the distance between sample and probe. The AFM allows measurements under atmospheric circumstances and produces images of conductors and insulators, and can operate in three different work modes. The tip is constantly in contact with the sample during scanning in *contact mode*, or brought into resonance and oscillate over the sample while touching the sample shortly in *tapping mode*. But the AFM owes its name to the most advanced mode where the probe tip is brought in resonance with a very close distance to the sample while the bending is caused by the Lorentz force between tip and sample, the so called *non-contact mode*. The latter makes it possible to create an image of the atomic lattice of a sample. Generally, AFM makes it possible to produce high quality and high resolution surface images because of the accurate control over the movement of the probe and sample distance. After the Introduction of AFM, several variations on this technique were developed, Including Kelvin Probe Force Microscopy (KPFM, main parameter surface potential), Scanning Resistance Microscopy (SRM, conductivity), and much more variants on the principle of a scanning probe.

### Designed AFM set-up and environment for high accuracy measurements

Battery materials are highly reactive and can rapidly degrade when exposed to oxygen and moisture. To prevent contamination and degradation, it is essential to work in a protected glovebox environment. This imposes a critical requirement for operando AFM (Atomic Force Microscopy) on battery materials, necessitating that the AFM system be placed within a glovebox. Additionally, the AFM's high precision requires it to operate in a vibration-free environment, making standard commercially available glovebox systems unsuitable for achieving the desired measurement resolution, which ranges from 10 to 200 nm.

A specially designed glovebox has been developed to meet the requirements for AFM measurements and allows probing inside exposed battery cells. Figure 1.3 illustrates the facility designed for operando AFM on batteries. The cube-shaped glovebox is gas-sealed and mounted on a heavy stone base, ensuring the vibration-sensitive AFM rests on a stable platform. To minimize vibrations from the purifier's pump and blower, the inert argon atmosphere is circulated through the glovebox using bellows couplings. An active vibration isolation system (Accurion Halcyonics_i4) absorbs vibrations in the range of 0.2 to 200 Hz, further ensuring measurement accuracy. Since even the gas flow through the box can introduce vibrations, a bypass system is integrated between the gas inlet and outlet to control the flow near the AFM and avoid any disturbances during measurements. Additionally, any noise that might interfere with the cantilever's movement, such as talking or door movements, must be minimized.

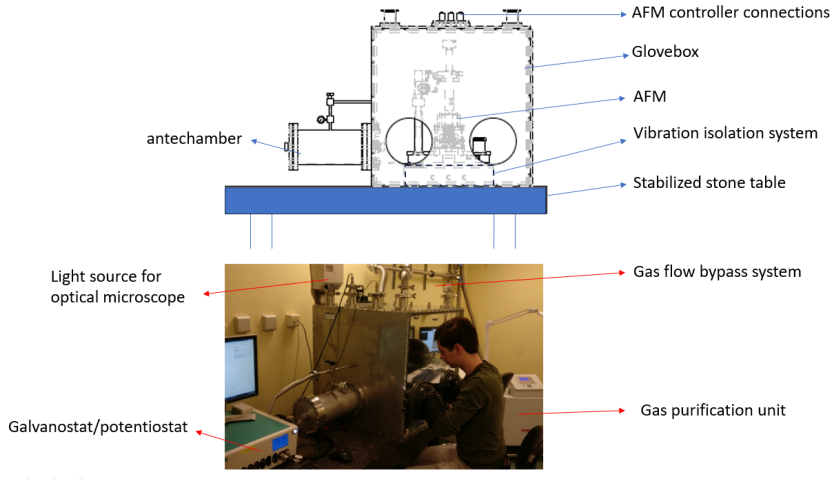


Figure 1.3: The AFM facility with vibration reduction glovebox environment and connected galvanostat/potentiostat (written informed consent was optained from the individual portrayed in this image).

The chosen AFM system for this project is the NT-NDT NTegra P9, which features an open design allowing easy access to the sample area. The AFM setup comprises two components: the controller, which is located outside the glovebox, and the measurement device, housed inside. Special connector feed-throughs are used to bring all necessary connections for the AFM into the glovebox. A fiber optic cable supplies light for the optical microscope inside, while a vacuum-sealed USB port allows signals from a digital camera to be transmitted to the computer, enabling live video of the scanning cantilever during measurements.

The optical microscope (Opta 2.0x mini) can be rotated to provide clear access to the probe and sample holder. The AFM itself features a three-legged scanning head that can be easily attached or removed, minimizing the inconvenience of working with gloves while maintaining measurement precision. The AFM is equipped with an internal bias voltage source and a highly sensitive current meter (iprobe). The internal circuit can be configured through the NTegra software interface (NOVA px), allowing both the tip and the sample to connect to either the internal voltage source, internal ground, or an external connector. To extend the measurement capabilities and enable advanced battery analysis, connections for a Galvanostat/ Potentiostat (Metrohm Autolab PG-STAT302F) have been routed into the glovebox via coaxial cables, facilitating impedance analysis, cyclic voltammetry, charge/ discharge procedures, and various other electrochemical tests.



### Positron Annihilation Spectroscopy

In 1928, the theoretical physicist in quantum mechanics Paul Adrien Maurice Dirac predicted the existence of anti-matter (Dirac, 1928) composed of anti-particles including the positron, which is the opposite particle of an electron. In 1932, Carl Anderson (Anderson, 1932) studied showers of cosmic particles in a cloud chamber and detected a track of a particle that must be positive charged with the same mass as an electron, later identified as the first anti-particle in physics, the positron. In 1936 Anderson shared the Nobel prize in physics with Victor Hess for discovering the positron. Shortly after the discovery, annihilation studies of electrons and positrons where carried out and lead to the insights that the analysis of momentum and energy distribution during annihilation can be utilized to investigate material properties of condensed matter. It turned out that the annihilation of positrons is very sensitive to defects, in particular lattice imperfections, vacancies, vacancy agglomerates, dislocations, i. e. trapping of positrons in open volumes (voids). A positron is trapped by the formation of an attractive potential caused by the lack

of a repulsive positively charged nucleus in such a defect. The sensitivity of defect detection is high (more than one vacancy per $10^7$ atoms), which makes positron annihilation spectroscopy a unique non-destructive measurement method that provides crucial information about defects in materials.

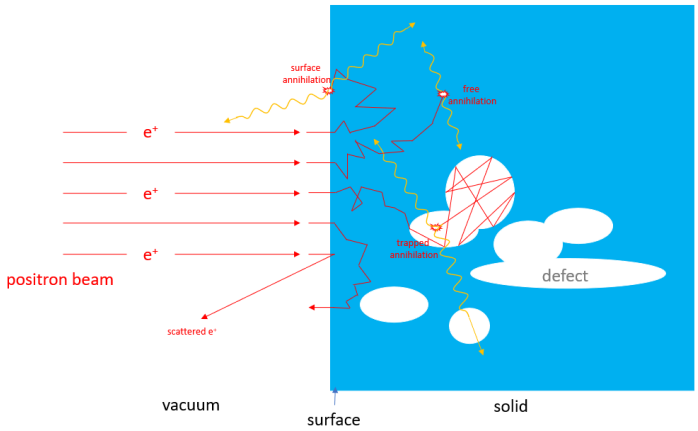


*Figure 1.4: different annihilations of a positron-electron pair*

A trapped positron will find an electron to annihilate and form two 511 keV photons which are emitted in nearly opposite (anti-parallel) directions. Trapping of positrons in defects is observed as well-defined changes in this positron–electron annihilation radiation. Three measurement methods are based on this process:

1. Positron Annihilation Lifetime Spectroscopy (PALS), based on correlating the lifetime (dwelling time) of the injected positrons against the sample void size (longer lifetimes correspond to large void sizes).
2. Angular Correlation of the positron annihilation Radiation (ACAR), where the small deviation of the angle between the two almost anti-parallel emitted photons is used to determine the momentum distribution of electrons.
3. Doppler Broadening Positron Annihilation Spectroscopy (DBPAS), where the Doppler shift of the 511 keV positron–electron annihilation radiation peak is used to determine the momentum distribution of electrons.

The latter technique is used for the study described in this thesis. The shape of the DBPAS momentum distribution spectrum is characterized with two parameters, the low-momentum *shape* parameter *S* which is a measure for the fraction of counts in the central region of the peak, and the *wing* parameter *W* which corresponds to the fraction of counts on both sides of the peak. Figure 4 shows a typical momentum distribution spectrum with the energy windows of *S* and *W*. Typically, an increase

in the value of *S* indicates an increase in open volume defects in the depth being probed, while the value of *W* is more dependent on the atoms surrounding the defect where the annihilation takes place.

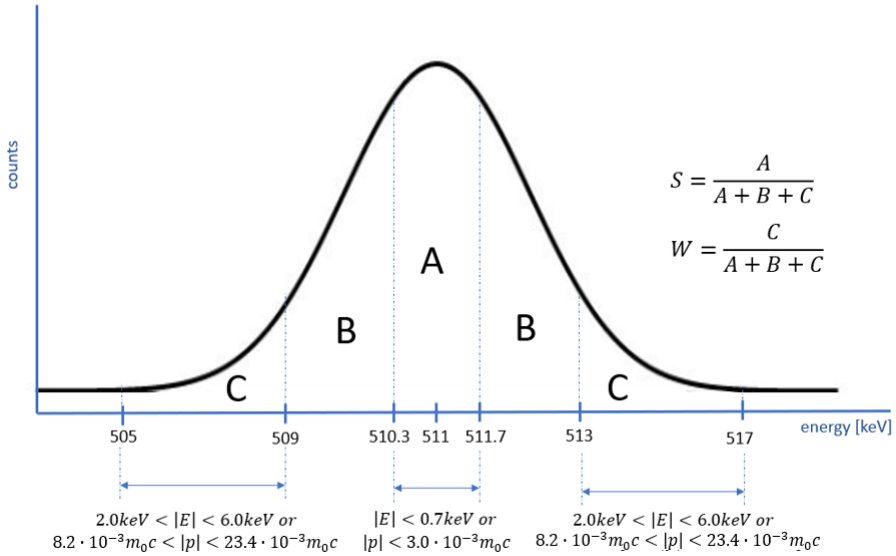


Figure 5: determination of the S and W shape parameters of the momentum distribution spectrum For analyses, both the *S* parameter and the *W* parameter are used independently of each other (Gramsch et al. 1999; Abdel-Rahman et al. 2006), while in many studies they are combined because they often complement each other and can therefore provide more insights (Clement et al. 1996).

## Scope of the Thesis

The overall aim of the work described in this thesis is to study the feasibility of new advanced measurement methods, providing researchers with more tools to investigate the complex and interacting processes in batteries. Two methods were investigated and extended with new insights and methods in this study, (i) the use of SPM for electrode-electrolyte interface analyses, and (ii) the use of Doppler Broadening Positron Annihilation Spectroscopy (DBPAS) for electrode bulk analysis. Hence, Chapter 2 investigates whether the probe of an AFM can be supplied with a small amount of lithium so that a non-faradic measurement can take place between probe and sample. With a lithium-provided probe, a very small submicron-sized half-cell is created, allowing ion current to be related to the surface condition and morphological situation of an electrode. In Chapter 5 the same is repeated for

magnesium in an aqueous electrolyte, whereby the deposition morphology of magnesium is compared with the way in which metallic lithium-growth takes place. Chapters 3 and 4 discuss the use of positrons as a probe for bulk processes in silicon anodes for lithium ion batteries. Both the initial processes (Chapter 3) and the processes that occur during multiple cycling (Chapter 4) are examined. These studies in this thesis are based on the following research questions:

1. How can a probe of an SPM be provided with an amount of metal so that it can be used to create a sub-micron half-cell for research into metal-ion batteries?
2. How can processes in battery electrodes be investigated using positron annihilation spectroscopy?

To answer these questions, solutions were sought for the various technical challenges of using these techniques for battery research and these techniques were subsequently used to investigate actual scientific questions (Silicon anode cracking for positron annihilation techniques and magnesium deposition using an aqueous electrolyte for advanced SPM techniques).

# References


Abdel-Rahman, M., Abo-Elsoud, M., Eissa, M. F., Kamel, N., Lotfy, Y. A., & Badawi, E. A. (2006). Positron annihilation line shape parameters for CR-39 irradiated by different alpha-particle doses. *Progress in Physics*, *3*(2006), 91.

Adediran, I. A., Isah, K. O., Ogbonna, A. E., & Badmus, S. K. (2023). A global analysis of the macroeconomic effects of climate change. *Asian Economics Letters*, *4*.

Altris (2024). https://www.altris.se/

Anderson, C. D. (1932). The apparent existence of easily deflectable positives. *Science*, *76*(1967), 238-239.

Aurbach, D. (2000). Review of selected electrode–solution interactions which determine the performance of Li and Li ion batteries. *Journal of Power Sources*, *89*(2), 206-218.

Barai, A., Uddin, K., Dubarry, M., Somerville, L., McGordon, A., Jennings, P., & Bloom, I. (2019). A comparison of methodologies for the non-invasive characterisation of commercial Li-ion cells. *Progress in Energy and Combustion Science*, *72*, 1-31.

Binnig, G., Rohrer, H., Gerber, C., & Weibel, E. (1982). Surface studies by scanning tunneling microscopy. *Physical review letters*, *49*(1), 57.

Binnig, G., Quate, C. F., & Gerber, C. (1986). Atomic force microscope. *Physical review letters*, *56*(9), 930.

Chamie, J. (2023). Climate Change with 8 Billion Humans. In *Population Levels, Trends, and Differentials: More Important Population Matters* (pp. 59-63). Cham: Springer Nature Switzerland.

Chen, H., Yang, Y., Boyle, D. T., Jeong, Y. K., Xu, R., de Vasconcelos, L. S., ... & Cui, Y. (2021). Free-standing ultrathin lithium metal–graphene oxide host foils with controllable thickness for lithium batteries. *Nature Energy*, *6*(8), 790-798.

Clement, M., De Nijs, J. M. M., Balk, P., Schut, H., & Van Veen, A. (1996). Analysis of positron beam data by the combined use of the shape-and wing-parameters. *Journal of applied physics*, *79*(12), 9029-9036.

Dirac, P. A. M. (1928). The quantum theory of the electron. *Proceedings of the Royal Society of London. Series A, Containing Papers of a Mathematical and Physical Character*, *117*(778), 610-624.

Gramsch, E., Lynn, K. G., Throwe, J., & Kanazawa, I. (1999). Positron diffusion in solid and liquid metals. *Physical Review B*, *59*(22), 14282.

Grant, A., & O'Dwyer, C. (2022). Operando Methods and Probes for Battery Electrodes and Materials. *arXiv preprint arXiv:2207.12098*.

Harks, P. P. R. M. L., Mulder, F. M., & Notten, P. H. L. (2015). In situ methods for Li-ion battery research: A review of recent developments. *Journal of power sources*, *288*, 92-105.

Hawley, W. B., & Li, J. (2019). Electrode manufacturing for lithium-ion batteries—Analysis of current and next generation processing. *Journal of Energy Storage*, *25*, 100862.

Megahed, S., & Scrosati, B. (1994). Lithium-ion rechargeable batteries. *Journal of Power Sources*, *51*(1-2), 79-104.

Mei, W., Chen, H., Sun, J., & Wang, Q. (2019). The effect of electrode design parameters on battery performance and optimization of electrode thickness based on the electrochemical–thermal coupling model. *Sustainable energy & fuels*, *3*(1), 148-165.

Mills, E., Cannarella, J., Zhang, Q., Bhadra, S., Arnold, C. B., & Chou, S. Y. (2014). Silicon nanopillar anodes for lithium-ion batteries using nanoimprint lithography with flexible molds. *Journal of Vacuum Science & Technology B*, *32*(6).

Natron (2024). https://natron.energy/

Northvolt (2024). https://northvolt.com/products/cells/sodium-ion/

Pan, Q., Barbash, D., Smith, D. M., Qi, H., Gleeson, S. E., & Li, C. Y. (2017). Correlating electrode–electrolyte interface and battery performance in hybrid solid polymer electrolyte-based lithium metal batteries. *Advanced Energy Materials*, *7*(22), 1701231.

Rohrer, H., Binnig, G. (1983). Scanning Tunnelling Microscopy. https://doi.org/10.5169/seals-115309.

Takeuchi, S., Tan, H., Bharathi, K. K., Stafford, G. R., Shin, J., Yasui, S., ... & Bendersky, L. A. (2015). Epitaxial LiCoO2 films as a model system for fundamental electrochemical studies of positive electrodes. *ACS applied materials & interfaces*, *7*(15), 7901-7911.

Tepavcevic, S., Zheng, H., Hinks, D. G., Key, B., Ward, L., Lu, Z., ... & Markovic, N. M. (2020). Fundamental insights from a single-crystal sodium iridate battery. *Advanced Energy Materials*, *10*(10), 1903128.

Voigtlander. B., (2015). Scanning Probe Microscopy. Springer Berlin Heidelberg: New York

Wang, L., Yu, J., Li, S., Xi, F., Ma, W., Wei, K., ... & Luo, B. (2024). Recent advances in interface engineering of silicon anodes for enhanced lithium-ion battery performance. *Energy Storage Materials*, 103243.

Wei, C., Tan, L., Zhang, Y., Wang, Z., Feng, J., & Qian, Y. (2022). Towards better Mg metal anodes in rechargeable Mg batteries: Challenges, strategies, and perspectives. *Energy Storage Materials*, *52*, 299-319.

Wei, T. T., Wang, F. F., Li, X. Z., Zhang, J. H., Zhu, Y. R., & Yi, T. F. (2021). Towards high-performance battery systems by regulating morphology of TiO2 materials. *Sustainable Materials and Technologies*, *30*, e00355.

Xu, M. Q., Li, W. S., Zuo, X. X., Liu, J. S., & Xu, X. (2007). Performance improvement of lithium ion battery using PC as a solvent component and BS as an SEI forming additive. *Journal of Power Sources*, *174*(2), 705-710.

Yamada, M., Watanabe, T., Gunji, T., Wu, J., & Matsumoto, F. (2020). Review of the design of current collectors for improving the battery performance in lithium-ion and post-lithium-ion batteries. *Electrochem*, *1*(2), 124-159.

Zhao, Y., Ding, C., Hao, Y., Zhai, X., Wang, C., Li, Y., ... & Jin, H. (2018). Neat design for the structure of electrode to optimize the lithium-ion battery performance. *ACS applied materials & interfaces*, *10*(32), 27106-27115.

# CHAPTER TWO

*Scanning active-probe microscopy techniques on battery electrodes*

This chapter is based on: Legerstee, W. J., Boekel, M., Boonstra, S., & Kelder, E. M. (2021). Scanning Probe Microscopy facility for Operando study of redox processes on Lithium Ion Battery electrodes. *Frontiers in Chemistry*, *9*, 505876

# Scanning Active-Probe Microscopy techniques on battery electrodes

## Introduction

The automotive industry with its high demands forms an enormous driving force behind the large growth of the battery market. Due to practical requirements, there is a need for faster charging solutions and a large variety in charging strategies is offered to charge vehicles. Fast charging becomes more common and contact-less charging is around the horizon. Large variations in charging conditions lead to degradation of the battery and faster aging (Nagpure et al. 2013). At the same time, new battery materials with a higher gravimetric and volumetric energy density are being sought, and these requirements must also be combined with automotive requirements such as high stability and long battery life.

On the one hand, improvements to the current lithium ion (Li-ion) cells are being sought, but more and more research is being done into possibilities beyond Li-ion batteries, for example sodium-ion and magnesium-ion batteries. This increases the need for specialized research into rechargeable batteries and the need for new and powerful characterization methods.



Several research groups have developed scanning probe microscopy techniques to investigate electrochemical processes (Arreaga-Salas et al. 2012; Benning et al. 2019; Kim et al. 2018; Zhang et al. 2020), and a commercial AFM-SECM instrument has recently become available which is suitable for battery research (Bruker 2020). However, all these scanning probe techniques are used to *analyze* battery processes on micro to nano level, while charge and discharge conditions are *controlled* at bulk level. Therefore, in this study we investigated the possibility of using the probe as an active component during the measurement, and so, makes it possible to tune charge and discharge parameters on a local scale. A set-up has been developed for this purpose in which an AFM has access to an open battery cell under controlled conditions. Several techniques have been investigated to provide the probe with lithium so that it can operate as counter electrode and participate as part of the dynamic interphase processes in a controlled way.

Significant battery aging processes take place at the interfaces between the electrode and the electrolyte. A Solid Electrolyte Interphase (SEI) forms at this

interface, which is related to processes responsible for aging and loss of capacity. The capacity loss consists of a reversible and an irreversible part, both contributing to the impedance of the interphase (Lam et al. 2013). With bulk-level Electrochemical Impedance Spectroscopy (EIS) it is possible to Investigate these processes and distinguish between the contribution of reversible and irreversible processes, but the relationship between the irreversible processes and local electrode surface properties, such as morphology, local composition, grain size and shape, crystal orientations, etc. is poorly known. Hence, combining AFM and non-faradaic EIS provides a powerful method to investigate local processes at the nanoscale and get more insight into transport physics as a function of spatial coordinates.

## Scanning Probe Microscopy

Scanning probe microscopy (SPM) is a collective term for high resolution measurements in which the surface of an object is scanned with a very small probe to produce a three-dimensional image. After the development of the Scanning Tunneling Microscope (STM) (Binnig, Rohrer 1983) and the Atomic Force Microscope (AFM) (Binnig et al. 1986), many variations on this highly sensitive measuring technique have arisen, among which- Scanning Capacitance Microscopy (SCM), Conductive AFM (C-AFM) and Kelvin Probe Force Microscopy (KPFM). The basis of the many variants is AFM, where attractive and repulsive forces between a very sharp tip and the sample surface are used to study surface morphologies. In general, for all these AFM-based measurement methods, the distance between the probe and the sample is determined by measuring small changes that occur in a controlled process parameter between surface and probe. These changes are converted into corrective movements of the probe that ensure that the probe accurately follows the surface. This technique can be used to create a 3D surface scan of all conceivable and measurable parameters between sample and probe with resolutions up to the nanometer scale (Amanieu et al. 2015; Benning et al. 2019; Kim et al. 2018; Nagpure et al. 2011; Mahankali et al. 2019).

In principle, the AFM-probe can be used for complex electrochemical measurements, such as impedance measurements on a very local scale. O'Hayre et al. (2004) performed quantitative impedance measurements in which, by pressing the tip firmly on the sample, a local impedance scan in contact mode can be performed. They developed a model that describes the impedance of the probe surface and takes into account the resistance of the tip, the interfacial resistance (resistance to the faradaic

charge transfer), the double layer capacitance and the distribution of the resistance from the probe tip into the sample. When the force is brought above a certain (sample-dependent) threshold value and it is kept as constant as possible over all measuring points, it is possible to perform and map SPM impedance measurements to investigate frequency-dependent phenomena on the nanometer scale.

A well-known SPM technique where electrochemical processes between tip and sample are mapped is Scanning Electrochemical Microscopy (SECM)(Bard et al. 1989). A glass pipet-like probe that consists of a metal core, the Ultra-Micro-Electrode (UME), is immersed in a solution, scans the sample surface and measures the current that results from redox reactions that takes place. The current can be measured as a function of the probe X-Y position which creates a two dimensional image map (Wittstock et al. 2007). Alternating Current Scanning Electrochemical Microscopy (ac-SECM) is a form of SECM in which a sinusoidal bias voltage is applied to the UME to indirectly measure the impedance response of the sample under investigation for a single ac frequency (Eckhard et al. 2007; Diakowski et al. 2007). To obtain impedance information over a wider frequency range, a combination of SECM and EIS called "Scanning Electrochemical Impedance Microscopy" (SEIM) has proven to be a powerful technique for investigating local electrochemical changes (Bandarenka et al. 2013). However, with all these methods, amperometric measurements are made between the UME and the sample in the presence of redox mediators and /or redox probes. Recently, from the bio-electrochemistry field, Valiūnienė et al. (2019), avoided the use of redox mediators and probes and demonstrated a redox probe-free approach to SEIM on conductive and non-conductive surfaces. To reduce the duration of the measurements, the SEIM technique was hybridized with Fast-Fourier Transform based EIS (FFT-EIS) which makes it possible to simultaneously measure up to 50 single sine-signals. The resulting non-faradaic FFT-SEIM application is used in the field of bio-electrochemistry for in-situ and operando evaluation of electrochemical processes (Valiūnienė et al. 2020; Morkvenaite-Vilkonciene et al. 2017).

### SPM for battery research

Many research groups have focused on investigating battery properties using AFM. In the simplest method, the battery is dismantled in a protected glove box and samples are rinsed clean, after which they can be analyzed by AFM (Demirocak & Bhushan 2015; Kim et al. 2018; Nagpure et al. 2010; Sakai et al. 2019; Yang et al. 2017). A major drawback of this method is that the condition of the samples can

be affected, which may result in loss of important properties. This type of research is therefore limited to mechanical and morphological techniques, such as analyzing changes in surface morphology, elasticity and hardness through battery use, and measuring changes in the material structure.

More and more researchers are using *in-situ* measurement methods ( Benning et al. 2019; Demirocak & Bhushan 2014; Doi et al. 2008; Inaba et al. 2011; Huang et al. 2018; Mahankali et al. 2019; Wang et al. 2014; ) where information about interface processes can be investigated without influencing them. In general, to perform in situ measurements, the battery process is temporarily or completely stopped, after which measurements are taken. This method is useful, inter alia, for investigating the origin and development of the SEI on the electrodes. The most advanced and complex way of measuring is achieved by operating the battery during the measurement, the so-called *operando* measurements (Breitung et al. 2016; Wang et al. 2017; Zhang et al. 2020). By performing a measurement this way, the dynamic processes that occur can be followed real-time and related to all kinds of battery parameters and settings, bringing this type of measurements closest to the practical behavior of the battery. The facility and techniques discussed in this thesis have been developed to allow *operando* measurements on batteries, taking it one step further by also including the probe as part of the measurement.

### AFM probe tip as an active element

By creating battery operation between the probe tip and the sample in a controlled manner, a powerful analysis method is added to the range of possibilities that AFM offers. This technique opens the way to simultaneous monitoring of morphological, mechanical, electrical and electrochemical properties and processes. To achieve this, it is necessary to provide the tip with a small amount of lithium. In fact the tip will function as an active part of a battery.

During a preliminary investigation in our laboratory we looked at the possibility of bringing lithium into the probe by alloying a Silicon tip with Lithium (Garcia-Tamayo, 2014). The principle has been demonstrated but many practical problems were encountered. Measurements were performed without the use of a controlled glovebox environment. A liquid measuring cell has been used that was covered with a membrane and flushed with Argon gas, and which offers protection against contamination for a short time (ND-MDT liquid cell). An uninsulated AFM probe (ND-MDT NSG03, figure 2.1b) was used and measurements were made with the

entire chip immersed in electrolyte (1M $LiPF_6$ in EC/DMC 1:1), electro-chemically prepared as half-cell versus metallic lithium. Figure 2.1a shows a charge-discharge curve that was measured by the use of a Potentiostat/Galvanostat (Metrohm Autolab PG-STAT302F). As a result, lithiation took place over the entire chip, making the measurement not properly controlled and even lithiation resulted in distorted tips due to silicon expansion, see Figure 2.1c.

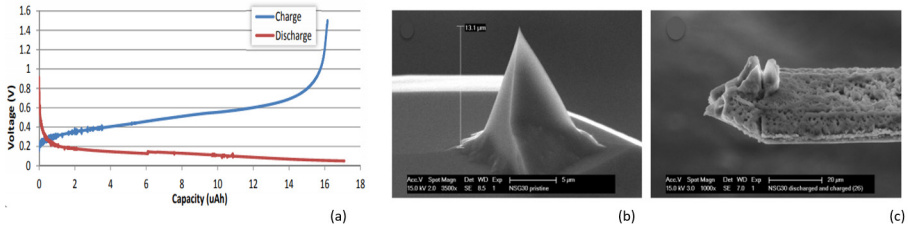


Figure 2.1: (a) Discharge (red) and charge (blue) curve of silicon probe vs. metallic lithium. (b) pristine tip. (c) Probe after discharge and charge procedure.



The conclusion of this exploratory study was that in principle it is possible to store lithium in the tip and these tips can also be stored over a longer period of time without degrading (Garcia-Tamayo, 2014). In fact, although the results were not conclusive, this preliminary study showed that it is possible to alloy lithium with the silicon of the AFM chip (including the cantilever and tip), and electrochemically take it out again. The aim of our research is therefore to make the process controllable and manageable and to investigate how a lithiated probe can contribute to operando measurements of battery materials.

## Experimental setup

For carrying out battery research with an AFM, setups have been realized by various research groups and even an advanced commercial device is available (Bruker, 2020). Here we describe a self-assembled and tailor-made setup that is affordable compared to the commercial offer and also allows a lot of flexibility and adaptability.

### Customized glovebox environment for SPM measurements on operational battery electrodes

Battery materials are very sensitive to contamination with water and oxygen and therefore an AFM measurement must be performed under protected conditions. Various methods are possible to achieve this. At first a gas-tight and flushable

sample holder can be integrated with the probe holder of the AFM equipment. A disadvantage may be that the sample room is very complex, but this keeps the AFM measuring equipment easily accessible and usable for other research that does not require a protected atmosphere. A simple alternative is to use so-called glove bags with which the AFM equipment can be enclosed and placed under Argon atmosphere. Because of the relatively poor level of protection against contamination, this mode of operation is inconvenient for long term measurements on batteries. The highest protection can be obtained by placing the AFM equipment in a glovebox. The disadvantage is that all necessary connections for control and measurement have to be entered into the glovebox and that the AFM is only accessible through the gloves of the glovebox. The advantage is the great flexibility in designing the sample holder and the use of the wide range of probes that are commercially available.

It is desirable to set up an AFM as vibration-free as possible. Preventing vibrations increases the accuracy with which measurements can be taken. In order to be able to perform measurements in the desired resolution of 10 to 200 nm, vibrations must be prevented as much as possible and any vibration damping measures must be taken.

A special glovebox has been designed which includes all requirements for AFM measurements and makes it possible to probe inside open exposed batteries. The designed facility for AFM on batteries consists of a cube-shaped glovebox which is mounted gastight on a heavy stone table, so that the vibration-sensitive AFM stands directly on a stable surface. The connections required for purifying and circulating the inert argon atmosphere through the glovebox are equipped with bellow couplings, preventing the transmission of vibrations from the pump and blower of the purifier unit. To eliminate almost all remaining vibrations, the AFM set-up is placed on an active vibration isolation system that absorbs vibrations in the range of 0.2 to 200 Hz (Accurion Halcyonics_i4). During sensitive measurements, even the gas flow through the box can cause vibrations, and therefore a bypass system is placed between the gas inlet and outlet. This allows the gas to flow partly through the box and partly through the bypass so that the flow along the AFM can be adjusted such that no disturbances of the measurements occur. During measurements, the gas flow can be reduced while the purity of the atmosphere stays at the desired level for at least 72 hours (<1 ppm moisture and oxygen). Test measurements with calibration samples have shown that a scanning resolution of at least 10 nm is achievable under these conditions.

## AFM Instrument coupled with a Galvanostat/Potentiostat

The AFM equipment selected for this project is the NT-NDT NTegra P9, a very open instrumental design where access to the sample space can be obtained without obstacles. The AFM equipment consists of two parts, the controller unit, which is located outside the glovebox, and the measuring device, which is located inside the glovebox. All necessary connections for the AFM measuring device have been brought into the glovebox via special connector feed-throughs. The required light for the optical microscope is coupled inwards via a fiber optic connection and a vacuum tight USB port is used for bringing the signals of a digital camera to the computer which allows live video of a scanning cantilever during the measurements.

The optical microscope (Opta 2.0x mini) can be turned away for creating access to the probe and sample holder. The AFM is equipped with a three-legged scanning head which can easily be placed and removed. The inconveniences caused by working with rubber gloves are thus minimized while keeping very accurate measurements possible. This AFM equipment is provided with an internal bias voltage-source and a highly accurate current meter, the so-called *iprobe*. The internal circuit can be adjusted via the user interface of the NTegra software (NOVA px), whereby both the tip and the sample can be connected to the internal voltage source, the internal ground, but also to an external connector. To generate more measurement options and enable advanced battery analysis, the connections of a galvanostat / potentiostat (Metrohm Autolab PG-STAT302F) have been brought into the glovebox via coaxial cables, enabling impedance analysis, cyclic voltammetry, charge and discharge procedures and many other electrochemical measurements.



## AFM accessible cell

In order to be able to perform AFM measurements on the electrode materials within a working battery, a special open-cell sample holder has been developed. Figure 2.2 shows a cross section and a "battery prepared" photo of the *"Atomic Force Microscope Accessible Battery cell"* (AFMAB). As can be seen in the expanded image, the AFMAB consists of a liquid-tight housing on which all parts of a battery can be stacked. First, a sample substrate (1) is placed in the holder. Electrical contact is obtained with the gold-plated spring pins (2). Separator material is placed on top of the substrate with a small hole (4) in the middle at the position of the sample. Use of a reference electrode is possible by placing it between two stacked separators and leading the electrical contact out with an Kapton® insulated wire. The working part (5) is then screwed onto the housing so that the golden pins (2) make electrical contact

with the substrate. On top of the stacked separator a thin lithium anode (6) is placed, again with a small hole (4) at the position of the sample. Finally, the counterpart (7) with golden spring pins to the lithium anode is placed on top and connected with screws to tighten the stack of materials. Once the cell has been assembled, the AFMAB can be placed at the measuring position of the AFM and connected to the galvanostat/potentiostat equipment. By applying a desired amount of electrolyte in the liquid-tray (3), a cell is created in which the sample can be used as the working electrode of a battery and can be reached with the AFM. Bulk charge and discharge procedures can be performed until a desired state of the battery is reached, after which *in-situ* measurements can be performed when the processes are paused, or *operando* measurements can be carried out during operation. The cantilever chip is mounted on the crystal nosepiece (8), which is suitable for measurements in liquids, and can be fitted with a rubber membrane that can be used to close the AFMAB cell during measurement to minimize evaporation of the electrolyte.

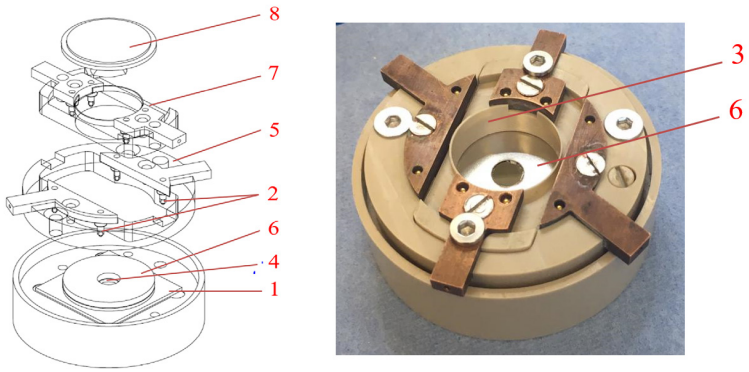


Figure 2.2: The Atomic Force Microscope accessable battery cell (AFMAB). (1)Sample substrate; (2)spring pin connections; (3)Liquid tray; (4)Separator; (5)Working electrode connector; (6)Lithium disc with hole (larger here then in case of real measurements); (7)Counter electrode connector; (8) Nose piece (probe holder)

## Monitoring the tip-lithiation process by shift of resonance frequency of the probe cantilever

In order to make the lithiation process of the tip controllable, a way of monitoring this process was sought. It has been investigated whether resonance frequency shifting of the cantilever in oscillation mode can be used to determine the amount of lithium added to the tip. A model has been set up that describes the relationship

between mass change and the shift of the first mode natural resonance frequency, and the cantilever oscillation as a function of added mass has been simulated.

## Theoretical mechanics of an oscillating cantilever

Due to the classical mechanics of oscillators a beam clamped on one side behaves like a mass spring system (Poggi et al. 2005). The complicated beam dynamics of a cantilever spring with small deflections is described by the Euler-Bernoulli equation (Bauchau et al. 2009; Payam & Fathipour 2009) and its solutions are given in vibrational modes with their 'eigenfrequencies'. The beam-dynamics for an individual resonance mode can be simplified with the dynamics of a common harmonic oscillator (Boisen el al. 2011), which is given by:

$$f_0 = \frac{1}{2\pi}\sqrt{\frac{k_{eff}}{m_{eff}}} \qquad \text{(Eq 2.1)}$$

For a homogeneously distributed cantilever with no anisotropy of the cantilever material in the beam direction, the effective spring constant $k_{eff}$ for the first and most important vibrational mode is given by:

$$k_{eff} = \frac{E \cdot h^3 \cdot w}{4L^3} \qquad \text{(Eq 2.2)}$$

where $E$ is Young's modulus and $h$,$w$, and $L$ are height, width and length of the cantilever, respectively. The effective mass $m_{eff}$ for the first mode of a homogeneously distributed cantilever is given by:

$$m_{eff} = 0.2427 m_{cantilever} \qquad \text{(Eq 2.3)}$$

For a freely oscillating cantilever the resonance frequency $f_0$ changes when a small amount of lithium with mass $m_{Li}$ is added to the very end of the beam. When we assume that $m_{eff} >> m_{Li}$ and the mass is added at the end of the cantilever, the shifted resonance frequency for the first vibrational mode becomes:

$$f_{Li} = \frac{1}{2\pi}\sqrt{\frac{k_{eff}}{m_{eff}+m_{Li}}} \qquad \text{(Eq 2.4)}$$

When we introduce the relative resonance shift $f_n$ as:

$$f_n = \frac{f_{Li}}{f_0} \qquad \text{(Eq 2.5)}$$

It follows from equation 2.1 and 2.4 that the added amount of lithium depends on $f_n$ and $m_{eff}$ as:

$$m_{Li} = \frac{f_n^2}{1-f_n^2} m_{eff} \quad \text{(Eq 2.6)}$$

With this equation a general relationship has been formulated between the relative resonance shift and the amount of added mass to the cantilever tip.

AFM probes are commercially available in many different shapes and sizes, made from different materials and often provided with a special coating, for instance a reflective or conductive layer. When a thin film of a different material is added to the surface of a cantilever, this will affect the mechanical bending properties and so the vibrational properties of the beam. Depending on the thickness of the layer and the orientation of the anisotropic substrate (Silicon cantilever), additional mechanical stress will occur, which in principle can be determined with an extended version of Stoney's equation (Injeti, S. S. & Annabattula, R. K. 2016). Both this stress and the addition of a layer with its own Young's modulus will influence the bending properties and thus the spring constant of the cantilever.

### Responsivity and sensitivity

In principle we want to use the AFM probe as a very sensitive mass detection instrument, i.e. a beam-based mass sensor, a technique which is often used for detection and mass determination of molecules in the field of bio-science (Boisen et al. 2011). In our case, a small amount of lithium is added to the very end of the beam during the lithiation process, which changes the effective mass $m_{eff}$ of the cantilever, resulting in a shift of the first mode resonance frequency. The minimum detectable mass, the *responsivity* $R_c$ is determined by the ratio between the change of mass of the cantilever and the change of the free resonance frequency (Zhang & Hoshino 2018):

$$R_c = \frac{\Delta f_0}{\Delta m_{eff}} \quad \text{(Eq 2.7)}$$

When we assume that the change of mass is very small in relation to the mass of the cantilever, the responsivity can be written as derivative of equation 2.1 with respect to the mass of the beam:

$$R_c \approx \frac{\partial f}{\partial m_{eff}} = -\frac{f_0}{2m_{eff}} \quad \text{(Eq 2.8)}$$

Equation 2.8 clearly indicates that the responsivity can be improved by increasing the resonance frequency or reducing the mass of the cantilever, both attainable by lowering the beam dimensions or reducing the material density. The dimensions of an AFM probe are in the order of micrometers and the probe is often made of Silicon, the sensitivity of this mass sensor is therefore roughly calculated between *10-30 kHz/ng*.

The responsivity can be regarded as a property of the used cantilever in a particular situation which makes it an important value in determining the capability of a probe for use as a mass detection sensor. The same ratio as described by equation 2.7 can be determined when including the instrument properties, such as noise, external vibrations and other influences. This will give us the *sensitivity* $S_{inst}$:

$$S_{inst} = \frac{\Delta f_{min}}{\Delta m_{min}} \qquad \text{(Eq 2.9)}$$

which is defined as the minimum input level required to produce an output that overcomes the threshold.



## Influence of damping

When describing the behavior of a cantilever as a harmonic oscillator, the effect of energy loss has not been taken into account so far. Damping, or the dissipation of kinetic energy from a vibrating cantilever is caused by both intrinsic processes (determined by material properties) and extrinsic processes (determined by the environment). The latter especially requires attention when operating the AFM under ambient conditions because the dominant source of dissipation of kinetic energy is the surrounding medium. For our application, in general, if the damping of the system increases, the resonance frequency decreases, causing the *responsivity* $R_c$ to decrease. In addition, the resonance peak is broadened (Q-factor decreases), which increases the noise level and so decreases the *sensitivity* $S_{ins}$. This makes it challenging to determine the added lithium mass on a cantilever in fluid environments using frequency shift (Payam & Fathipour, 2014; Korayem et al. 2012; Bhiladvala & Wang, 2004; Sader, 1998).

### Modelling frequency shift as a function of added lithium on the tip

Due to the complexity that arises when all parameters and properties of an oscillating cantilever are included, the dynamic behavior of a cantilever with added lithium has been simulated with Finite Element Method analysis (FEM) using the *Comsol multiphysics*® software package.

As a result of the production process, even the same type of cantilevers show variations in dimensions and shape (Poggi et al. 2005). These variations have an effect on the harmonic vibration properties of the beam, so in fact, no cantilever has the same resonance frequency. Therefore, in order to simulate the harmonic oscillation of a given cantilever, the exact measures must be known. Dimensions, shape and position of the tip are required to calculate the resonance frequency of a particular cantilever. For the FEM analysis given here we used a diamond coated conductive probe (Nanosensors GmbH CDT-NCHR, Nominal resonance frequency 400 kHz, Nominal force constant 80 N/m). The exact dimensions have been determined by measuring the sizes of the tip and cantilever with the use of a scanning electron microscope (SEM: JEOL JSM-IT100). The values stated by the manufacturer have been used for all mechanical material properties needed for the simulation (Silicon, density 2329 $kgm^{-3}$, E = 170☞$10^9$ Pa, Poison ratio = 0.28; Diamond, density 3514.9 $kgm^{-3}$, E = 1.1448☞$10^{12}$ Pa, Poison ratio = 0.068992). The thin layer of diamond that covers the probe has a thickness of 100 nm and the cantilever is provided with an aluminum reflection layer (thickness 30 nm) on top.

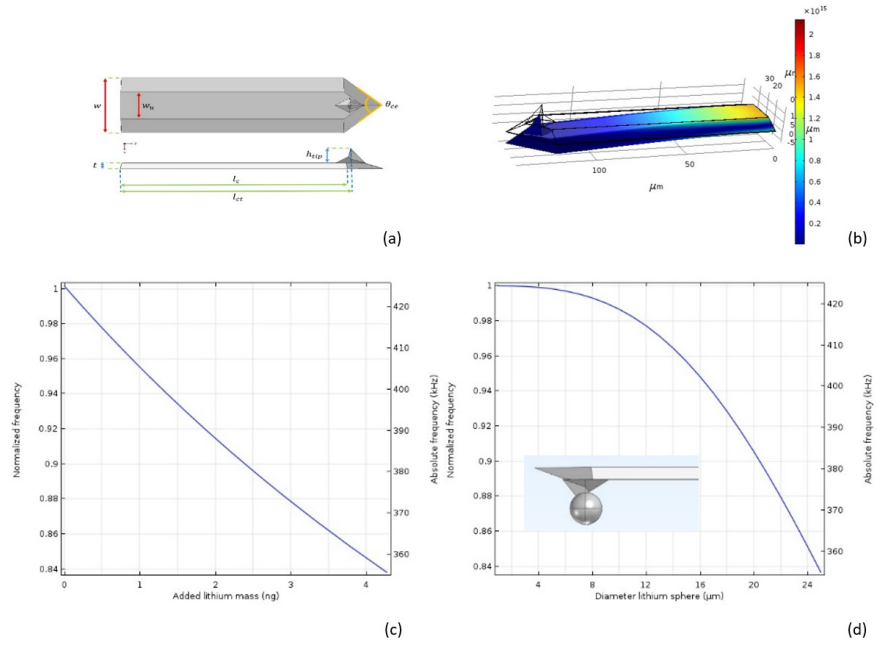


Figure 2.3: (a) Dimensions and (b) FEM analyses of the CDT-NCHR Diamond coated probe. (c) Simulation results of frequency shift as a function of added mass and (d) frequency shift as a function of diameter of a lithium sphere situated at the end of the tip

Figure 2.3a shows a 3D presentation of the model used for the FEM analysis. The plane at position 0 is actually the plane where the cantilever is attached to the chip and is therefore defined as a fixed plane. A vibrational analysis can be performed on the model whereby the first harmonic resonance frequency is calculated. Figure 2.3c and 2.3d shows the result of the vibration analysis on the cantilever model. The shift of the normalized frequency as a function of added lithium mass on the end of the tip as well as the frequency shift as a function of the diameter of a (theoretical) lithium sphere are presented. By using equation 2.7, the *responsivity* of the CDT-NCHR can be determined as $R_c$ = *-17.5 kHz/ng*.

## Probe tip lithiation methods

The methods that have been explored to supply the tip of the AFM probe with lithium can be divided into methods using liquid electrolyte (further mentioned as wet methods) and methods where no electrolyte is used (dry methods). Table 2.1 provides an overview of all lithiation methods that have been studied. The main methods are further explained below.



### Wet lithiation

In the wet lithiation experiments it was investigated how the tip of the probe can be supplied with lithium by bringing it into contact with electrolyte. Two principes have been explored to provide the tip with lithium, namely the plating method, based on the electrochemical deposition of a layer of lithium on the surface of the tip, and the alloy method, in which the lithium is alloyed with the silicon of the tip.

*Lithiation of the tip by immersing the entire probe*

The possibility of lithiating the tip by immersing the entire chip in the electrolyte has been investigated, requiring only the tip to be covered. Therefore, as shown in Figure 2.4a, a conductive and completely insulated probe is used, with only the end of the tip exposed. The choice between insulated probes is very limited, but a probe has been found with a platinum coated tip (NaugaNeedles™ NN-EENP-FM60 Nominal resonance frequency 60 kHz, Nominal force constant 3 N/m), which allows the plating method. The insulation on the cantilever and the carrier-chip makes it possible to completely or partially submerge the chip in electrolyte (LiPF6 EC/DMC 1:1, Sigma Aldrich). An electro-chemical half-cell was created between the AFM probe (working electrode) and a disc of Lithium (counter electrode). By applying a potential an ion current starts to flow through, hence, forcing lithium ions to move to the open tip end and as a result, depositing the exposed end of the tip with lithium.

Basically this method works and lithium is deposited on the tip, but a number of adverse effects occur, making this method practically not usable. Almost immediately after immersing the chip in electrolyte reactions takes place between the electrolyte and the material of the nosepiece and other parts of the equipment. The probe chip, including the reflective gold plating on the cantilever, is also affected, causing the laser reflection signal to become increasingly weaker and completely disappear over time, ultimately rendering probe control impossible. In addition, there is another important reason to preferably measure with a non-submerged cantilever. The large vibration damping effect of liquid on the cantilever will shift the resonance frequency of the cantilever to very low values, which has the consequence that the responsivity to mass change is much lower (see 4.3). Determining the added mass of lithium at the tip by measuring the resonance shift is therefore not possible with the desired accuracy.

Table 2.1: Classified probe tip lithiation methods

| Method | | Way of Lithium transfer | Used probe | Li mass determination by $f_r$ shift | efficacy |
|---|---|---|---|---|---|
| Wet | Electro chemical plating | Immerse chip in electrolyte | Isolated with exposed end NN-EENP-FM60 | Poor responsivitiy | Reactions with electrolyte disrupt AFM operation |
| | | Immerse tip in electrolyte film | diamond coated CDT-NCHR | Extra cleaning step needed | possibility that cantilever is covered with electrolyte during lithiation |
| | | Immerse tip in electrolyte soaked graphite electrode | diamond coated CDT-NCHR | Extra cleaning step needed | Lithium forms dendrite structure |
| | Alloying ($Li_xSi$) | Immerse tip in electrolyde film | Doped Si NSG30 | Extra cleaning step needed | Successful lithiation |
| | | Immerse tip in electrolyte soaked graphite electrode | Doped Si NSG30 | Extra cleaning step needed | Successful lithiation |
| Dry | Mechanical | Adhesion | Platinum coated PtSiNCH | Good responsivitiy | Successful lithiation |
| | Electro chemical plating | Contact | diamond coated CDT-NCHR | Good responsivitiy | Successful lithiation |
| | Alloying ($Li_xSi$) | Contact | Doped Si NSG30 | Good responsivitiy | Successful lithiation |
| | | Contact | Doped Si NSG30 | Poor responsivitiy | Successful lithiation |

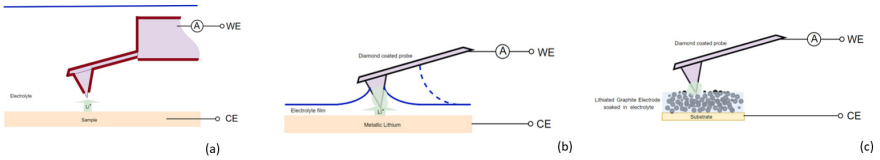


Figure 2.4: Wet probe lithiation methods. (a) Immersing method; (b) thin film method; (c) soaked electrode method (reference electrode was connected to CE in all situations).

The method in which the entire tip is immersed, thus appears to be very difficult to implement. In general, we can conclude that the immersion method influences the AFM's most important measurement principles over time and is not suitable for our purpose. Because of these drawbacks, methods have been investigated in which the cantilever can be kept out of the liquid. If the liquid only covers the tip and does not pass over the cantilever, this offers additional possibilities. This means for our purpose that non-insulated conductive probes can be used, which are widely available commercially and can be selected from a wide variety of material compositions and properties.



*Lithiation by immersing the tip in electrolyte film*

Figure 2.4b schematically illustrates a method of lithiating only the tip of the probe by pressing it in a thin deposited electrolyte film in a controlled manner. This method is performed with two types of electrolyte, namely the widely used LiPF6 EC/DMC 1:1 (Sigma Aldrich), and moreover a salt in a liquid state at room temperature, so-called *'Ionic Liquid' (IL)*($C_8H_{11}F_6N_3O_4S_2$*/* $LiC_2F_6NO_4S_2$ *100:1, Solvionic)*. The use of a diamond coated conductive probe (Nanosensors GmbH CDT-NCHR) allows the electrochemical plating method, while the use of a conductive silicon probe (NT-MDT NSG30) is suitable to form a silicon-lithium alloy tip. A disc of metallic lithium (99,99 pure, Sigma Aldrich) was used as a substrate and counter electrode for the lithiation process.

When the probe is brought very slowly to the liquid surface, a sudden bending of the cantilever is an indication that the tip has made contact with the electrolyte. Electrochemical plating of lithium can be started by applying a potential of a few tenths of volts, which will cause an ion current to flow. In the case of EC/DMC based electrolyte, the main problem is the surface tension driven fluid flow along the cantilever, as indicated by the dotted line in Figure 2.4b. Because the forces occurring by this capillary process are very small in relation to the total surface tension of the electrolyte, it cannot be detected whether this takes place. Figures 2.5a and 2.5b show two photographs where lithium covers all or partially the cantilever due

to electrolyte fluid climbing. It appears that for EC/DMC based electrolyte covering only the tip by immersing in an electrolyte film is difficult to control.



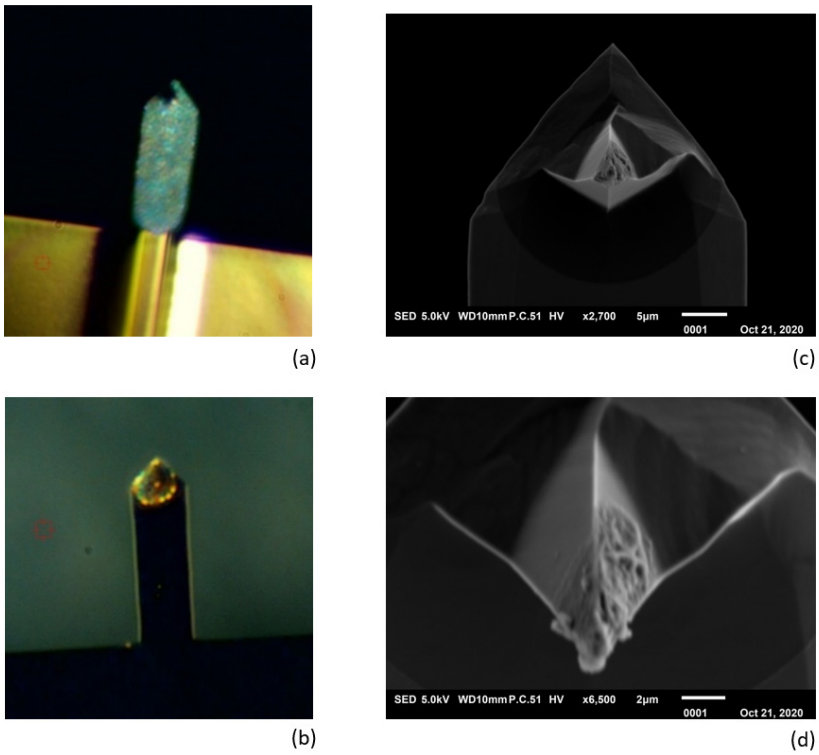


Figure 2.5: a and b: Lithiation covering the cantilever (EC/DMC based electrolyte). c and d: Lithiation of the tip by alloying (Ionic Liquid electrolyte)

By placing a drop of Ionic Liquid in the center of the lithium disk, a thin film can be created by fast rotation of the substrate. The ionic liquid has a high viscosity and is therefore a fairly viscous layer on the surface of the substrate. By setting a small probe pressure, it is possible to land the probe on the surface without breaking through the liquid. A small potential difference was applied between tip and sample to start lithiation of the NSG30 probe by the alloying method. The results are shown in Figure 2.5c and 2.5d.

*Electrolyte soaked graphite foil*

Pores in electrode material act as capillary channels filled with electrolyte which prevents the solvent from evaporation and form an electrolyte buffer. Figure 2.4c

schematically shows how a porous graphite electrode containing lithium and soaked with electrolyte can be used to lithiate the probe tip. Because lithiation is desired to take place at the probe tip-end, a very small amount of electrolyte is required to create battery operation between the tip and the sample, and due to the capillary forces of the porous graphite channels, this amount remains intact for a very long time.

To provide the graphite electrode with lithium, a dismountable lab-cell was used to form a half-cell by a lithium metal disk (2.011 $cm^2$) as the counter electrode, stacked with a separator (Celgard 2400), filled with 1M $LiPF_6$ in 1:1 EC/DMC as an electrolyte, followed by a working electrode of commercial battery-graded graphite powder casted on copper sheet (NEI Corporartion, Nanomyte BE200E). The graphite electrode was discharged with 0.1c (Maccor 4000) until a potential of 0.1 V against Li / Li+ was measured. The graphite foil has been carefully removed from the cell after which it has been applied to the AFMAB cell (Figure 2), provided with electrolyte and connected as a working electrode for lithiation of the probe-tip, as can be seen in Figure 2.4c.



As described above, the use of porous material as a substrate provides advantages. Climbing the electrolyte against the cantilever is counteracted by the capillary forces of the micro channels in the porous material, whereby, after setting the working distance to the sample, only the tip is covered with lithium.

Figure 2.6b and 2.6c show a SEM image of a tip that has been treated in this way, where the lithium is deposited only at the very end of the tip. The detailed SEM picture shows that the lithium has formed a sphere of dendrites on the tip. Figure 2.6a shows the absolute resonance frequency from before and after this treatment, wherein it is clearly visible that the addition of lithium results in a shift of 5,7±0,1 kHz of the resonance frequency. The amount of lithium applied to the tip can be deduced from this shift and is determined as 0.275±0,005 ng.

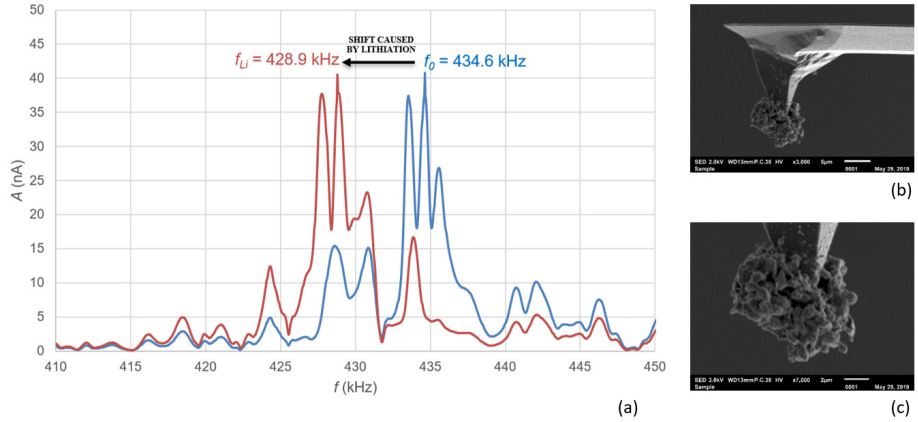


Figure 2.6: (a) Absolute shift of resonance frequency as a result of lithiation of the tip by electro- chemical plating; (b) and (c) a sphere of lithium dendrites at the end of the tip applied by electrochemical plating.

After applying lithium using the electrochemical plating method, an attempt was also made to electrochemically remove the lithium from the tip back to the substrate. This can be done simply by reversing the potential. This process has been carried out several times without success which may have to do with the formed lithium dendrites. These dendrites have probably formed a layer of dead lithium on the tip (Chen et al. 2017; Xiao 2019), as a result of which the charge exchange between tip and added lithium is blocked.

## Dry lithiation

In the dry methods, lithium is transferred to the probe tip without transporting lithium using electrolyte. here two methods have been investigated, a method in which the lithium is applied on a mechanical way and a method in which electro-chemical transport is used.


Figure 2.7: Dry lithiation methods: (a) mechanical lithiation;(b) electrochemical alloying method.

*Mechanical lithiation*

Often a lithographic process occurs when scanning in contact mode on softer materials and surfaces. Scanning the surface with a certain force removes a small amount of material. In some cases, this material will be pushed to the sides of the scanning area, but in other cases, some of the material will stick to the tip. Because lithium is a fairly soft material, it has been investigated here to what extent it is possible to attach an amount of lithium to the tip using this scraping technique. Figure 2.7a shows a schematic representation of the mechanical lithiation method. The force with which the tip presses on a surface can be set very accurately with AFM equipment. By landing a cantilever probe with a high spring constant on a surface of metallic lithium with a controlled force and then rocking the probe back and forth, the tip of the lithium is scraped off the surface. It turns out that after this operation, some lithium remains on the tip.

For this method, a conductive diamond coated probe with a very high spring constant of typically 80 N/m was chosen (Nanosensors GmbH CDT-NCHR). A metal lithium disc (Sigma Aldrich) was pre-scraped smooth using a sharp doctor blade to remove any oxide layer from the surface, and was then used as the lithium-yielding substrate. To test whether the applied lithium can be electrochemically removed from the tip, a second substrate was positioned next to the lithium disc such that within the x-y plane of the probe control both substrates can be reached. For the second substrate a Silicon wafer (100) was deposited with a layer of gold (~100 nm) by Magnetron-sputtering (Cressington 208HR, MTM20 thickness controller) and covered with a smooth film of Ionic Liquid.



| | $f_{Li}$ (kHz) | $f_{dep}$ (kHz) | $\Delta f_r$ (±0.2kHz) | m (±0.28ng) |
|---|---|---|---|---|
| 1 | 405.7 | 425.9 | 26.2 | 1.40 |
| 2 | 406.5 | 426.7 | 25.4 | 1.36 |
| 3 | 401.1 | 429.2 | 30.8 | 1.67 |
| 4 | 415.4 | 429.2 | 16.5 | 0.87 |
| 5 | 397.5 | 416.5 | 34.4 | 1.89 |
| 6 | 405.7 | 420.0 | 26.2 | 1.40 |

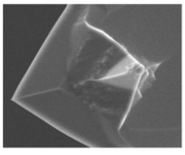

(a)

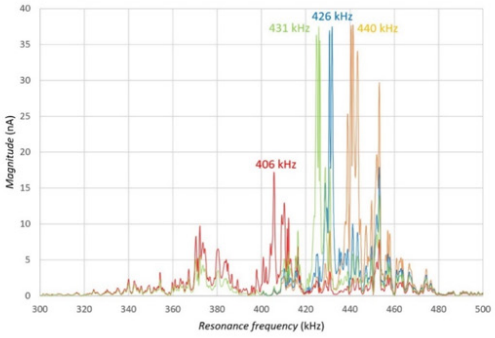


(b)

Figure 2.8: Resonance shift as result of lithiation by using the mechanical method followed by electrochemical de-lithiation. (a) the very end of the probe tip covered by a small amount of lithium; (b) the resonance spectra of different situations: orange = Pristine; Blue = after electrolyte dipping; Red = after mechanical plating on the tip; Green = after deposition back to the substrate

Referring to Figure 2.8, which shows the resonance frequency shift for four different situations, the working procedure for applying lithium to the tip and depositing lithium to the substrate is explained. The orange graph shows the frequency spectrum of the pristine and unused probe, with its highest (first order) peak at 440 kHz. First, the probe was brought to the surface of the substrate covered with ionic liquid and the correct height (deposition distance) was sought by gradually lowering the probe until the tip contacts the electrolyte film. When the probe has been lifted until contact with ionic liquid was broken, the free oscillating frequency spectrum was measured. The first order peak has been shifted to a value of 436 kHz (blue line in Figure 10) due to sticking ionic liquid at the tip end. Subsequently the probe was moved to the lithium substrate and was landed with a set force. The probe was moved over the surface back and forth a number of times to collect lithium at the tip by mechanical scraping. After this procedure the free oscillation spectrum was again measured and moved to lower values with the maximum peak shifted to 406 kHz (red line in Figure 10). Finally, the tip was brought back to the substrate covered with ionic liquid and carefully set at deposition distance. A small potential difference between tip and lithium sample was applied to force the lithium deposition to the gold layered substrate. After this, again the free oscillation spectrum was determined, where a shift of the highest peak was encountered to a value of 431 kHz (green line in Figure 10).

To demonstrate the reproducibility of this method, six times an amount of lithium was mechanically applied to the tip and electrochemically returned to the lithium substrate. With the measured resonance shift, the amount of lithium that was electrochemically returned to the substrate was calculated by using the model of 2.4.2. The Table in Figure 8 shows six consecutive measurements, with the measured shift, the corresponding calculated mass of lithium and the calculated standard deviation.

*Dry Electro chemical alloying and plating*

A relatively simple method for lithiating the tip of an AFM probe is achieved by establishing dry contact between a silicon probe tip and a metallic lithium substrate. Contact between these surfaces allows lithium to migrate to silicon, a very slow transfer process which is further limited by the fact that the contact is obtained only by the probe tip area that contacts the lithium substrate. However, the process can be accelerated by applying a potential between the tip and the lithium substrate, as shown in Figure 2.7b. In addition to this, the potential also helps bridge any oxide layer present on the lithium surface.

A conductive probe of Antimony doped single crystal Silicon (ND-MDT NSG30 N-type 0.01-0.025 mOhm.cm) was selected for dry electro-chemical alloying experiments. The relatively high spring constant (typical 40 N/m) creates a high pressure on the contact surface and the high resonance frequency (measured $f_0$ = 269.1505 kHz) enables the use of the frequency shift method for determining lithium mass. In the graph of Figure 2.9 the shift of the relative resonance frequency $f_n$ is shown as a function of the contact time t between the probe and the lithium substrate. During this experiment, the probe was lifted from the substrate every hour to monitor the free resonance frequency and thus the lithiation process. The experiment was conducted for ten hours. Subsequently, the free resonance frequency was followed for three weeks (measuring daily) to determine whether changes were measurable over time. During this period we monitored small variations around the resonance frequency which were comparable with the normal variations of an AFM probe due to long term temperature fluctuations. No permanent shift was observed, so it can be assumed that the probe has remained in the same dynamic state over the three weeks and no major changes have occurred.



Figure 2.9d shows a SEM photo of the probe tip after this lithiation experiment. It can clearly be seen that an alloying reaction has occurred, whereby the tip has expanded enormously. Moreover, the crystal orientation of the tip (100) seems to have created a preferred shape comparable to the structures found in the Nanopillar study of Lee et al (2011). Despite this successful lithitation, this probe can no longer be used for accurate AFM experiments due to its large dimensions (tip diameter ~ 5 micron). It was therefore investigated whether a short alloy-charging can be applied in which the probe tip is minimally deformed. Figure 2.9e shows the result of a charge procedure for ~15 minutes which results in a shift of the relative resonance to *fn* = 0.9998. The two extreme situations shown in Figure 2.9d and 2.9e provide insight into the range within which the tip can be lithiated. Depending on the desired scan accuracy, a certain deviation from the tip shape can be accepted and a choice can be made for a degree of lithiation.

The alloying experiments were repeated with a probe of the same composition as used above (Antimony doped single crystal Silicon), but with a lower resonance frequency and spring constant (ND-NDT NSG03, measured $f_0$ = 98.971 kHz, typical spring constant 1.74 N/m). These experiments have confirmed that lithium mass determination is less sensitive with a low resonance frequency and the lithiation process is more difficult due to the lower pressure of the tip on the lithium surface.

From various measurements it can be concluded that up to a potential of approximately 2 Volt between tip and sample, lithiating the tip leads to alloying of silicon with lithium. When the potential is increased, a second process, electro-chemical plating of the probe appears to occur. Figure 2.9b an 2.9c show SEM photos of a tip covered with a layer of lithium. During the SEM analysis, the crust was repelled by charging and parts of the normal tip surface became visible. From this, it can be assumed that the lithium applied by electrochemical plating has poor contact with the underlying probe.

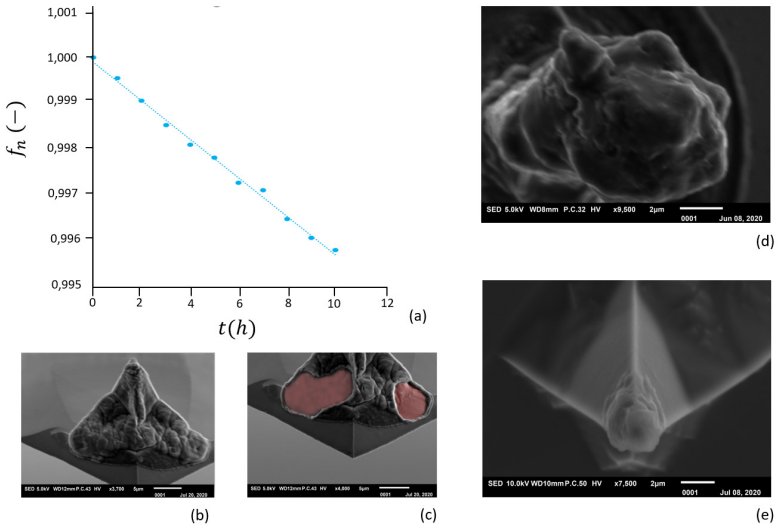


Figure 2.9: Lithiation of the tip by the dry-alloying (right) and the dry-plating method.

From the performed lithiation experiments it can be concluded that dry lithiation is the most applicable method, with the mechanical method and the alloying method giving the best results (see Table 1).

## Measurements with a lithiated probe

### Ion current measurements

The successfully lithiated probes have been used to investigate whether the probe can be used as an active element. Figure 10a schematically shows the measuring principle whereby an electrochemical cell is formed by bringing the probe into contact with a thin layer of electrolyte. In principle, a micro-scale battery has been created between the lithium-containing tip and the sample.

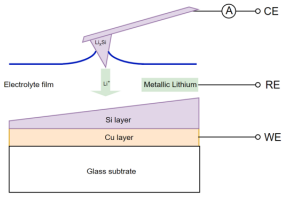


(a)

| | Position 1 [nA] | Position 2 [nA] |
|---|---|---|
| 1 | 1,255 | 1,323 |
| 2 | 1,186 | 1,316 |
| 3 | 1,203 | 1,359 |
| 4 | 1,226 | 1,39 |
| 5 | 1,159 | 1,317 |
| Average | 1,206 | 1,341 |
| SD | 0,037 | 0,033 |

(b)

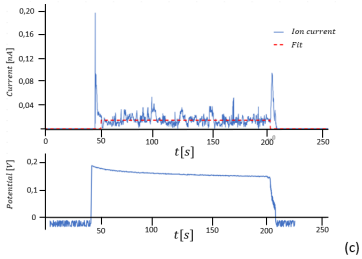


(c)

Figure 10: a) the lithiated probe as an active component in the battery process; b) and c) Ion current measurements.

To test the measuring principle of figure 10a, an accurate and flat sample has been obtained by means of sputter deposition techniques. A glass substrate (thickness 175 microns, 30x30 mm) is plated with a thin layer of copper (current collector) and Silicon (electrode layer). The substrate was cleaned with acetone and isopropanol and placed into a sputter deposition system (AJA Int. ATC 1800) with a pressure of < $10^{-8}$ mBar. After plasma cleaning (5 min. in Argon at 20 mBar and RF power of 24 W). First, 15 nm Ti was sputtered to improve adhesion with the substrate, after which a layer of copper of 300 nm was applied (15 min. in Argon at 5 mBar and RF power of 100 W). After this, the substrate was set off axis with respect to the target to obtain a thickness gradient in the applied layer. Finally a Silicon layer was deposited (37 min. in Argon at 5 mBar and RF power of 100 W) using a mask with a diameter of 2 mm. The thickness gradient of the film was verified using profilometry (DekTak 6M) and found to be 130-260 nm.

Electrochemical measurements where conducted in the argon filled AFM Glovebox system discribed In section 2.3.2. The sample was placed in the AFMAB cell (Figure 2.2) and connected as a working electrode. A thin layer of Ionic liquid was applied to the sample surface and spread over the entire area by fast rotating the sample holder. A small piece of lithium foil was placed on an uncovered glass side of the sample, in contact with the electrolyte to serve as a reference electrode. The electrodes are connected with the tip of the probe acting as the counter electrode, creating a three-electrode configuration. A potentiostat/Galvanostat (Metrohm Autolab PG-STAT302F) was used for measuring the potentials between sample and probe with respect to the lithium reference, while the current has been measured accurately by the *i*-probe current measurement of the AFM instrument.

We used a lithiated probe prepared by the electrochemical alloy method for ion-current measurements. Two positions with a difference in Silicon thickness have been selected on the sample. We then alternately landed the probe on the layer of Ionic liquid at both measuring points to measure the ion current for approximately 150 seconds. Because the ionic liquid behaves like a very elastic surface, the gain of the AFM control loop was set at a very low level (0,1) to avoid any unwanted corrections. By lowering the probe step by step, contact was made with the electrolyte, after which a potential was immediately measured and an ion current started to flow, see figure 2.10. Five separate measurements were taken at each measuring point. The obtained *i*-probe data was analyzed using *Gwyddion* SPM software (Gwyddion, 2019) for determining the average ion current excluding the start and end spike in the data (see red dotted line in the current plot of Figure 2.10). The two selected measuring points show a significant difference in ion current values, see the table in figure 2.10.

### Impedance measurements between tip and sample

The half-cell that can be created between a lithiated tip and an electrolyte covered sample allows very local non-faradaic impedance measurements. The typical probe-to-sample distance is very small due to the use of AFM, so the resolution of this measurement is on the order of the tip-radius. As far as we know, no research is known to determine the impedance as a function of frequency for battery research on this small scale. With the help of local impedance measurements, it is possible to quantify and compare differences in the sample surface and the processes that take place there. In addition, it can contribute to insights into the origin and composition of the SEI, and it provides opportunities to map impedance data over a surface by combining these measurements with AFM scans. Within the scope of this study, we note that the main goal of our impedance experiments is to demonstrate the possibilities of applying non-faradaic EIS in AFM measurements.

To minimize the influence of the tip on the total impedance, a conductive diamond-coated AFM cantilever with a relatively low resistance was chosen for this experiment (Nanosensors GmbH CDT-NCHR, Nominal force constant 80N/m, Typical tip resistance 3000 Ω). The probe was lithiated by the mechanical plating method so in fact a metallic lithium layer covers the tip end. EIS measurements were carried out with the coupled galvanostat / potentiostat (Metrohm Autolab PG-STAT302F). The AFM setup is located within the surrounding glovebox (see section 2.3.1) which functions as a faraday cage and so limits electrical noise. Measurement cables are shielded and cable lengths are balanced and minimized to limit stray capacitance.

Preliminary measurements have been made to determine the influence of the cables and the probe on the measurement and it has been found that the contribution of the equipment can be clearly distinguished from signals. Subsequently, a system is measured consisting of an lithium point (the tip), an electrolyte film (1M $LiPF_6$ in 1:1 EC/DMC) and a substrate of metallic lithium.

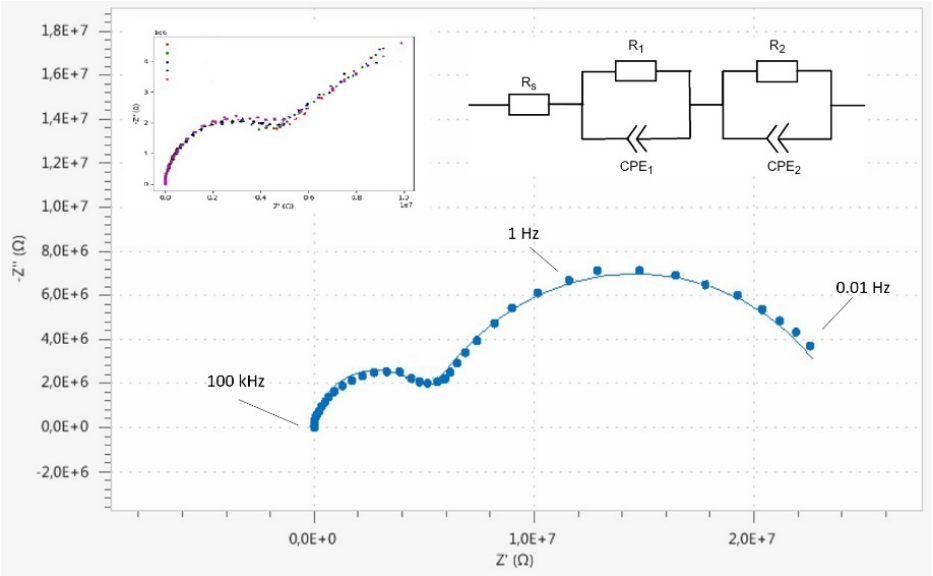


Figure 2.11: Impedance measurement with ionic contact via liquid electrolyte (1M $LiPF_6$ in 1:1 EC/DMC) between the lithiated tip and a metallic lithium sample. The measurement (00.1 Hz-100 kHz) consist of two semi circles which can be described with the equivalent circuit (inset top right). Calculated values (NOVA circuit fit, Metrohm Autolab) are $R_s$=600 Ω; $R_1$=19,5 MΩ; $CPE_1$=14,6 nF and n=0,79; $R_2$=4,95 MΩ; $CPE_2$=252 pF and n=0,96. Five short measurements (1Hz-100 kHz, Inset top-left) show the reproducibility of the measurement technique.

Figure 2.11 shows Cole-Cole plots of the EIS measurements. To prove the reproducibility, six individual short-time measurements (inset figure 2.11 top-left) were carried out within a frequency range of 1 Hz to 100 kHz, repeated at the same point and the same sample-probe distance. Subsequently, a longer measurement was taken in which the range was extended to lower frequencies (0,01 Hz-100 kHz), forming two semi-circles in the Cole-Cole plot which may very well be caused by processes at the lithium electrodes (Takami et al. 1992).

The equivalent circuit for this measurement is shown in figure 2.11 (inset top-right) and consists of two parallel *R/CPE* units and an ohmic resistance in series. The electrolyte resistance is represented by $R_s$, and charge transfer and typically diffusional processes at both electrodes are given by $R_1/CPE_1$ and $R_2/CPE_2$, respectively. It is however stressed that these processes of both charge transfer and diffusion occur at both electrodes and might be difficult to separate if the characteristic times of the process and geometric factors are simular. Since both electrodes are basically lithium and the charge, i.e. the ions, move practically though a similar surface area at both electrodes, the impedances due to both electrodes can be expected to be practically the same, and thus difficult to deconvolute.

## Discussion

The facility described here is suitable for performing *operando* measurements on batteries, in which it is possible to work under very low oxygen, moisture and vibration conditions. A conductive AFM-probe has access to battery electrodes and allows electrochemical measurements in the resolution range of approximately 20 to 200 nm. To enable measurements in which the probe is an active component of the battery, it has been investigated whether the probe can be supplied with an amount of lithium. Various methods have been tested whereby the dry lithiation methods give the best results. The lithium applied to a silicon tip by electrochemical alloying can be used in electrochemical measurements and the amount of lithium on the tip can be accurately determined by the shift of the Cantilever natural resonance frequency. By using ionic liquid as electrolyte, the probe can be applied to the tough liquid surface and measurements can be made to determine the ionic current. In fact, both the charging and the discharging processes (i.e. cycling) can take place between tip and sample. The amount of lithium absorbed into the tip by the alloying method must be carefully monitored as tip distortion occurs at the expense of probe scan resolution.

It appears that lithium can be brought to the tip by wet electrochemical plating, but cannot be removed in a controllable manner. The reverse process whereby lithium is brought from the tip to the sample is blocked by dendrites on the tip end. This layer of dendrite-shaped lithium is formed during the plating process and cannot be electro-chemically returned to the sample (Chen et al. 2017; Xiao 2019).

The mechanical scraping method (moving the needle over a lithium surface with some force) is a good way to provide the tip with lithium. The applied lithium can

be removed electro-chemically and can therefore be used as the electrode of a sub-micron battery, whereby only the discharging process can be applied. This method can be used to make a lithiated tip in a relatively simple way, whereby the amount of lithium can be measured directly with the frequency shift method. The applied lithium is metallic, which offers advantages for some measurements: the so formed *sub-micron half-cell battery* between lithiated tip and sample makes non-faradaic impedance measurements possible. Very local impedance can be measured and this information can be mapped and related to a specific sample position.

It is clear that the shift of the resonance frequency of an AFM cantilever is a measure for the mass transport between tip and sample, and can be used to determine the amount of lithium on the tip. The developed FEM model can be a useful tool.

The techniques described here and the results found have demonstrated that it is possible to use this facility and techniques to perform electrochemical experiments on a sub-micron to nano scale. This study shows that the use of lithiated tips offers great possibilities and offers a new addition to operando measurement techniques. The disadvantage is that the measurements are time consuming. However, lithiated tips can be kept in stock without degradation so that series of experiments can be prepared. The study has shown that the principles work. A follow-up study will focus on accurately drawing up assured measurement conditions, making series measurements possible.



The facility offers many possibilities, including research at the SEI, diffusion experiments, local impedance measurements, and measurements on redox processes and ion currents. It is desirable for EIS to be expanded with FFT (comparable to the work of Valiūnienė et al. 2019). This offers possibilities for mapping measurements in which entire impedance spectra can also be recorded. These measurements can be mapped as a function of the location on the sample by combining them with AFM surface scans, and so relationships between morphological and electrochemical properties can be investigated. Measurements are planned for the coming period in which we will use this facility and these methods to determine operando parameters.

## Generalized conclusions

Despite the technical difficulties, it has proved possible to provide the probe tip of an AFM with lithium and use it as an electrode in a laboratory battery. The resulting 'active probe' can be used for non-faradaic ion current and impedance

measurements. By demonstrating the measuring principle, the way is cleared to set up an automated 2d mapping method in which topographic, ion current and impedance measurements can be performed simultaneously. The thus created *Electrochemical Active Probe Microscopy* measurement-method can be a new technique for investigating battery processes on a sub-micron to nano scale.

# References


Amanieu, H.Y., Aramfard, M., Rosato, D., Batista, L., Rabe, U., Lupascu, D.C. (2015) Mechanical properties of commercial $Li_xMn_2O_4$ cathode under different States of Charge. *Acta Materials 89* 153-162

Arreaga-Salas, D. E., Sra, A. K., Roodenko, K., Chabal, Y. J., & Hinkle, C. L. (2012). Progression of solid electrolyte interphase formation on hydrogenated amorphous silicon anodes for lithium-ion batteries. *The Journal of Physical Chemistry C*, *116*(16), 9072-9077.

Bandarenka, A. S., Eckhard, K., Maljusch, A., & Schuhmann, W. (2013). Localized electrochemical impedance spectroscopy: Visualization of spatial distributions of the key parameters describing solid/liquid interfaces. *Analytical chemistry*, *85*(4), 2443-2448.

Bard, A. J., Fan, F. R. F., Kwak, J., & Lev, O. (1989). Scanning electrochemical microscopy. Introduction and principles. *Analytical Chemistry*, *61*(2), 132-138.

Bauchau, O. A., & Craig, J. I. (2009). Euler-Bernoulli beam theory. In *Structural analysis* (pp. 173-221). Springer, Dordrecht.

Bhiladvala, R. B., & Wang, Z. J. (2004). Effect of fluids on the Q factor and resonance frequency of oscillating micrometer and nanometer scale beams. *Physical review E*, *69*(3), 036307.

Binnig, G., & Rohrer, H. (1983). Scanning tunneling microscopy. *Surface science*, *126*(1-3), 236-244.

Binnig, G., Quate, C. F., & Gerber, C. (1986). Atomic force microscope. *Physical review letters*, *56*(9), 930.

Boisen, A., Dohn, S., Keller, S. S., Schmid, S., & Tenje, M. (2011). Cantilever-like micromechanical sensors. *Reports on Progress in Physics*, *74*(3), 036101.

Breitung, B., Baumann, P., Sommer, H., Janek, J., & Brezesinski, T. (2016). In situ and operando atomic force microscopy of high-capacity nano-silicon based electrodes for lithium-ion batteries. *Nanoscale*, *8*(29), 14048-14056.

Benning, S., Chen, C., Eichel, R. A., Notten, P. H., & Hausen, F. (2019). Direct Observation of SEI Formation and Lithiation in Thin-Film Silicon Electrodes via in Situ Electrochemical Atomic Force Microscopy. *ACS Applied Energy Materials*, *2*(9), 6761-6767.

Bruker, (2020) *Battery characterization using AFM* Visited on 20-02-2020 through https://www.bruker.com/products/surface-and-dimensional-analysis/atomic-force-microscopes/campaigns/battery-characterization-using-afm.html

Chen, K., Wood, K.A., Kazyak, E., LePage, W.S., Davis, L.A., Sanchezband, A.J., Dasgupta, N.P. (2017) Dead lithium: mass transport effects on voltage, capacity and failure of lithium metal anodes. *Journal of materials chemistry* DOI: 10.1039 / c7ta00371d

Diakowski, P. M., & Ding, Z. (2007). Interrogation of living cells using alternating current scanning electrochemical microscopy (AC-SECM). *Physical Chemistry Chemical Physics*, *9*(45), 5966-5974.

Demirocak, D. E., & Bhushan, B. (2014). In situ atomic force microscopy analysis of morphology and particle size changes in lithium iron phosphate cathode during discharge. *Journal of colloid and interface science*, *423*, 151-157.

Demirocak, D. E., & Bhushan, B. (2015). Probing the aging effects on nanomechanical properties of a LiFePO4 cathode in a large format prismatic cell. *Journal of Power Sources*, *280*, 256-262.

Doi, T., Inaba, M., Tsuchiya, H., Jeong, S.K., Iriyama, Y., Abe, T., Ogumi, Z. (2008) Electrochemical AFM study of $LiMn_2O_4$ thin film electrodes exposed to elevated temperatures. *Journal of Power Sources 180* 539-545

Eckhard, K., Kranz, C., Shin, H., Mizaikoff, B., & Schuhmann, W. (2007). Frequency dependence of the electrochemical activity contrast in AC-scanning electrochemical microscopy and atomic force microscopy-AC-scanning electrochemical microscopy imaging. *Analytical chemistry*, *79*(14), 5435-5438.

Espinoza Beltran, F.J., Munoz-Saldana, J., Torres-Torres, D., Torres-Martinez, R., Schneider, G.A. (2006) Atomic force microscopy cantilever simulation by finite element methods for quantitative atomic force acoustic microscopy measurements. J. *Materials Research Vol. 21* No. 12

Garcia-Tamayo, E. (2014) Advanced thin layer deposition of materials for Li-ion batteries via electrospray [dissertation]. *Delft University of Technology*

Gwyddion (2019). Visited on 20-02-2020 through www.gwyddion.net.

Huang, S., Cheong, L., Wang, S., Wang, D., Shen, C. (2018) In-situ study of surface evolution of silicon anodes by electrochemical atomic force microscopy. *Applied Surface Science 452* 67-74

Inaba, M., Jeong, S. K., & Ogumi, Z. (2011). In situ scanning probe microscopy of interfacial phenomena in batteries. *Electrochemical Society Interface*, *20*(3), 55.

Injeti, S. S., & Annabattula, R. K. (2016). Extending Stoney's equation to thin, elastically anisotropic substrates and bilayer films. *Thin Solid Films*, *598*, 252-259.

Kim, S. H., Kim, Y. S., Baek, W. J., Heo, S., Han, S., & Jung, H. (2018). Nanoscale electrical resistance imaging of solid electrolyte interphases in lithium-ion battery anodes. *Journal of Power Sources*, *407*, 1-5.

Korayem, M.H., Sharahi, H.J., Korayem, A.H. (2012) Comparison of frequency response of atomic force microscopy cantilevers under tip-sample interaction in air and liquids. *Scientia Iranica 19* 106-112.

Lee, S. W., McDowell, M. T., Choi, J. W., & Cui, Y. (2011). Anomalous shape changes of silicon nanopillars by electrochemical lithiation. *Nano letters*, *11*(7), 3034-3039.

Lam, L., Bauer, P., Kelder, E.M. (2011) A practical circuit based model for Li-ion battery cells in electric vehicle applications, *IEEE* 978-1-4577-1250-0.

Morkvenaite-Vilkonciene, I., Valiūnienė, A., Petroniene, J., & Ramanavicius, A. (2017). Hybrid system based on fast Fourier transform electrochemical impedance spectroscopy combined with scanning electrochemical microscopy. *Electrochemistry Communications*, *83*, 110-112.

Nagpure, S.C., Bhushan, B., Babu, S.S. (2010) Surface potential measurement of aged Li-ion batteries using Kelvin probe microscopy. *Journal of Power Sources 196* 1508-1512.

Nagpure, S.C. Bhushan, B., Babu, S.S. (2013) Multi-scaled Characterization of aged Li-ion battery materials for improving performance: an overview. *Journal of electrochemical society 160* A2111 A2154.

Nanosensors, (2020) *Conductive Diamant Coated Tip Non Contact Tapping Mode* Visited on 20-02-2020 through https://www.nanosensors.com/conductive-diamond-coated-tip-non-contact-tapping-mode-high-resonance-frequency-reflex-coating-afm-tip-CDT-NCHR

O'Hayre, R., Lee, M., Prinz, F.B. (2004, June) Quantitative impedance measurement using atomic force microscopy. *Journal of applied physics 95* 12 8382-8392

O'Hayre, R., Feng, G., Nix, W.D., Prinz, F.B. (2004, September) Ionic and electronic impedance imaging using atomic force microscopy. *Journal of applied physics 95* 12 8382-8392

Mahankali, K., Thangavel, N. K., & Reddy Arava, L. M. (2019). In Situ Electrochemical Mapping of Lithium–Sulfur Battery Interfaces Using AFM–SECM. *Nano letters*, *19*(8), 5229-5236.

Payam, A. F., & Fathipour, M. (2009). Modeling and dynamic analysis of atomic force microscope based on Euler-Bernoulli beam theory. *Dig J Nanomater Biostruct*, *4*(3), 565-578.

Payam, A.F., Fathipour, M. (2014) Effect of tip mass on frequency response and sensitivity of AFM cantilever in liquid. *Micron 70* 50-54

Poggi, M.A., McFarland, A.W., Colton, J.S., Bottomley, L.A. (2005) A Method for Calculating the Spring Constant of Atomic Force Microscopy Cantilevers with a Nonrectangular Cross Section. *Analytical Chemistry* 77-4 1192-1195

Polcari, D., Dauphin-Ducharme, P., Mauzeroll, J. (2016) Scanning electrochemical microscopy: A comprehensive review of experimental parameters from 1989 to 2015. *Chemical Reviews 116* 13234-13278 doi: 10.1021/acs.chemrev.6b00067

Sader, J. E. (1998). Frequency response of cantilever beams immersed in viscous fluids with applications to the atomic force microscope. *Journal of applied physics*, *84*(1), 64-76.

Sakai, H., Taniguchi, Y., Uosaki, K., & Masuda, T. (2019). Quantitative cross-sectional mapping of nanomechanical properties of composite films for lithium ion batteries using bimodal mode atomic force microscopy. *Journal of Power Sources*, *413*, 29-33.

Takami, N., Ohsaki, T., & Inada, K. (1992). The Impedance of Lithium Electrodes in LiPF6-Based Electrolytes. *Journal of the Electrochemical Society*, *139*(7), 1849.

Valiūnienė, A., Petroniene, J., Morkvenaite-Vilkonciene, I., Popkirov, G., Ramanaviciene, A., & Ramanavicius, A. (2019). Redox-probe-free scanning electrochemical microscopy combined with fast Fourier transform electrochemical impedance spectroscopy. *Physical Chemistry Chemical Physics*, *21*(19), 9831-9836.

Valiūnienė, A., Sabirovas, T., Petronienė, J., & Ramanavičius, A. (2020). Towards the application of fast Fourier transform-scanning electrochemical impedance microscopy (FFT-SEIM). *Journal of Electroanalytical Chemistry*, 114067.

**Vincent, L.T., Weddle, P.J., Tang, G. (2017)** System theoretical analysis or battery charging optimization. *Journal of energy storage 14-1* 168-178

**Wang, L., Deng, D., Lev, L. C., & Ng, S. (2014).** In-situ investigation of solid-electrolyte interphase formation on the anode of Li-ion batteries with Atomic Force Microscopy. *Journal of Power Sources*, *265*, 140-148.

**Wang, S., Zhang, W., Chen, Y., Dai, Z., Zhao, C., Wang, D., & Shen, C. (2017).** Operando study of Fe3O4 anodes by electrochemical atomic force microscopy. *Applied Surface Science*, *426*, 217-223.

**Wittstock, G., Burchardt, M., Pust, E.S., Shen, Y., Zhao, C. (2007).** Scanning Electrochemical Microscopy for direct imaging of reaction rates. *Angewante Chemie 46* 1584-1617

**Xiao, J. (2019).** How lithium dendrites form in liquid batteries. *Science*, *366*(6464), 426-427.

**Yang, S., Wu, J., Yan, B., Li, L., Sun, Y., Lu, L., Zeng, K. (2017).** Nanoscale characterization of charged/discharged lithium-rich thin film cathode by scanning probe microscopy techniques. *Journal of Power Sources* 352 9-17

**Yu, D., Gryzlov, T.L., Alexenko, A.E., Spitsyn, B.V., Skundin, A.M. (2018)** The possibility of electrochemical lithium intercalation into a nanodiamond. *Mendeleev Communications* 28-6 666-667

**Zhang, J. X., & Hoshino, K. (2018).** *Molecular Sensors and Nanodevices: Principles, Designs and Applications in Biomedical Engineering*. Academic Press.

**Zhang, Z., Smith, K., Jervis, R., Shearing, P. R., Miller, T. S., & Brett, D. J. (2020).** Operando Electrochemical Atomic Force Microscopy of Solid–Electrolyte Interphase Formation on Graphite Anodes: The Evolution of SEI Morphology and Mechanical Properties. *ACS Applied Materials & Interfaces*, *12*(31), 35132-35141.

# CHAPTER THREE

## *Characterization of initial effects in porous silicon anode material using Positron Annihilation Doppler Broadening Spectroscopy*

This chapter is based on: Legerstee, W. J., Noort, T., van Vliet, T. K., Schut, H., & Kelder, E. M. (2022). Characterisation of defects in porous silicon as an anode material using positron annihilation Doppler Broadening Spectroscopy. *Applied Nanoscience*, *12*(11), 3399-3408.

# Characterization of initial defects in porous silicon anode material using Positron Annihilation Doppler Broadening Spectroscopy

## Introduction

The automotive industry needs higher energy densities for lithium ion batteries. To achieve this, a great deal of research is being conducted into new materials, including anode materials. An interesting candidate as anode material is silicon, which forms an alloy with lithium according to the reaction equation of eq 3.1 (in Chapter 4 the reaction between Li and Silicon is discussed in detail).

$$4Si + 15Li^{+} + 15e^{-} \xrightarrow{3579\ \mathrm{mAh}\cdot g^{-1}} Li_{15}Si_{4} \qquad \text{(Eq 3.1)}$$

Silicon is seen as the next-generation anode material in Li-ion batteries because its theoretical capacity of 3579 mAh $g^{-1}$ (based on $Li_{15}Si_4$) is up to more than ten times higher than the commonly used graphite anodes with a theoretical capacity of approx. 372 mAh $g^{-1}$ (Li & Dahn 2007; Liu & Huang 2011). However, silicon's ability to alloy with lithium results in a large volume expansion up to 300-400 percent. The mechanical stresses created by volume expansion cause cracking and particle pulverization, resulting in electrically disconnected small particles and poor contact with the current collector, followed by capacitance loss and anode degradation (Beaulieu et al. 2001). To overcome these major drawbacks, several research groups have sought ways to accommodate these extreme volume changes. One of the possible solutions is the incorporation of small open volumes, e.g. voids, in silicon structures at which a large part of the volume increase can be absorbed thus preventing the formation of cracks in the silicon anode material (McDowell et al. 2013; Shen et al. 2016; Shin et al. 2005), as illustrated schematically in figure 3.1.

In the past decade various structural material designs containing open volumes have been developed, among which silicon-carbon composites (Kim et al. 2018), silicon nanowires (Zamfir et al. 2013; Salihoglu et al. 2019) hollow nano structures (Yeom et al. 2019; Wang et al. 2018), and nano structured layers (Tang et al. 2019; Cho 2010). However, many of these methods have the significant drawback of being based on advanced deposition techniques capable of producing only small amounts of material, making it unsuitable for use in the automotive industry where large-scale electrode material production is required. Therefore, many research groups have

focused on scalable methods for the production of micro-sized particles containing nano-sized porosity (Whang et al. 2020; An et al. 2019; Ge et al. 2013; Zhang et al. 2014) which can be processed into battery electrodes using the well-known tape-casting methods (Shanefield, 1991).

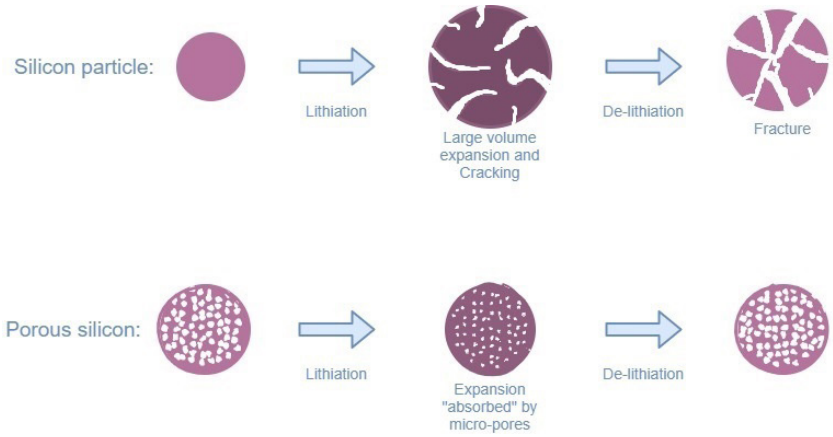


Figure 3.1: The principle of absorbing the extreme expansion of a particle and avoiding the formation of cracks due to silicon lithiation by structures containing small open volumes.

However, the use of porous materials in commercial batteries requires insight into the limitations due to the degradation processes caused by charging and discharging the anode material repeatedly (cycling). In addition to the more usual analysis methods, like long term cycling tests, electrochemical impedance analysis, intermittent titration techniques and cyclic voltametric analysis, researchers use various advanced analysis methods, including Transmission Electron Microscopy (Shen et al. 2016; McDowell et al. 2012), acoustic emission (Kalnaus et al. 2011; Rhodes et al. 2010), Atomic Force Microscopy (Vidu et al. 2002; Huang et al. 2018) and Nuclear Magnetic Resonance (Key et al. 2011). More recently, methods such as X-ray Compton scattering spectroscopy (Suzuki et al. 2016) and positron annihilation spectroscopy (Klinser et al. 2019; Seidlmayer et al. 2016) have been used to investigate the presence and change of defects as a result of lithium extraction and uptake in cathode electrode materials. Here we present Positron Annihilation Doppler Broadening Spectroscopy (DBPAS) as a new additional powerful technique for the defect characterization of silicon anodes. Due to its high sensitivity to open volume defects (Krause-Rehberg & Leipner 1999) we have applied this technique for the study of early stage crack formation. The value of this method is demonstrated on porous silicon anodes by determining a critical charging capacity above which

the defect structure is changing. The change in DBPAS parameters is related to premature fracture of the porous particles caused by the expansion of the silicon as a result of the alloying process with lithium. For this study we use porous silicon that has been successfully and scalable produced and which is available as a bulk material for anode preparation (E-magy, 2020).

## Experimental

*Positron Annihilation Doppler Broadening Spectroscopy*

Positron Annihilation Spectroscopy (PAS) is a well-established nondestructive technique for characterization of defects , voids and open volumes in materials (Schultz & Lynn 1988), and is used in many fields of material science (Tuomisto and Makkonen, 2013). The use of positron annihilation as a probe allows for the detection of defect concentrations in the order of 0.1 ppm (Smedskjaer et al. 1980) which makes this technique extremely sensitive. Several positron measurement principles are known (Krause-Rehberg & Leipner 1999) and used for almost 50 years to characterize defects in materials. The method we use here is the so-called Variable Energy Positron beam Doppler Broadening technique, which measures the Doppler shift in the energy of the 511 keV annihilation gammas emitted when a positron annihilates.



Positrons are anti-matter particles and can be created by materialisation of radiation ($e^+/e^-$ pair production) or are obtained by $\beta^+$ decay. For the latter usually a $^{22}Na$ positron source is used which emits positrons with kinetic energies distributed according to a so-called beta-spectrum. In order to obtain a beam of positrons with tunable, well defined energies the positrons emitted by the $^{22}Na$ source are slowed down to an energy of ~2.5 eV by using a Tungsten moderator. These moderated positrons are then accelerated to selected energies (practically between 0.1- 25 keV) and targeted on a material of interest. When implanted in a sample with an initial kinetic energy well above the thermal energy the positrons rapidly lose their energy. When thermal equilibrium is reached, positron-electron annihilation can take place, most likely resulting in the collinear emission of two 511 keV photons. Due to the momentum of the positron-electron pair (mainly determined by the electron motion) the photon energies show a Doppler shift which causes a broadening of the annihilation energy distribution when observed by an energy selective spectrometer. The shape of the obtained energy spectrum is related to the presence and type of defects and is commonly characterized by the so-called *shape parameters S and W*, as shown in figure 3.2[a]. The *S* parameter is

experimentally determined as the relative area of the central part of the energy distribution spectrum, while the *W* parameter expresses the relative contributions of the tails to the total peak area (Clement et al. 1996). Thus, the *S* parameter is a measure for the contribution of lower momentum (valence) electrons, while the *W* parameter represents annihilations with the higher momentum (core) electrons. By determining these parameters for a series of implantation energies (related to depth), defect depth distributions and characterization of open volume defects in sub-surface regions can be obtained. The defect *S* parameter is most sensitive to defects because the probability for a positron to annihilate with high momentum outer shell electrons of defect neighboring atoms is lower, thus increasing the contribution of low momentum annihilations in the 511 keV photo-peak.

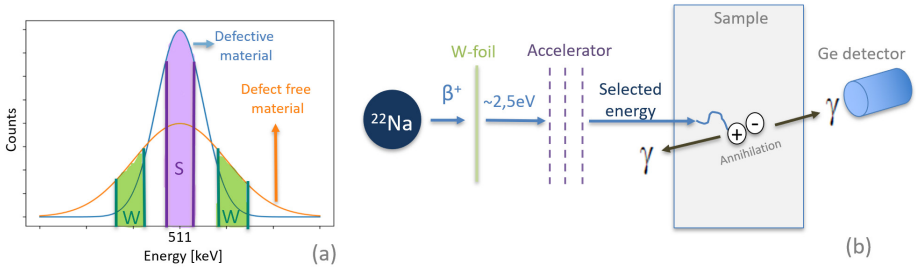


Figure 3.2: (a) Energy distribution spectra of a defect-free sample (orange) and a defective material (blue), and the shape parameters *S* (purple) and *W* (green). (b) DBPAS measurement principle for single detector mode in which one out of the two Gamma rays is detected

*The variable Energy Positron Beam*

For Positron Annihilation Doppler Broadening Spectroscopy (DBPAS) measurements we used the Delft Variable Energy Positron Beam (VEP), containing a $^{22}$Na positron source (1 GBq) to produce a mono-energetic, magnetically guided positron beam (~$10^5$ e+ .$s^{-1}$) with a diameter of 8 mm and variable acceleration energy ranging from 1 to 25 keV for depth selective probing. The corresponding depth range can be determined from the following power law (Schultz and Lynn, 1988):

$$\bar{z} = \frac{A}{\rho} E^n \qquad \text{(Eq 3.2)}$$

where $\bar{z}$ is the mean implantation depth (in Å), ρ is the density of the target material (2.3 g.cm$^{-3}$ for Si), A is a constant empirically found to be $A \approx 400 \text{Å}.g.cm^3.keV^{-n}$ and

$n \approx 1.6$ for most materials (Lynn and Lutz, 1980). The maximum average implantation depth can be determined for silicon at approximately 3μm for 25 keV positrons. Energy selective measurements of the annihilation radiation are performed with a high purity Ge solid state detector (Canberra, energy resolution 1.8 keV@1.33 MeV) in single-detector mode (as shown schematically in figure 3.2[b]). For analysis of the obtained *S* and *W* parameter the data fitting and modelling algorithm VEPFIT is used (Van Veen et al. 1991).

*Lithiation of porous silicon*

The electro-chemical lithiation process of crystalline silicon (c-Si) is a two phase alloying process with a sharp reaction front (Chon et al. 2011; Obrovac & Christensen, 2004). During the first lithiation c-Si is transformed to an amorphous $Li_xSi$ alloy ($0<x<3.4$) forming a distinct voltage plateau in the potential curve (first discharge part in figure 3.5) around 0,1 V versus $Li^+/Li$ (indicating the two phase addition reaction between Si and Lithium), and with a volume change of ~300% (for x=3.4). Further (or deep) lithiation to a voltage under ~0.05 V will form a crystalline and metastable $Li_{15}Si_4$ alloy which is the final lithiated product for electro-chemical alloying at room temperature (Obrovac & Christensen, 2004; Kubota et al. 2007). In dealloying (extract lithium), the crystalline structure ($Li_{15}Si_{4)}$ will revert to amorphous $Li_ySi$ ($y\approx2$) by a two phase reaction at a distinct plateau at ~0.4 V, followed by a solid-solution reaction from amorphous $Li_ySi$ to amorphous silicon (a-Si) when completely de-lithiated (Zang 2011). The second and subsequent alloying and de-alloying cycles show up a voltage profile which is different from the first, as can be seen in figure 3.5. For better cycling performance it is recommended to avoid the forming of the crystallized $Li_{15}Si_4$ phase by setting the lower voltage limit on 50 mV. (Li & Dahn 2007; Ozanam & Rosso 2016).

The shape of the voltage profiles for Si-anodes are affected, among other things, by the morphological properties of the used silicon material. Anodes that contain silicon with different porosity structure or particle size show up slightly different voltage profiles (different slopes of the curves) because alloying processes are highly influenced by the ratio between surface/interface processes and particle volume (Zhang 2011). In figure 3.5 the voltage profile of the material used for this study is shown.

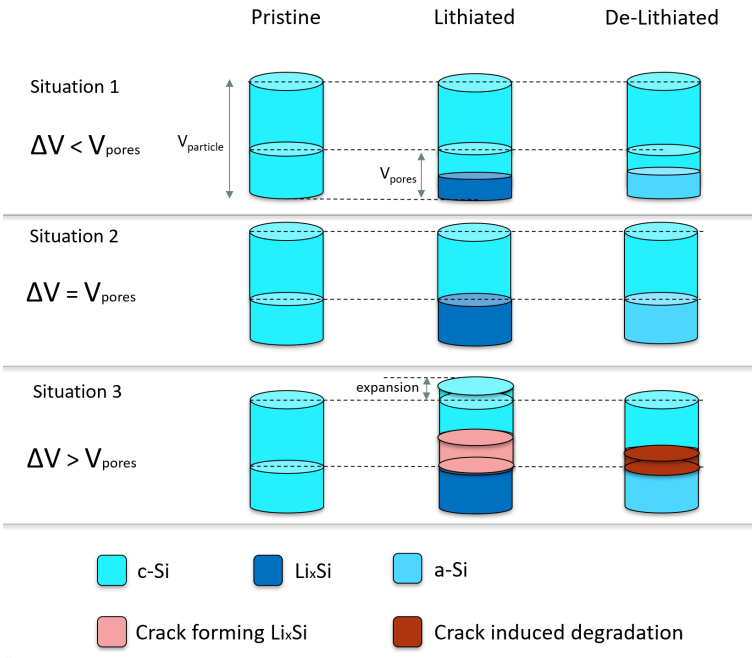


Figure 3.3: Schematic represenatation of volume expansion compensation and limits by porous silicon

Several studies have indicated that particularly during the very first lithiation, extensive damage occurs in the c-Si structure (Kalnaus et al. 2011; McDowell et al. 2013). With porous Si structures, the occurrence of damage is partly determined by the ability of the open volumes to absorb the expansion. Thus for using these materials in commercial batteries it is important to know the limit of lithiation before cracking occurs. This means, the theoretical capacity of 3579 mAh $g^{-1}$ will not be fully used, but instead the maximum capacity without fracture ($C_{max}$) will be the desired value at which the anode material can be used with minimal degradation over longer time. For porous silicon, $C_{max}$ is determined by the ability of the porosities to compensate for volume changes due to lithiation. In figure 3 a simplified pore-compensation mechanism is schematically shown wherein the occurring volume change due to alloying ($\Delta V_{alloying}$) is compared with the compensating pore volume ($V_{pores}$). The first situation when $\Delta V_{alloying} < V_{pores}$ will prevent damage because the discharged capacity ($C_d$) is below $C_{max}$. The second situation is the equilibrium state where $\Delta V_{alloying} = V_{pores}$ where $C_d$ will be equal to $C_{max}$, that is the status we want to approach as closely as possible. In the third situation, $\Delta V_{alloying} > V_{pores}$ , the value of $C_d$ exceeds $C_{max}$ resulting that some of the expansion will cause fractures

and permanent damage will occur. Determining the critical value of $C_{max}$ is very valuable because in addition to preventing damage, the capacity to be used can be accurately determined so that the material can be used optimally.

*Atomic Force Microscopy analysis*

The expansion of the porous Si as a result of lithium alloying is analyzed with an Atomic Force Microscope (AFM) (Ntegra NT-NDT) which is located in a glovebox under inert atmosphere (Legerstee et al. 2021). An open cell design allows the AFM probe (Pointprobe CDT-NCHR) to access the surface of a flat sample. After a scan it is possible to lithiate the sample by adding electrolyte to the surface, after which the surface should be carefully cleaned of the electrolyte so a new scan of the surface can be made.

*Sample preparation*

Porous c-Si was obtained from E-magy in two different appearances, as half product (so called 'flakes' with typical sizes of one or more square centimeters) and in the form of 2-6 micron sized particles. The flakes are used for additional surface analysis by Scanning Electron Microscopy (SEM) (JEOL JSM-IT100) and AFM, while the particles are used to prepare electrodes by a doctor blade casting method. Fig 3.4[a] shows a SEM photo of the base material (flake). Due to the pores of the material (200-600nm), a porosity of approximately 35 % is obtained (according to the specs of the supplier). The XRD pattern of the porous c-Si confirms the presence of a crystalline phase (figure 3.4[b]).

Electrodes were prepared by mixing 80% porous Silicon particles with 10% Carbon Black, 10% Polyacrylic Acid (PAA) in a buffered citric acid solution was added to make a slurry. The slurry was coated on copper foil which acts as current collector for the prepared electrode and dried in a vacuum oven (60 °C for 12 h). Figure 3.4[c] and 3.4[d] shows a SEM picture of the prepared electrode and a detail of a porous particle. The anode sheets were cut into discs (diameter 12.7 mm) and assembled in an argon filled glovebox as a half-cell with lithium metal as a counter and reference electrode. To avoid the release of the anode material when dismounting the cells after cycling, we used a glass fiber membrane on the lithium metal side as a separator and polypropylene membrane (Cellgard 2400) on the silicon side, the former ensuring a stable amount of electrolyte. A dismountable laboratory cell (airtight mounted stainless steel poles separated by a PTFE gasket) was used to prepare the batteries with 1M solution of $LiPF_6$ in 1:1 (vol.%) ethylene carbonate (EC):dimethyl carbonate

(DMC) as electrolyte. The samples were lithiated (discharged against $Li^+/Li$) and de-lithiated (charged) with c-rates based on 1C=1000 $mAh.g^{-1}$, that is the capacity at which the porous material has been extensively tested and still shows capacity retention after 100 cycles (specified by the manufacturer).



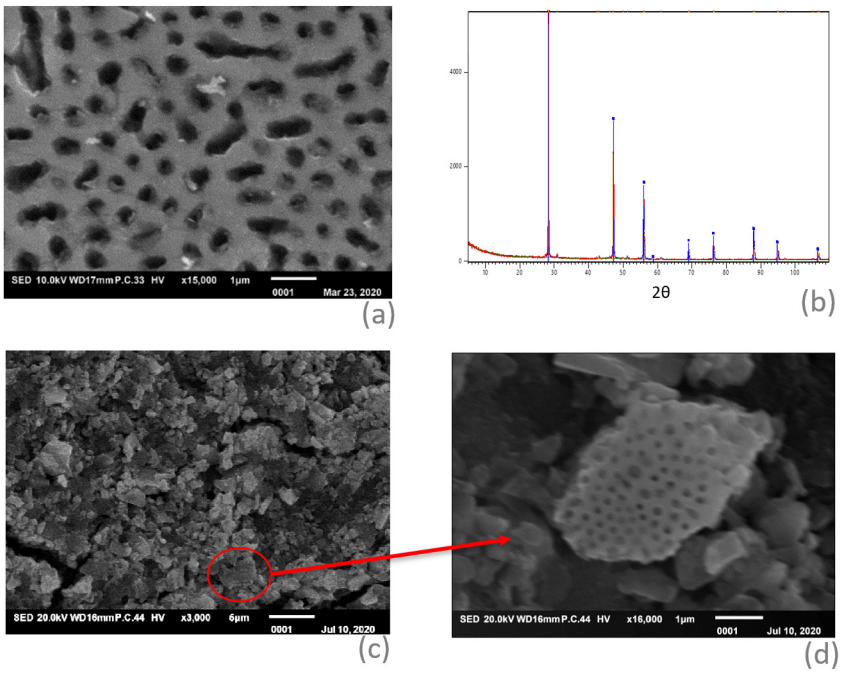


Figure 3.4: (a) SEM picture of flake surface; (b) XRD patern c-Si flake; (c) SEM picture of prepared anode (80m% porous Si); (d) SEM detail of a porous particle.

Electro-chemical tests were carried out using a Maccor™ battery tester, and conducted under constant current conditions with a lower voltage limit at 0.05 V for preventing the formation of the unwanted crystalline $Li_{15}Si_4$ phase. The upper limit was set on 1 V for de-lithiation. We performed ten measurements with different values for $C_d$ varying between 50 and 3000 $mAh.g^{-1}$. The samples were cycled for 2 times at a current of 0.1C followed by a final de-lithiation step. In figure 3.5 an example of the cycling procedure is given. Here the first cycle is the so called 'Format step', followed by a full second cycling step. The last part, the final de-lithiation step, is added to extract as much as possible the lithium by charging (de-alloying) the sample repeatedly under a constant voltage of 1V against $Li^+/Li$.

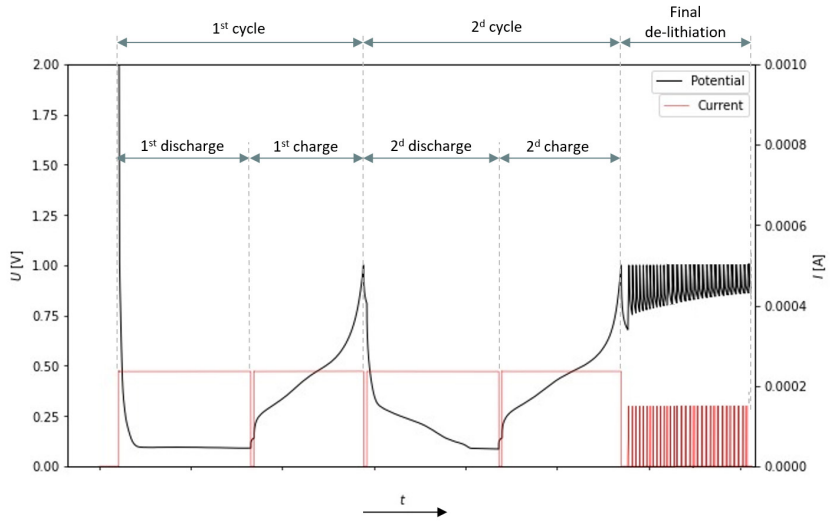


Figure 3.5: Cylcling procedure of porous silicon anode samples in a half-cell configuration (metallic lithium as a counter and reference electrode).



After the discharge/charge procedures the samples were prepared for DBPAS measurements. The cells were dismounted in an airtight glovebox filled with argon (<1 ppm oxygen and moisture) and the anode samples were carefully removed from the separator, after which they are rinsed in Dimethyl Carbonate for 10 minutes under stirring conditions. The samples were then dried under vacuum for 20 minutes and placed in a sample holder for positron measurements. The sample holder was transported to the DBPAS facility in an air-tight box. The positron setup was flushed with $N_2$ during the placement of the samples, and samples were transferred to the set-up within 1 second, so that minimal contamination with air has occurred. The DBPAS setup was brought to vacuum level of $1.10^{-6}$ mbar after which the positron measurements for 48 different implantation energies have started.

## Results and discussion

Figure 3.6a shows an AFM scan of a pristine flake where the pores are clearly visible. After the scan we added electrolyte to the surface and started the lithiation process for 48 hours with a discharge current of 12.5 μA.cm$^{-2}$, after which we removed the electrolyte and performed a new scan. Figure 3.6b shows the lithiated state of the flake, which confirms the volume absorption by pores and a change of surface as a result of alloying with lithium on the surface.

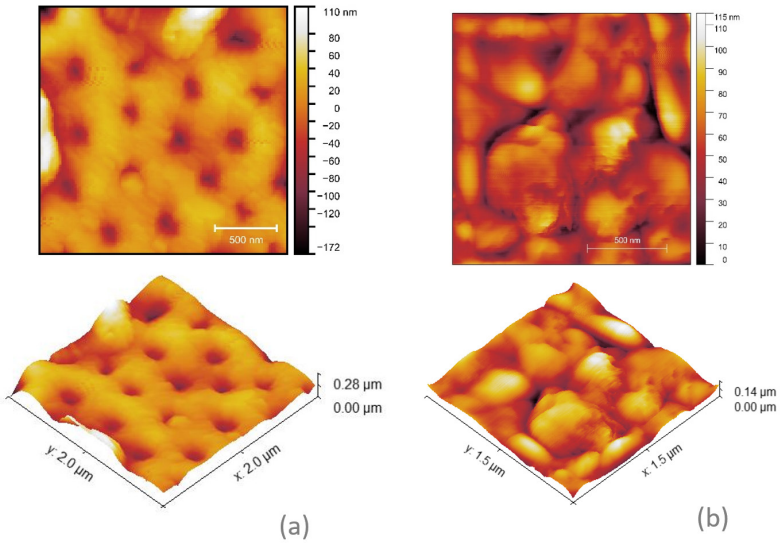


Figure 3.6: AFM scans of (a) pristine and (b) Highly lithiated flake surface.

*DBPAS results*

Ten samples were cycled according to the procedure described above (Figure 3.5), using the following values for the total discharged capacity $C_d$: 50, 150, 250, 350, 700, 1000, 1500, 2000, 2500 and 3000 mAh.g$^{-1}$. We performed DBPAS measurements on all samples including a pristine sample which was stored under electrolyte for 48h and treated the same way as all other samples. Figure 3.7[a] and 3.7[b] shows the measured (dots) and fitted (line) *S* parameter and *W* parameter as a function of implantation energy for three samples: the pristine sample, and samples with discharge capacities of $C_d$ =1000 mAh.g$^{-1}$ and $C_d$ =2000 mAh.g$^{-1}$. The pristine sample shows a relatively flat *S*-plot and *W*-plot while the cycled samples show a slope on both *S* and *W* parameter between approximately 0-7 keV, which reveals the difference in annihilation characteristics at the surface in comparison to those in the deeper Li affected regions. For higher energies the curve forms a relatively constant S and W which is related to the deeper located bulk material. For this study, we limit ourselves to analyzing the differences in the bulk level of the *S* and *W* parameters of energies between 7-25 keV (indicated by the vertical gray dashed line in figure 3.7[a] and 3.7[b]).

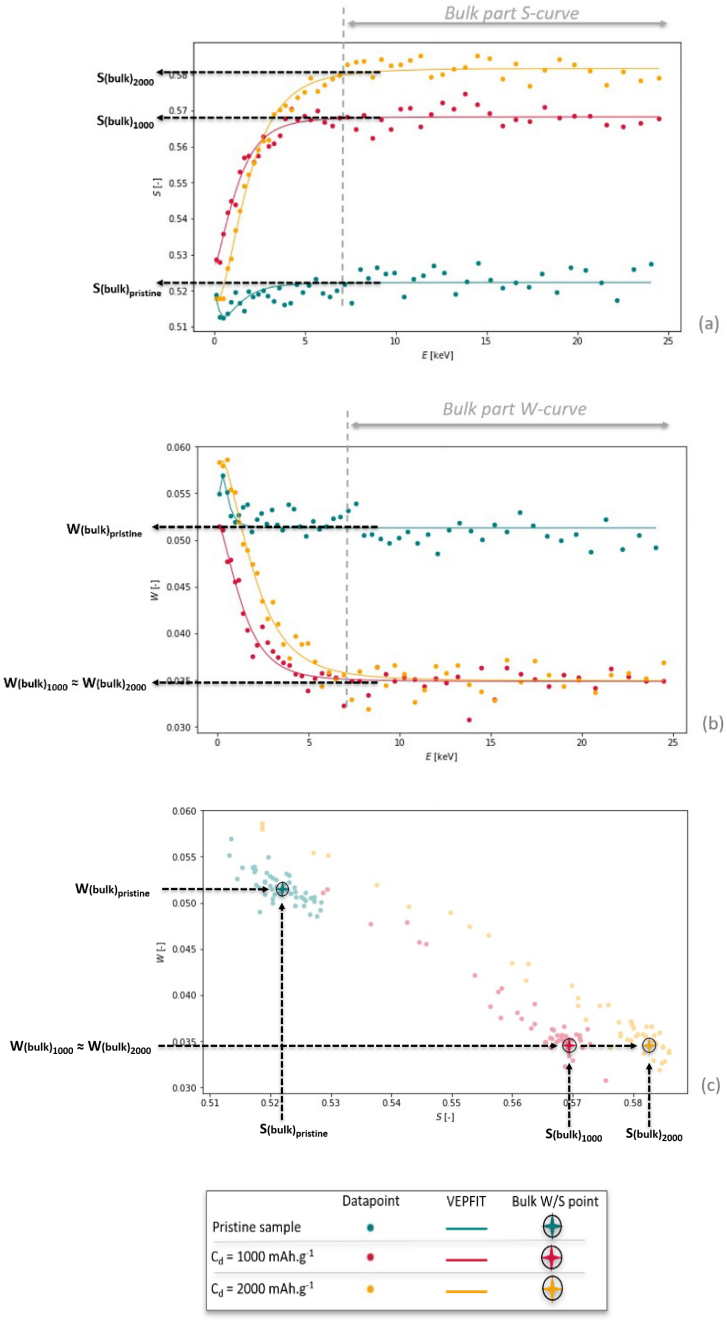


Figure 3.7: Low momentum *S* parameter (a) and high momentum *W* parameter (b) and the *S-W* plot as function of implantation energy (c) for a pristine sample, sample $C_d$=1000 mAh.g$^{-1}$ and sample $C_d$=2000 mAh.g$^{-1}$. An example for determination of the bulk level value is given by the dotted arrows. Bulk *S/W* points are used for further analysis.

The dashed arrows in Figures 3.7[a] and 3.7[b] indicate the bulk value of the defect-sensitive *S* parameter and show significant differences between 1000 mAh.g$^{-1}$ and 2000 mAh.g$^{-1}$, while the *W* parameter for both samples remains approximately the same.



Figure 3.7[c] shows the *S* and *W* parameter in one plot as function of the implantation energy, or equivalently the depth. The characteristic *S,W*-point for the bulk for each of the three samples is indicated by the triangles. These bulk level values are used in this study to observe changes in the damage to the material.

In figure 3.8 all samples (with different discharged capacity $C_d$) are represented by the bulk *S,W*-points. With increasing discharge capacity first an increase in the *S* parameter and a decrease in the *W* parameter is observed. It can be noticed that up to 1000 mAh.g$^{-1}$ the bulk *S,W*-points lie on a single straight line indicating that the concentration of defects has increased without a noticeable change in defect character, which can be related to structural changes (formation of a-Si) due to the lithium alloying process.

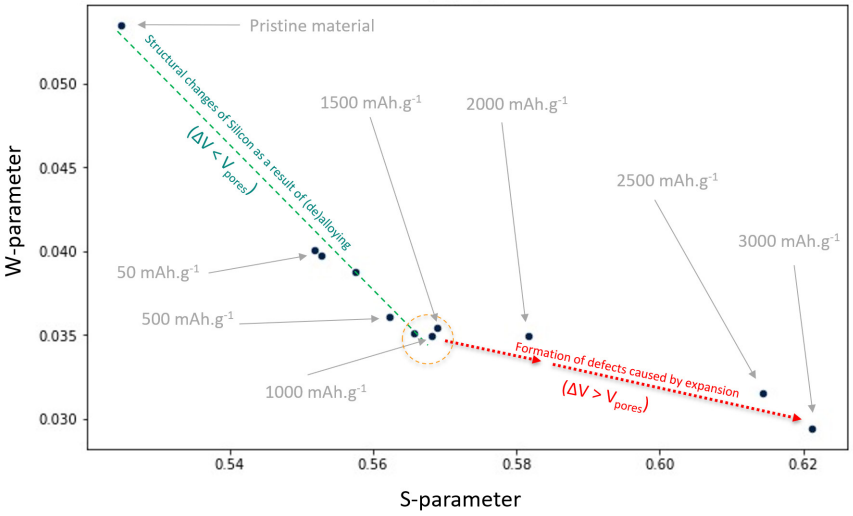


Figure 3.8: *S,W* plane for bulk(*S,W*) values for samples which were cycled against metallic Lithium, discharged to a capacity $C_d$ of respectively 50, 150, 250, 350, 700, 1000, 1500, 2000, 2500 and 3000 mAh.g$^{-1}$) and charged to 1V vs $Li^+$/Li. Each sample is represented by 1 point.

Discharging at 1500 mAh.g$^{-1}$ does not lead to further changes in *S* and *W* meaning that defect concentrations are at a level causing positron saturation trapping. However, for higher discharging levels (2000, 2500 and 3000 mAh.g$^{-1}$) a large increase in mainly the *S* parameter is observed, a clear indication for trapping of positron at a different trapping site. The fact that the change in the *W* parameter is less pronounced hints at the formation of larger (crack precursor) defects.

## Conclusions

The forming of defects in porous Silicon anodes were investigated for different lithiation conditions by using positron annihilation techniques as a highly sensitive defect probe. It appears that the positron-electron momentum distribution changes as soon as a new form of defects occurs, so that the origin of the defects can be accurately determined. The method has shown for porous silicon that during the first two cycles, new or additional defects are formed above a discharge capacity of 1500 mAh.g$^{-1}$. In general, we conclude that positron techniques appears to be a powerful way to investigate the process of defect development in silicon when used as an anode for Li-ion batteries.

In the study we limited ourselves to the lithiation process and the associated development of defects during the first two cycles of porous silicon anodes. The results found lead to a continuation of this study by looking at the defect development that occurs during long-term cycling and investigation of the influence of discharge and charge rate.

# References


An, W., Gao, B., Mei, S., Xiang, B., Fu, J., Wang, L., ... & Huo, K. (2019). Scalable synthesis of ant-nest-like bulk porous silicon for high-performance lithium-ion battery anodes. *Nature communications*, *10*(1), 1-11.

Beaulieu, L. Y., Eberman, K. W., Turner, R. L., Krause, L. J., & Dahn, J. R. (2001). Solid-State Lett. 4. *A137-A140*.

Cho, J. (2010). Porous Si anode materials for lithium rechargeable batteries. *Journal of Materials Chemistry*, *20*(20), 4009-4014.

Chon, M. J., Sethuraman, V. A., McCormick, A., Srinivasan, V., & Guduru, P. R. (2011). Real-time measurement of stress and damage evolution during initial lithiation of crystalline silicon. *Physical review letters*, *107*(4), 045503.

Clement, M., De Nijs, J. M. M., Balk, P., Schut, H., & Van Veen, A. (1996). Analysis of positron beam data by the combined use of the shape-and wing-parameters. *Journal of applied physics*, *79*(12), 9029-9036.

Emagy (2020), consulted on 11/4/2021 by https://e-magy.com/product/. Broek op Langedijk.

Ge, M., Rong, J., Fang, X., Zhang, A., Lu, Y., & Zhou, C. (2013). Scalable preparation of porous silicon nanoparticles and their application for lithium-ion battery anodes. *Nano Research*, *6*(3), 174-181.

Huang, S., Cheong, L. Z., Wang, S., Wang, D., & Shen, C. (2018). In-situ study of surface structure evolution of silicon anodes by electrochemical atomic force microscopy. *Applied Surface Science*, *452*, 67-74

Kalnaus, S., Rhodes, K., & Daniel, C. (2011). A study of lithium ion intercalation induced fracture of silicon particles used as anode material in Li-ion battery. *Journal of Power Sources*, *196*(19), 8116-8124.

Key, B., Morcrette, M., Tarascon, J. M., & Grey, C. P. (2011). Pair distribution function analysis and solid state NMR studies of silicon electrodes for lithium ion batteries: understanding the (de) lithiation mechanisms. *Journal of the American Chemical Society*, *133*(3), 503-512.

Kim, S. H., Kim, Y. S., Baek, W. J., Heo, S., Yun, D. J., Han, S., & Jung, H. (2018). Nanoscale electrical degradation of silicon–carbon composite anode materials for lithium-ion batteries. *ACS applied materials & interfaces*, *10*(29), 24549-24553.

Klinser, G., Kren, H., Koller, S., & Würschum, R. (2019). Operando monitoring of charging-induced defect formation in battery electrodes by positrons. *Applied Physics Letters*, *114*(1), 013905.

Krause-Rehberg, R., & Leipner, H. S. (1999). *Positron annihilation in semiconductors: defect studies* (Vol. 127). Springer Science & Business Media.

Kubota, Y., Escaño, M. C. S., Nakanishi, H., & Kasai, H. (2007). Crystal and electronic structure of Li 15 Si 4. *Journal of Applied Physics*, *102*(5), 053704.

Legerstee, W. J., Boekel, M., Boonstra, S., & Kelder, E. M. (2021). Scanning Probe Microscopy facility for Operando study of redox processes on Lithium Ion Battery electrodes. *Frontiers in Chemistry*, *9*.

Li, J., & Dahn, J. R. (2007). An in situ X-ray diffraction study of the reaction of Li with crystalline Si. *Journal of The Electrochemical Society, 154*(3), A156-A161.

Liu, X. H., & Huang, J. Y. (2011). In situ TEM electrochemistry of anode materials in lithium ion batteries. *Energy & Environmental Science*, *4*(10), 3844-3860.

Lynn, K. G., & Lutz, H. (1980). Slow-positron apparatus for surface studies. *Review of Scientific Instruments*, *51*(7), 977-982.

McDowell, M. T., Ryu, I., Lee, S. W., Wang, C., Nix, W. D., & Cui, Y. (2012). Studying the kinetics of crystalline silicon nanoparticle lithiation with in situ transmission electron microscopy. *Advanced Materials*, *24*(45), 6034-6041.

McDowell, M. T., Lee, S. W., Nix, W. D., & Cui, Y. (2013). 25th anniversary article: understanding the lithiation of silicon and other alloying anodes for lithium-ion batteries. *Advanced Materials*, *25*(36), 4966-4985.

Obrovac, M. N., & Christensen, L. (2004). Structural changes in silicon anodes during lithium insertion/extraction. *Electrochemical and Solid State Letters*, *7*(5), A93.

Ozanam, F., & Rosso, M. (2016). Silicon as anode material for Li-ion batteries. *Materials Science and Engineering: B*, *213*, 2-11.

Rhodes, K., Dudney, N., Lara-Curzio, E., & Daniel, C. (2010). Understanding the degradation of silicon electrodes for lithium-ion batteries using acoustic emission. *Journal of the Electrochemical Society*, *157*(12), A1354.

Salihoglu, O., & Kahlout, Y. E. (2019). Doped silicon nanowires for lithium ion battery anodes. *Materials Research*, *22*(2).

Shen, C., Ge, M., Luo, L., Fang, X., Liu, Y., Zhang, A., ... & Zhou, C. (2016). In situ and ex situ TEM study of lithiation behaviours of porous silicon nanostructures. *Scientific reports*, *6*(1), 1-11.

Shin, H. C., Corno, J. A., Gole, J. L., & Liu, M. (2005). Porous silicon negative electrodes for rechargeable lithium batteries. *Journal of power sources*, *139*(1-2), 314-320.

Smedskjaer, L. C., Manninen, M., & Fluss, M. J. (1980). An alternative interpretation of positron annihilation in dislocations. *Journal of Physics F: Metal Physics*, *10*(10), 2237.

Suzuki, K., Barbiellini, B., Orikasa, Y., Kaprzyk, S., Itou, M., Yamamoto, K., ... & Sakurai, H. (2016). Non-destructive measurement of in-operando lithium concentration in batteries via x-ray Compton scattering. *Journal of Applied Physics*, *119*(2), 025103.

Tang, J., Yin, Q., Wang, Q., Li, Q., Wang, H., Xu, Z., ... & Zhou, L. (2019). Two-dimensional porous silicon nanosheets as anode materials for high performance lithium-ion batteries. *Nanoscale*, *11*(22), 10984-10991.

Tuomisto, F., & Makkonen, I. (2013). Defect identification in semiconductors with positron annihilation: experiment and theory. *Reviews of Modern Physics*, *85*(4), 1583.

Van Veen, A. V., Schut, H., Vries, J. D., Hakvoort, R. A., & Ijpma, M. R. (1991, February). Analysis of positron profiling data by means of "VEPFIT". In *AIP Conference Proceedings* (Vol. 218, No. 1, pp. 171-198). American Institute of Physics.

Vidu, R., Quinlan, F. T., & Stroeve, P. (2002). Use of in situ electrochemical atomic force microscopy (EC-AFM) to monitor cathode surface reaction in organic electrolyte. *Industrial & engineering chemistry research*, *41*(25), 6546-6554.

Wang, J., Huang, W., Kim, Y. S., Jeong, Y. K., Kim, S. C., Heo, J., ... & Cui, Y. (2020). Scalable synthesis of nanoporous silicon microparticles for highly cyclable lithium-ion batteries. *Nano Research*, *13*(6), 1558-1563.

Wang, J., Liao, L., Li, Y., Zhao, J., Shi, F., Yan, K., ... & Cui, Y. (2018). Shell-protective secondary silicon nanostructures as pressure-resistant high-volumetric-capacity anodes for lithium-ion batteries. *Nano letters*, *18*(11), 7060-7065.

Yeom, S. J., Lee, C., Kang, S., Wi, T. U., Lee, C., Chae, S., ... & Lee, H. W. (2019). Native Void Space for Maximum Volumetric Capacity in Silicon-Based Anodes. *Nano letters*, *19*(12), 8793-8800.

Zamfir, M. R., Nguyen, H. T., Moyen, E., Lee, Y. H., & Pribat, D. (2013). Silicon nanowires for Li-based battery anodes: a review. *Journal of Materials Chemistry A*, *1*(34), 9566-9586.

Zhang, W. J. (2011). Lithium insertion/extraction mechanism in alloy anodes for lithium-ion batteries. *Journal of Power Sources*, *196*(3), 877-885.

Zhang, Z., Wang, Y., Ren, W., Tan, Q., Chen, Y., Li, H., ... & Su, F. (2014). Scalable synthesis of interconnected porous silicon/carbon composites by the rochow reaction as high-performance anodes of lithium ion batteries. *Angewandte Chemie*, *126*(20), 5265-5269.

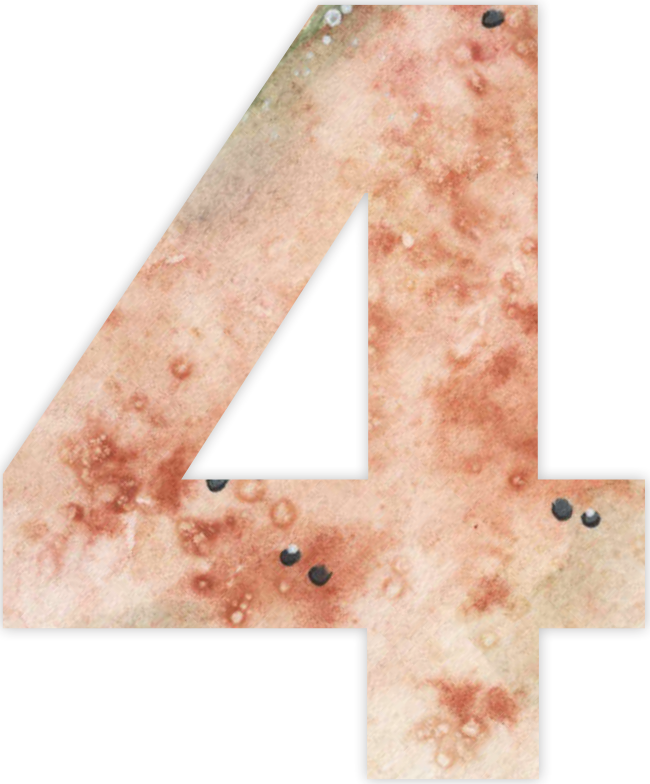

# CHAPTER FOUR

*Analysis of Degradation Processes In Porous Silicon as a result of Lithiation and De-lithiation with Positron Annihilation Spectroscopy*

This chapter has been submitted for publication in parallel with the printing of this thesis.

# Analysis of Degradation Processes In Porous Silicon as a result of Lithiation and De-lithiation with Positron Annihilation Spectroscopy

## Introduction

Silicon as anode material in lithium ion batteries (LIBs) has been subject of many studies in the last decade because of its high theoretical specific capacity, its abundance as raw material on earth, and the environmental benignity [Ramakrishna & Jose 2022]. The capacity of silicon exceeds that of the commonly used anode material graphite nearly by an order of magnitude (3579 $mAh.g^{-1}$ when Si is fully lithiated to amorphous $Li_{15}Si_4$, referred to as a- $Li_{15}Si_4$ ($Li_{3.75}Si$, compared to 372 $mAh.g^{-1}$ for the widely used graphite anode material) [Li&Dahn 2007; Liu & Huang 2011]. But even if silicon can only be used up to a third of its theoretical capacity, it offers a huge capacity improvement over the current generation of Li-ion batteries. The use of anode material with a specific capacity of 1500 $mAh.g^{-1}$ combined with a high capacity cathode material allows for an increase of the specific gravimetric energy density of a full cell battery up to 30% and an increase of the volumetric energy density of ~20% [Plancke et al. 2017; Obrovac & Chevrier 2014]. However, the rapid loss of capacity and degradation caused by the severe volume changes on lithiation and de-lithiation during cycling makes pure and unmodified silicon unsuitable as an anode material. In addition, volume increases of the order of 300% are undesirable for battery electrode materials for various practical reasons (for comparison, graphite anodes have a maximum expansion of about 10% on lithiation). One of the possible solutions to this problem is sought in the use of porous silicon structures [Shin et al 2005; Vu et al 2012] in which a large part of the volume increase can be absorbed by the porosity. To investigate the application of porous silicon, we looked in our previous work at the maximum lithiation possible at which the volume changes are still absorbed by the voids in the material [Legerstee et al 2022]. We introduced Positron annihilation spectroscopy as an ex-situ anode analysis method and examined whether this can be applied as an additional technique for investigating the development of structure defects in silicon (such as the development of undesirable cracks at a very early stage) as a result of the lithiation and de-lithiation process. Our study showed that the origin and development of defects arising in the first two cycles (initial damage) can be accurately investigated using Doppler Broadening Positron Annihilation Spectroscopy (DBPAS) as an analyzing technique. The study showed, for the porous silicon composite anodes we used (Emagy, 2020), the maximum capacity at which no damage occurs is between 1000 and 1200 $mAh.g^{-1}$.

Because the behavior of silicon upon multiple cycling is still poorly understood, more understanding of the material behavior under repeated lithiation/de-lithiation conditions is very important for the use in rechargeable batteries and thus makes further research necessary. Despite the promising results of our previous work concerning the maximum possible capacity without damage, the long term cycling performance and degradation of porous silicon requires a separate study in which multiple processes play a relevant role and DBPAS potentially can make a complementary contribution to the palette of measurement methods. The poor capacity retention and instant and sudden degradation of the material after a relatively low amount of cycles needs more insights into the process behind this, so as to improve material design. In the work presented here we investigate the development of structural changes and the onset of degradation of the material during cycling. Because a combination of processes plays an important role during the cycling of silicon, as well as important changes occur at the electro-chemical, mechanical, structural and morphological level, we make use of a number of complementary measurement techniques and analysis methods. All our electrochemical measurements are performed in half-cell configurations, which means that the silicon containing anodes formally serves as a cathode against metallic lithium. It thus means In this chapter that the term *discharge* represents insertion of lithium ions into silicon, and *charge* represents extraction of lithium from silicon.



## Silicon as an anode material for LIBs

Possible anode materials for Li-ion batteries can be roughly divided into three different types, distinguished by their underlaying charge/discharge processes. The commonly used graphite. lithium titanium oxide ($Li_4Ti_5O_{12}$, LTO) and other layered structured materials belong to *intercalation materials* (i) [Ogumi & Iniba 1998; Delmas et al 1994], where Insertion of Li-ions into the interstitial sites of the crystalline lattice from the host-material takes place. Transition metal compounds belong to the so called *conversion materials* (ii) [Seo et al 2015; Ceder & van der Ven 1999], where the conversion reaction is based on the displacement of a transition metal by Li-ions. The third type of material that can be used as anode in Li-ion batteries, the *lithium alloys* (iii), is based on alloying between the electrode material and lithium [Obrovac et al 2007]. This type of materials have the ability to store much higher amounts of lithium compared to intercalation and conversion materials. Examples of suitable alloy materials for anodes in Li-ion batteries are Ag, Al, Ge, Sb, Sn, Zn, and Si, where the latter is the alloying material with the highest maximum lithiation (3,75 Li per Si). This makes silicon very interesting for researchers as a subject for study and for industry as a promising candidate as anode material. The alloying process of silicon results

in substantial structural changes when compared to transition metal compounds or intercalation electrode materials where lithium is incorporated into lattice sites with limited structural distortions. Because of this extra complexity, additional analyzing methods like the DBPAS technique can provide a valuable insight into these changes.

### Alloying and de-alloying process of silicon with lithium

The electrochemical lithiation process of crystalline Si knows several crystalline $Li_xSi$ phases at temperatures above ~400℃ [Chevrier et al 2010], however, at room temperature, the electrochemical lithiation consists of two phases.

When starting with pristine crystalline silicon the alloy reaction can be written as

$$c - Si + xLi^+ + xe^- \longrightarrow a - Li_xSi \qquad \text{(Eq 4.1)}$$

Resulting in an amorphous phase. where x increases to the reaction is followed by

$$a - Li_xSi + (3{,}75 - x)Li^+ + (3{,}75 - x)e^- \longrightarrow a{-}Li_{3{,}75}Si \qquad \text{(Eq 4.2)}$$

for deep lithiation in the amorphous phase.

When the maximum amorphous lithiation state $Li_{3,75}Si$ is reached, only a very small amount of lithium (δ) is needed for an abrupt formation of meta stable crystalline $Li_{3,75}Si$ nuclei followed by rapid grain growth (Mcdowell et al 2013):

$$aLi_{3,75}Si + \delta Li^+ + \delta e^- \longrightarrow aLi_{3,75+\delta}Si \qquad \text{(Eq 4.3)}$$

$$aLi_{3,75+\delta}Si \longrightarrow cLi_{3,75+\delta}Si + \delta li \qquad \text{(Eq 4.4)}$$

The extra lithium atoms ($\delta Li$) are believed to act as a catalyst which enables the crystallization process (Jiang et al 2020). The formation of crystalline $Li_{3,75}Si$ is generally associated with a drop below a threshold voltage value, ranging from 30 to 70 mV vs. Li+/Li [Obrovac & Christensen 2004; Kang et al 2007; Kubota et al 2007; Laboni & Obrovac 2015; Woodard et al 2021].

When used in a battery, the material needs to be cycled and so, de-lithiation occurs at a given state of the material. If the material has not reached the crystalline phase during lithiation ($x \leq 3{,}75$), the de-lithiation process will proceed as follows:

$$a - Li_xSi \longrightarrow a - Li_\vartheta Si + (x - \vartheta)\, Li^+ + (x - \vartheta)\, e^- \qquad \text{(Eq 4.5)}$$

Where ϑ represents a very small amount of lithium left in the lithium poor $Li_\vartheta Si$ alloy. In a second lithiation step of the lithium poor and amorphous material will proceed following Equation 4.2.

When there is a crystalline phase of $cLi_{3,75}Si$ formed during the lithiation process ($x$=3,75) and de-lithiation takes place, the de-lithiation reaction for the crystalline part can be written as:



$$c - Li_{3,75}Si \xrightarrow{delitiation} aLi_xSi \; + residual\; c - Li_{3,75}Si \qquad \text{(Eq 4.6)}$$

The residual amount of crystalline $c - Li_{3,75}Si$ is partly the result of the volume contraction during de-lithiation which leads to the development of cracks and pulverization generating small isolated lithiated particles that can no longer contribute to the delithiation process due to poor electrical contact with the bulk material and the current collector [Ko et al 2016]. This means that the presence of $c - Li_{3,75}Si$ in delithiated samples can be an indication that isolated particles are present as a result of pulverization.

### Electron conductivity and lithium diffusion

The recombination of lithium ions with electrons to lithium atoms takes place at the interface between the electrode (silicon particle) and the electrolyte. Lithium atoms then diffuse through the lithiated silicon to the reaction front, where they contribute to the alloy reaction to form amorphous $Li_xSi$. In many silicon based composite electrodes, electron conduction is created by adding a good conductor, such as carbon particles or an advanced metal coating. However, this addition provides improved conduction of electrons within the electrode composite, but does not significantly affect conduction at the surface of a silicon particle or deeper in a morphological structure such as porous particles. Conduction of electrons through the particle or along the surface is therefore desirable. When silicon is doped with lithium, it forms an n-type semiconductor, where at room temperature the conductivity increases proportionally with the amount of lithium. However, the doping range for semiconductors (typical $10^{14}$-$10^{19}$ $cm^{-3}$) is immensely lower than the lithium concentration reached in electrochemically alloyed battery electrodes ($10^{23}$ $cm^{-3}$). These lithium concentrations make $Li_xSi$ an electron conductor. A distinction can be made between electron conduction through the particle (bulk conduction) and electron conduction along the surface (surface conduction). The latter

is most important for the required recombination of electrons and *Li* ions inside the pores and channels of a porous silicon structure.

The diffusion of lithium in silicon is an important parameter for the use of silicon in battery anodes, especially for high power applications, because it partly determines how fast a battery can be charged and discharged. Determination of the diffusion coefficient has been performed in many different ways and by many different researchers (for a comprehensive overview see [Ozanam et al 2016]). Depending on the determination method used, the lithiation state and other influential material and electrochemical parameters, there are large differences in the values found (roughly between $10^{-14}$ and $10^{-10}$ $cm^2s^{-1}$). In general it can be said that the diffusion increases as x in $Li_xSi$ increases [Xie et al 2010; Ding et al 2009], and also as the number of cycles increases [Zhang et al 2008]. In addition, the formation of cracks as a result of the large volume changes creates faster pathways along the fracture surfaces for lithium to diffuse [McDowell et al 2012].



During lithiation, the alloying process between silicon and lithium forms a distinct reaction front with an atomically sharp phase boundary of a few nanometers [Chon et al 2011]. The ratio between the diffusivity of lithium in $Li_xSi$ and the rate of the alloying reaction is indicative of which process is dominant, and thus determines the rate with which the silicon is lithiated. Generally, a thickness of about 8 μm of of $Li_xSi$ was calculated as the thickness at which the rate of lithiation is determined by the reaction rate at the front [Zhao et al 2011], meaning that for most applications with typical silicon particle sizes of a few microns, the lithiation is not limited by the diffusion of lithium through the amorphous $Li_xSi$ phase. In fact, the reaction rate is mainly limited by short range processes at the reaction front [Liu et al 2011]. When the silicon is partially alloyed with lithium (only a fraction of the maximum theoretical capacity is used), then next to the lithiated $Li_xSi$ shell a *c-Si* core will co-exist, separated by a sharp boundary due to the single phase nanometer reaction front. In some studies and explanations this is used as a crystalline silicon backbone concerning shapes like pillars or porous particles to facilitate proper battery performance (Figure 4.3c and 4.3d) [Obrovac and Krause 2006].

### Effects of mechanical properties

Lithiation of silicon leads to important changes in mechanical properties. Several studies show that the Youngs modulus and hardness of lithiated silicon decrease with increasing lithium content, and that under certain conditions creep occurs via

viscoplastic flow [Berla et al 2015; Shenoy et al 2010]. Pristine crystalline silicon is a brittle material, but as a result of lithiation it becomes ductile and obtains inelastic deformation properties. The high mechanical stresses that occur during the reaction with lithium ensure that plastic deformation takes place simultaneously to accommodate the large volumetric expansion. Due to the sharp boundary at the alloying reaction front, brittle fracture can occur in the pristine silicon near the boundary [Wang, X et al 2015]. In addition, the way in which the reaction front of the lithiation process forms is in many cases determined by the morphological structure of the silicon and influences the degree and manner of deformation that the silicon undergoes during lithiation. Zhao et al (2013) compared the development of stress at a flat reaction front, which occurs in thin layers of silicon (made by deposition techniques such as sputtering [Maranchi et al 2003], with a curved reaction front that occurs in spherical particles [Ma et al 2013] and pillar structures [Lee et al 2011]. In figure 4.1 we added to this comparison the development of stress and deformation for hollow structures such as pores or channels. Figure 4.1a shows the development of a straight reaction front without curvature, in which a compressive stress occurs in the biaxial plane parallel to the reaction front both at the interface and in the lithiated material. Figure 4.1b shows a curved reaction front with silicon core and a lithiated $Li_xSi$ shell. The reaction front undergoes compressive stress in the radial and tangential directions while the volume increase of the lithiated shell creates tensile hoop stress on the surface (that can lead to fracture on the surface). Figure 4.1c shows the situation for a lithiation process with a curved reaction front in which the supply of lithium takes place from the inner wall of a cylinder. A cylindrical boundary layer is created between pristine silicon and the $Li_xSi$ alloy, wherein during the lithiation process, the internal hollow pore is filled by the expanding $Li_xSi$, as shown in figure 4.1d, where the development of pore filling is illustrated. This immediately makes clear that the lithiated silicon needs to deform to accommodate the large volumetric expansion associated with the alloying process. At the reaction front the process occurs by the alloying of silicon with lithium to $Li_xSi$, directly resulting in concurrent volume expansion. During this process, an element of lithiated silicon at the curved reaction front first undergoes compressive plastic deformation in the hoop directions, after which the element is pushed towards the center of the cylinder, unloads elastically and deforms plastically again under the compressive stress. This combination of the alloying expansion reaction and plastic flow is repeated continuously during the lithiation process causing the pores in the porous silicon to shrink until the entire pore volume is consumed. The material deformations that occur during the lithiation process cause the pores to

be squeezed by compression and thereby the cylindrical shape will be affected and assumes an arbitrary deformation shape. From this it can be concluded that during delithiation, the pore will not revert to its original cylindrical shape. According to the findings of Pharr et al. (2014), plastic deformation takes place as a result of lithiation of silicon. Pores in the material could accelerate this process.

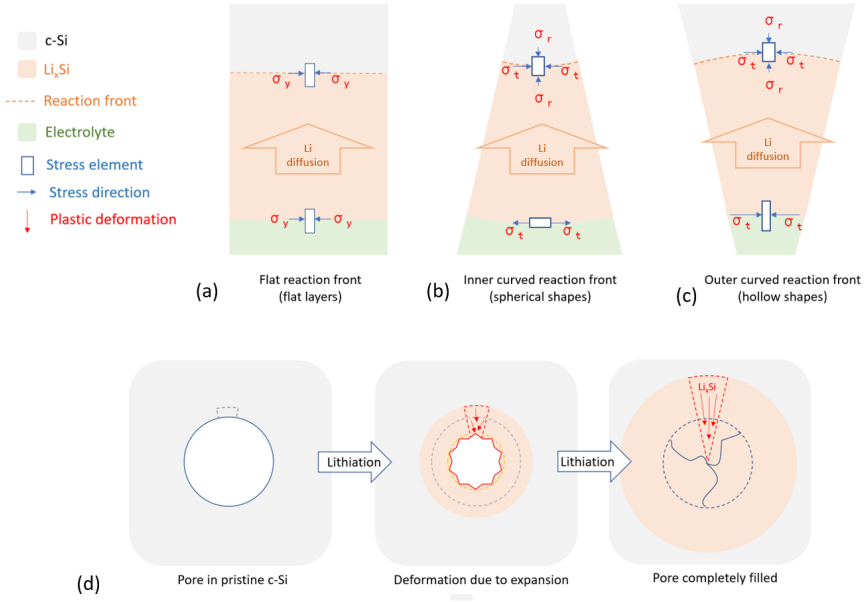


Figure 4.1: Development of the reaction front during lithiation for (a) a flat shape, (b) a inner curved shape, and (c) an outer curved shape; (d) the deformation of a pore during lithiation caused by volume expansion.

## Positron Annihilation Doppler Broadening Spectroscopy

Positron annihilation techniques in general [Krause-Rehberg & Leipner 1999] are used for almost 5 decades as a high sensitive probe technique for investigating voids and open volumes in condensed matter by probing the electron density distribution in the material [Schultz & Lynn 1988]. By implanting positrons with selected energies (proportional to implantation depth) into a solid, they lose energy during diffusion until annihilation with an electron takes place, after which (generally) two 511 keV gamma's are emitted in opposite directions. The momentum component of the positron-electron pair during annihilation broadens the energy distribution of the

annihilation gamma's. This so called Doppler shift contains information about the electron momentum distribution at the annihilation site. The energy distribution around 511 keV is characterized by two parameters, (i) *the shape parameter S*, which represents the gammas with a relatively small deviation of 511 keV, often caused by annihilations with free and valence electrons, and (ii) *the wing parameter W*, which represents events that have a larger deviation of 511 keV and are caused by annihilations with high-momentum core electrons. This makes the *S* parameter sensitive to defect concentrations in the investigated material, whereas the *W* parameter gives information about defect atomic surroundings. For the present study, in which we focus on the development of defects as a result of the repetitive lithiation and delithiation of silicon, we limit ourselves to analyzing the development of the *S* parameter as a result of cycling.



Although our previous study (chapter 3) showed that the combination of the *S* and *W* parameter can provide valuable insights, due to its higher complexity we first focus on analyses of only the defect-sensitive *S* parameter for the current study.

Positron interaction with solid materials is a complex process which comprise backscattering, channeling, thermalization, diffusion, interaction with surfaces and possible trapping in defects. The latter is sensitive for a wide range of defects like vacancies, dislocations, voids, precipitates, interfaces and grain boundaries. Because silicon as an anode material is subject to large volume changes causing defects followed by capacity loss, positron annihilation techniques may contribute to the understanding of the underlying processes. The present work is a follow up of our previous study, where we introduced Positron Annihilation Spectroscopy (PAS) as a nondestructive technique for determination of the maximum lithiation rate in prepared porous silicon anodes at which no damage occurs [Legerstee et al 2022].

The Doppler shift in the energy of the 511 keV annihilation gammas emitted when a positron annihilates was measured using the Delft Variable Energy Positron beam (VEP), a mono-energetic, magnetically guided positron beam ($10^5$ positrons.$s^{-1}$) at user variable energy ranging from 1 to 25 keV, for depth selective probing of defects and interfaces (depth range typically from 0-2 μm). The measurements were analyzed using the modelling and fitting algorithm VEPFIT [Van Veen et al 1991]. From the results, the bulk value of the *S* parameter was then obtained, as shown in Figure 4.2.

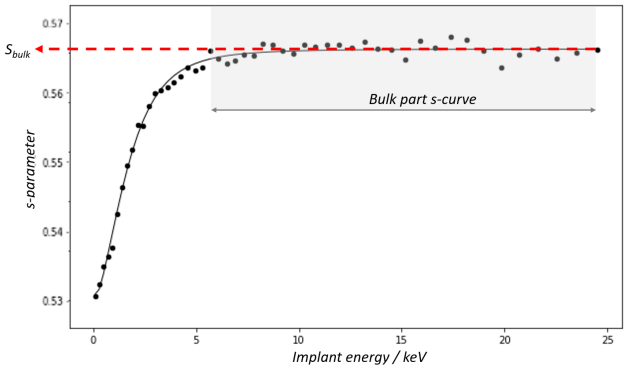


Figure 4.2: Example of a S-parameter depth profile from a lithiated silicon sample. For our analysis we used the bulk value (red dot line) for comparison between different samples.

## Experimental methods and work procedures

### Electrochemical cycling of porous silicon samples

For comparison and complementation of the results, silicon rich anodes were produced from the same porous material as used in our previous study [Legerstee at al 2022]. The base material [Emagy] consists of crystalline silicon particles with a size distribution of 2-6 micron. The particles contain pores that are circular or elliptical in shape and have a pore size distribution with sizes of 200-400 nm (see Figure 4.3a and b). Electrodes where prepared on a copper foil current collector using the doctor blade casting method by mixing 80% porous Silicon particles with 10% Carbon Black in a buffered critic acid solution of 10% Polyacrylic Acid (PAA) to make a slurry. The prepared electrodes where dried in a vacuum oven at 60 °C for 12 h, and cut into discs of 12,7 mm diameter. The prepared electrodes were then placed in a glovebox and accurately weighed to determine the amount of silicon in a sample. The samples were assembled in a demountable lab cell (airtight mounted stainless steel poles separated by a PTFE gasket) into a half-cell configuration with lithium foil as counter and reference electrode. The electrodes where separated by a glass fiber membrane on the lithium metal side and polypropylene membrane (Cellgard 2400) on the silicon side, soaked with 1M solution of $LiPF_6$ in 1:1 (vol.%) ethylene carbonate (EC):dimethyl carbonate (DMC) as electrolyte. The samples were cycled (repeatedly lithiated/discharged and de-lithiated/charged) with C-rates based on 1C=1000 $mAh.g^{-1}$, that is the capacity at which the porous material has been extensively tested by the manufacturer (Emagy).

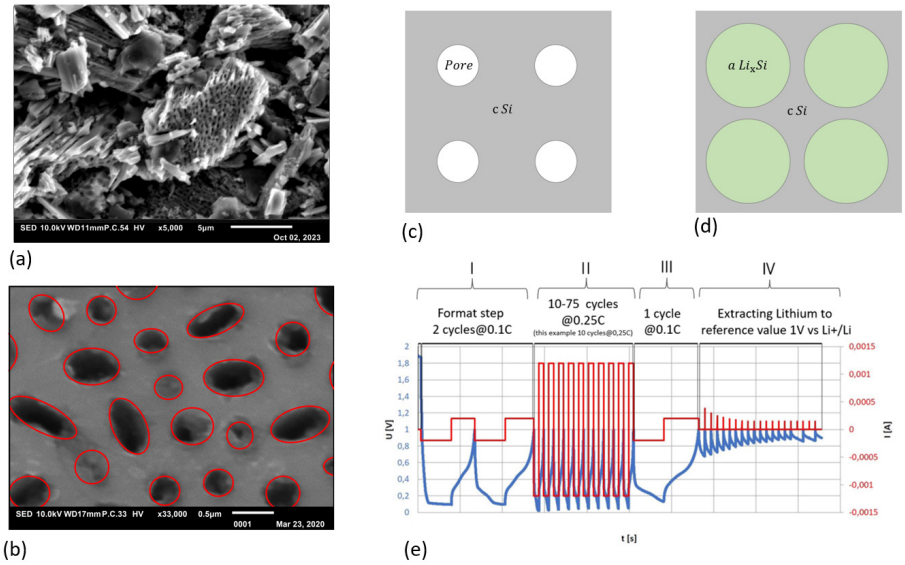


Figure 4.3: (a) SEM picture of porous silicon particle; (b) SEM picture of porous silicon flake surface; (c) schematic representation of pores in a crystalline silicon matrix; (d) partially lithiated silicon whereby the pores are completely filled with amorphous $Li_xSi$ and a crystalline matrix remains; (e) Charge/discharge procedure.

Electrochemical tests were carried out using a Maccor™ battery tester, and conducted under constant current conditions (galvanostatic) with a lower voltage limit of 0.05 V for preventing the formation of the unwanted crystalline $Li_{15}Si_4$ phase. The upper limit was set at 1 V for delithiation. Before the main cycling tests starts, all samples were cycled twice at a current of 0.1C and a discharge capacity ($C_d$) of 1000 mAh.g$^{-1}$, the so called 'formation procedure'. The main cycling tests (5, 10, 15, 20, 30, 35, 39, 42 and 76 cycles) where performed with values for $C_d$ of 1000, 1200 and 1500 mAh.g$^{-1}$ and a C-rate of 0,25C (based on 1C=1000 mAh.g$^{-1}$), followed by a final delithiation procedure. In figure 4.3e an example of the cycling procedure is given. Here the first part (Part I) is the format procedure, followed by Part II, the cycling step. The last part, the final delithiation step consists of two parts. Part III consists of 1 cycle at 0,1C followed by Part IV where the sample is repeatedly charged (delithiated) under a constant voltage of 1V against $Li^+$/Li to extract as much as possible lithium from the sample.

After the discharge/charge procedures the samples were prepared for analysis. The cells were dismounted in an airtight glovebox filled with argon (<1 ppm oxygen and moisture) and the anode samples were carefully removed from the separator, after

which they were rinsed in Dimethyl Carbonate for 10 minutes under stirring conditions. The samples were then dried under vacuum for 20 minutes and placed in an airtight sample holder for X-ray diffraction measurements (Bruker D8 Advance diffractometer with a Cu-Kα radiation source). After the measurement, the airtight sample holder was returned to the glovebox after which the samples were transferred to a special sample holder for DBPAS measurements. The sample holder was transported to the DBPAS facility in an air-tight box. The positron setup was flushed with $N_2$ during the placement of the samples, and samples were transferred to the set-up within one second, so that minimal contamination with air has occurred. The DBPAS setup was brought to a vacuum level of $1.10^{-6}$ mbar after which the positron measurements for 48 different implantation energies have started. After the completion of the DBPAS measurements, the samples were carefully removed from the holder after which surface analysis was performed by Scanning Electron Microscopy (SEM) (JEOL JSM-IT100).

## Data analysis

In materials science, XRD is probably the most widely used tool to determine structural changes of materials, and has therefore often been used to investigate the changes of silicon as a result of lithiation, both in-situ, ex-situ and operando [Hatchard and Dahn 2004; Misra et al 2012]. For the study described here, this technique is used to monitor the amorphization process and the possible development of *crystalline LiSi* compounds as a result of cycling. To quantify the degree of amorphization, the *full with at half maximum* (FWHM) values of the three dominant peaks of crystalline silicon were added together and then normalized to the value of the pristine sample, which is in a fully crystalline state.

Data of the positron measurements were analyzed by VEPFIT to determine the bulk values of the *S* parameter. For more information we refer to our previous work [Legerstee at al. 2022].

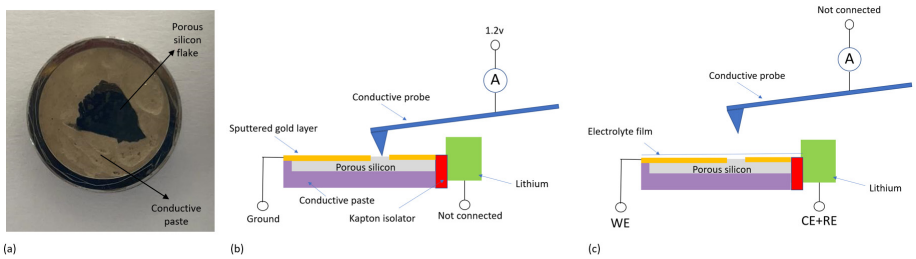


Figure 4.4: Sample preparation for use of a flake for conductive AFM measurements (a); schematic representation of conductivity measurement (b); probe lifted and surface wetted with electrolyte film for lithiation process (c)

### Atomic Force Microscopy on porous wafer samples

We used an Atomic Force Microscope (AFM) (Ntegra NT-NDT) for analyzing the conductivity of the surface of the porous silicon by so called *Spreading Resistance AFM*. This instrument is situated in a customized airtight glovebox under inert atmosphere [Legerstee et al. 2021] to allow for direct and open scanning probe measurements on lithiated silicon surfaces. Scans where performed using a diamond coated conductive AFM probe (Nanosensors CDT-NCHR, Nominal resonance frequency 400 kHz, Nominal force constant 80 N/m).



Besides the 2-6 micron sized particles that we used for preparing anode foils, we obtained Porous c-Si from Emagy™ in the form of so called 'flakes' which is a half product in the production process and, due to its flat shape and pore orientation (perpendicular to the surface), is very suitable as a sample for surface analyses by AFM. Figure 4.4a shows how a flake was positioned inside a stainless steel can that was filled with a conductive paste (MG-Chemicals 8331D). After drying (24 h), the surface was sanded down to a flake thickness of ~500 µm, after which the surface was further smoothed using a polishing set (diamond paste 1 µm, Dieter Schmid fine tools). A piece of adhesive tape (Kapton, Thickness 0,1 mm) was applied to the surface after which a line shaped sputter mask (line width ~0,5 mm) was cut (in the adhesive tape sticked to the surface) by a laser engraver (Trotec SP200). The masked sample was placed into a magnetron sputtering setup (Lith SD900c) directly below and in the center of the target, after which a smooth gold layer (thickness ~50 nm) was sputtered on the uncovered parts of the sample. The mask (adhesive tape) was then removed, leaving a conductive gold mesh on the silicon surface. The sample was brought into the glovebox for analyzing by AFM. First, a topographic scan was made by the AFM in semi contact mode (tapping mode). The AFM was then switched to contact mode to obtain a spreading resistance scan of the same surface by applying a potential of 1,2 V between tip and sample. An electrolyte ($LiPF_6$) film has been applied to the surface (for procedure see Legerstee at al 2021). The electrolyte was in contact both with the silicon and the metallic lithium and lithiation was started by applying a bias voltage of 0.1 V for 15 minutes using the potentiostat/galvanostat (Metrohm Autolab PG-STAT302F). After this, the electrolyte was carefully removed from the surface, after which a conductive scan was made using the AFM. This lithiation/scanning procedure was repeated once more.

## Results and discussion

### Amorphisation and defect analysis

We have made long term cycling measurements for samples with a limited discharge capacity (lithiation) of 1000, 1200 and 1500 mAh.g$^{-1}$ which corresponds respectively to 28%, 33,5% and 42% of the total theoretical capacity of silicon (3579 mAh.g$^{-1}$ which is the maximum for the highest electrochemacally lithiated phase of $Li_{3,75}Si$). In fact, every discharge cycle we terminate the lithiation process when the specific capacity has reached, to jump to the following delithiation step of the cycling process. This causes the silicon particles to be partially lithiated, meaning that the particle consists of a crystalline core with a lithiated phase around it (Obrovac and Krause 2006). It can be assumed that the amount of amorphous silicon for each of the applied discharge capacities (1000, 1200 and 1500 mAh.g$^{-1}$, respectively), at least after the first cycle, will be proportional to the above-mentioned percentages of the theoretical capacity (28%, 33,5% and 42%), so in every case a significant amount of crystalline silicon remains in the particles. To determine the crystalline fraction of silicon from the XRD results of the cycled anode samples, the sum of the three main Si peaks (111), (220), and (311) was taken and normalized to the value of the pristine Si samples.

In Figure 4.5 both the bulk value of the positron annihilation S parameter (Fig. 4.5b) and the normalized value of the silicon peaks from the XRD results (Fig. 4.5a) are shown as a function of the number of charge-discharge cycles. The table in Figure 4.5c also provides an overview of all these values, including the coulombic efficiency (CE) of the last cycle of each measurement.

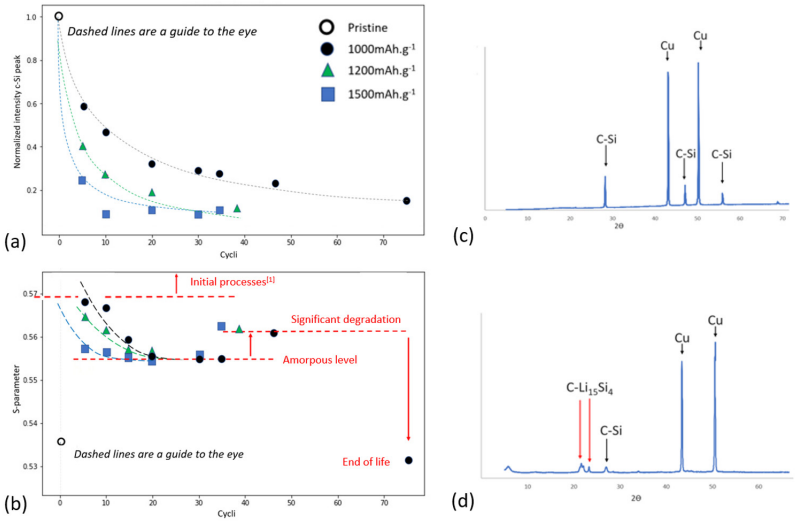


| Cycli | 1000 mAh.g$^{-1}$ | | | 1200 mAh.g$^{-1}$ | | | 1500 mAh.g$^{-1}$ | | |
|---|---|---|---|---|---|---|---|---|---|
| | S-parameter Bulk | Normalized Si peak | CE @last cycle | S-parameter Bulk | Normalized Si peak | CE @last cycle | S-parameter Bulk | Normalized Si peak | CE @last cycle |
| **Pristine** | 0.536 | 1 | -- | 0.536 | 1 | -- | 0.536 | 1 | -- |
| **5** | 0.569 | 0.59 | -- | 0.565 | 0.41 | -- | 0.557 | 0.24 | -- |
| **10** | 0.568 | 0.46 | -- | 0.562 | 0.27 | -- | 0.556 | 0.10 | -- |
| **15** | 0.559 | -- | 98,7 | 0.558 | -- | 98.3 | 0.556 | -- | 98.3 |
| **20** | 0.556 | 0.32 | 99.1 | 0.557 | 0.19 | 98.5 | 0.555 | 0.11 | 98.1 |
| **30** | 0.555 | 0.30 | 98.8 | -- | -- | -- | 0.556 | 0.09 | 97.8 |
| **35** | 0.555 | 0.29 | 98.9 | -- | -- | -- | 0.563 | 0.10 | 95.3 |
| **39** | -- | -- | -- | 0.562 | 0.12 | 92.1 | -- | -- | -- |
| **47** | 0.561 | 0.24 | 96.0 | -- | -- | -- | -- | -- | -- |
| **76** | 0.532 | 0.16 | EOL | -- | -- | -- | -- | -- | -- |

(e)

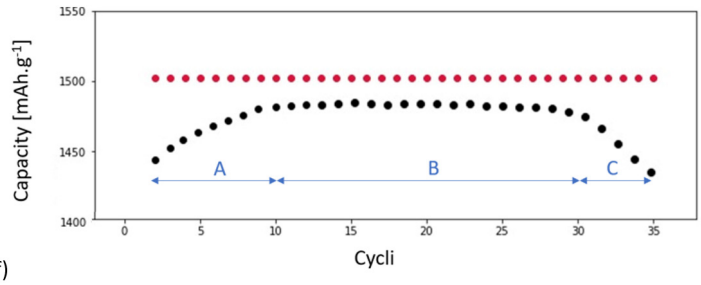


Figure 4.5: (a) normalized intensity of three c-Si XRD peaks (2θ 28.48/47.30/56.08)of figure c; (b) bulk value of the S parameter for cycled samples for 1000, 1200 and 1500 mAh.g$^{-1}$ charge capacities. Initial processes [1] are described in detail in Legerstee et al. (2022); (c) example of XRD measurements for pristine sample and (d) 76 cycles containing the crystalline $Li_{15}Si_4$ phase; (e) table of determined values for all samples; (f) example of coulombic efficiency (sample 35 cycli@1500mAh.g$^{-1}$ ) which shows the difference between charge capacity (red dots) and discharge capacity (black dots). First 7 cycles (Part A) the CE is rising and then stabilizes (Part B) after which the charge capacity remains the same while the discharge capacity drops down (part c).

Figure 4.5a shows the normalized Si peaks ( mean of 2θ 28.48/47.30/56.08, normalized on the pristine value) obtained from the XRD results that were taken right after the positron measurements. A clear trend is visible whereby the amorphization increases (intensity of the normalized silicon peaks decreases) with the number of cycles. This indicates that the amorphization has a progressive character whereby the crystalline silicon core (backbone) of the particles is consumed during cycling. It can be seen that the measurements with a loading capacity of 1000 mAh.g$^{-1}$ (black dots) undergo a relatively slow amorphization process compared to the 1200 mAh.g$^{-1}$ (green triangles) and 1500 mAh.g$^{-1}$ (blue squares). Moreover, the difference between 1000 mAh.g$^{-1}$ and 1200 mAh.g$^{-1}$ is more pronounced than between 1200 mAh.g$^{-1}$ and 1500 mAh.g$^{-1}$. The cause of this may be related to larger amounts of material expanding around the pores, resulting in higher stresses and plastic deformation occurring, as shown in Figure 4.1d.

Figure 4.5b shows the DBPAS defect sensitive *S* parameter as a function of completed charge/discharge cycles. All values for end (discharge) capacities of 1000 (black dots), 1200 (green triangles), and 1500 mAh.g$^{-1}$ (blue squares) are given. The top left corner of the figure shows where the much higher *S*-values of the initial processes (previous study) are located. For the first 20 cycles it can be seen that, as the number of cycles increases, the *S*-value decreases to an plateau in the graph around S=0.555. The way in which the *S* parameter evolves to this plateau is different for 1000, 1200 and 1500 mAh.g$^{-1}$, but appears to proceed in the same way as the normalized intensity of the Si peaks from Figure 4.5a. Furthermore, the higher value of the *S* parameter for the first cycles compared to the pristine sample indicates an increase in the number of defects as a result of cycling. The amorphization process is then accompanied by a decrease in the *S*-parameter during the first 15-20 cycles, which indicates a densification of the material.

The plateau (indicated as 'amorphous level' in figure 4.5b) seems to indicate a stabilization of the *S*-parameter when most of the material is amorphized (see figure 4.5a). Furthermore, it is noticeable that after 20-30 cycles the *S* parameter has a value about 3.5% higher than that of the pristine sample, which is consistent with the change of the *S* parameter in comparable processes from literature [Melskens et al 2014; Melskens et al 2017].

When the coulombic efficiency of a sample deviated significantly (as shown in Figure 4.5f for sample 35 cycli@1500 mAh.g$^{-1}$), the cyclic measurements were stopped abruptly, the following delithiation step was started (Figure 4.3e III and IV) and after which a DBPAS measurement was performed. These samples give a significantly increased *S*-value around *S*=0,562 as can be seen in the figure (red dotted line).

One sample was cycled until the end of life was reached: the last cycles of the electrochemical measurement (the procedure of part II in Figure 4.3e) of this sample show an increasing difference between lithiation and delithiation capacity (coulombic efficiency becomes very low) and ends in a situation where almost no more lithium is extracted from the sample during the delithiation step. For this sample the *S*-value appeared to have decreased enormously to a value around 0.530.



In summary, it can be said that the silicon anode material in the pristine and crystalline situation has a low *S*-value because it contains a relatively small amount of defects. As soon as the electrochemical lithiation and delithiation (cycling) is started, the *S* parameter increases to a relatively high value. During the first 10 to 15 cycles the *S* parameter decreases towards a plateau where it appears to be stabilized. This trend coincides with the trend of the normalized silicon peak from the XRD results. The *S* parameter is constant for some time after complete amorphization and still has a higher value than for the pristine silicon sample. This can be explained by the fact that the amorphous structure has a higher degree of disorder than the crystalline structure of the pristine sample. If a deterioration in the coulombic efficiency is observed in the cycle measurements, this is accompanied by an increase in the *S* parameter. At the end of life, where virtually no delithiation takes place, we see the *S* parameter to drop drastically. The larger amount of lithium in the sample may result in fewer defects in the material.

Finally, as an example, in Figure 4.5 two XRD spectra are shown; in Figure 4.5c the pristine sample with the fully crystalline Si particles, and in Figure 4.5d the 'end of life' sample with 76 cycles, which is the only sample to show a small peak of the metastable $Li_{15}Si_4$ phase.

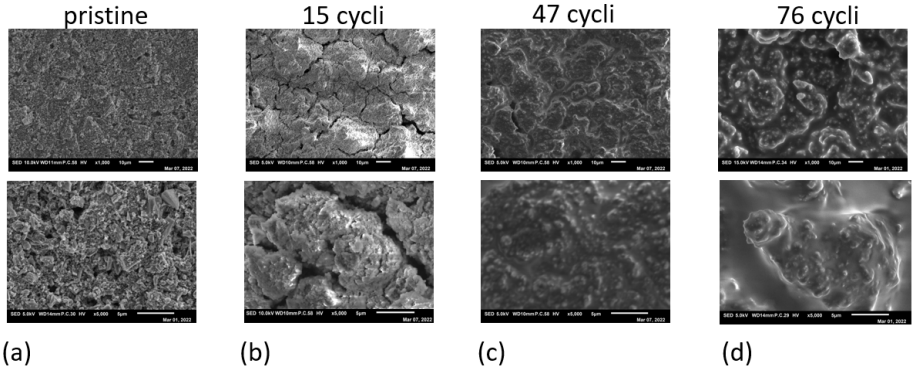


Figure 4.6: SEM pictures of the Si-anodes with magnification 1000 (above) and 2500 (below); (a) pristine; (b) after 15 cycles; (c) after 47 cycles; (d) after 76 cycles.

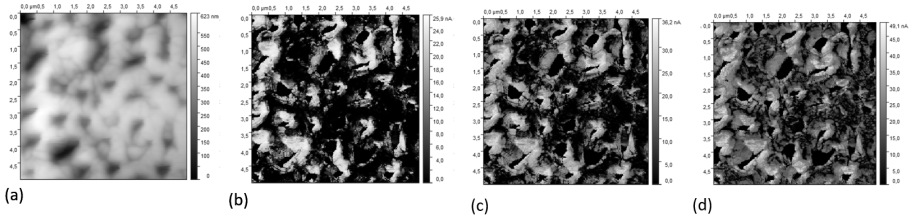


Figure 4.7: AFM images of the surface of porous silicon; (a) topographical image of the porous silicon sample surface made in tapping mode; (b) conductivity of the surface when the sample is not lithiated (pristine state); (c) conductivity of the sample after first lithiation of 15 minutes; (d) conductivity of the surface after second lithiation of again 15 minutes.

## Surface analysis of cycled samples

After the positron measurements the samples were exposed to air. We finally analyzed the anode surface using SEM. Figure 4.6 shows surface morphologies measured with SEM at two magnifications (1000x and 2500x) of 4 samples (all cycled with a c rate of 0.25 and a discharge capacity of 1000 $mAhg^{-1}$ in the voltage range between 1 v and 0.02 v) in which clear differences are visible. The images in Figure 4.6a show the pristine material, where we see a fairly flat surface with the angular and sharp edges of the particles clearly visible. After 15 cycles (Figure 4.6b), the distorted and bulged surface shows coarse cracks in the anode layer, between which the individual particles with their sharp edges are still visible. After 47 cycles (Figure 4.6c) the cracks have disappeared and the surface appears smooth and merged, and after 76 cycles (Figure 4.6d), at the end of life of the sample, bulges emerge from the surface. Overall, the progression from Figure 4.6a to 4.6d clearly shows the evolution of the anode surface as a result of cyclic lithiation and delithiation.

## Surface analysis of porous silicon during lithiation by AFM

As shown schematically in figure 4.7, the conductivity for electrons of the porous silicon was investigated using Spreading Resistance AFM. Figure 4.7a shows a topographical surface scan, where the pores are clearly visible. Figures 4.7b, 4.7c and 4.7d show the conductivity before lithiation, the conductivity after 15 minutes of lithiation, and the conductivity after 30 minutes of lithiation, respectively. Although the exact lithiation rate is not known, this measurement can be used to qualitatively assess the influence of silicon lithiation on conductivity.

The development of conductivity for electrons is clearly visible. While in the pristine material the conductivity is relatively high around the pores compared to the rest

of the surface, the conductivity increases as a result of lithiation, so that after 30 minutes almost the entire surface shows better conductivity.

## Conclusions

We found that crystalline silicon slowly becomes amorphous through lithiation. The results presented here show that the amorphization of the silicon continues and the so-called 'backbone' decreases until the material has an almost completely amorphous structure. Both the silicon normalized XRD peaks and the positron *S*-parameter show a faster decrease as the end (discharge) capacity increases from 1000 to 1200 and finally to 1500 $mAhg^{-1}$. This has been related to the higher mechanical stresses around the pores caused by deformation of the material due to the extreme expansion. The pores deform more when more lithium is added (higher end capacity), resulting in higher stresses, which lead to plastic deformation. To confirm this, AFM hardness measurements could be used, a technique that allows targeted measurements to be made at various locations on the surface, so that the hardness can be determined both close to and between the pores.



It has been shown here that there is a relationship between the positron annihilation *S* parameter and the amorphization process of periodically lithiated and delithiated silicon (cycling). The positron annihilation technique in fact measures the distribution of electron momentum at the annihilation site as a direct quantity and in principle allows a direct relationship to be determined with the type of defect. However, the relationship with the various underlying processes, such as the increase of lithium during cycling, is not yet well understood. Additional measurement techniques are needed to further investigate this.

At the end of life, the sudden reduction in the S-value appears to be related to the residual lithium. The presence of the $Li_{15}Si_4$ phase provides an additional indication that lithium remains in the sample.

Conductive AFM measurements show that the electron conductivity around the pores is highest, and as the lithiation increases, for the entire surface conductivity also increases. Electrons can therefore reach deep into the pores, allowing lithiation to take place directly within the pores.

# References


Berla, L. A., Lee, S. W., Cui, Y., & Nix, W. D. (2015). Mechanical behavior of electrochemically lithiated silicon. *Journal of Power Sources*, *273*, 41-51.

Ceder, G., & Van der Ven, A. (1999). Phase diagrams of lithium transition metal oxides: investigations from first principles. *Electrochimica Acta*, *45*(1-2), 131-150.

Chevrier, V. L., Zwanziger, J. W., & Dahn, J. R. (2010). First principles study of Li–Si crystalline phases: charge transfer, electronic structure, and lattice vibrations. *Journal of Alloys and Compounds*, *496*(1-2), 25-36.

Chon, M. J., Sethuraman, V. A., McCormick, A., Srinivasan, V., & Guduru, P. R. (2011). Real-time measurement of stress and damage evolution during initial lithiation of crystalline silicon. *Physical review letters*, *107*(4), 045503.

Delmas, C., Cognac-Auradou, H., Cocciantelli, J. M., Ménétrier, M., & Doumerc, J. P. (1994). The LixV2O5 system: An overview of the structure modifications induced by the lithium intercalation. *Solid State Ionics*, *69*(3-4), 257-264.

Ding, N., Xu, J., Yao, Y. X., Wegner, G., Fang, X., Chen, C. H., & Lieberwirth, I. (2009). Determination of the diffusion coefficient of lithium ions in nano-Si. *Solid State Ionics*, *180*(2-3), 222-225.

Drozdov, A. D. (2014). Viscoplastic response of electrode particles in Li-ion batteries driven by insertion of lithium. *International Journal of Solids and Structures*, *51*(3-4), 690-705.

Emagy (2020), consulted on 14/4/2021 by https://e-magy.com/product/, Broek op Langedijk

Gao, Y. F., Cho, M., & Zhou, M. (2013). Mechanical reliability of alloy-based electrode materials for rechargeable Li-ion batteries. *Journal of Mechanical Science and Technology*, *27*(5), 1205-1224.

Hatchard, T. D., & Dahn, J. R. (2004). In situ XRD and electrochemical study of the reaction of lithium with amorphous silicon. *Journal of The Electrochemical Society*, *151*(6), A838.

Jiang, Y., Offer, G., Jiang, J., Marinescu, M., & Wang, H. (2020). Voltage hysteresis model for silicon electrodes for lithium ion batteries, including multi-step phase transformations, crystallization and amorphization. *Journal of The Electrochemical Society*, *167*(13), 130533.

Kang, Y. M., Lee, S. M., Kim, S. J., Jeong, G. J., Sung, M. S., Choi, W. U., & Kim, S. S. (2007). Phase transitions explanatory of the electrochemical degradation mechanism of Si based materials. *Electrochemistry communications*, *9*(5), 959-964.

Ko, Y., Hwang, C., & Song, H. K. (2016). Investigation on silicon alloying kinetics during lithiation by galvanostatic impedance spectroscopy. *Journal of Power Sources*, *315*, 145-151.

Konishi, H., Hirano, T., Takamatsu, D., Gunji, A., Feng, X., & Furutsuki, S. (2015). Origin of hysteresis between charge and discharge processes in lithium-rich layer-structured cathode material for lithium-ion battery. *Journal of Power Sources*, *298*, 144-149.

Kubota, Y., Escaño, M. C. S., Nakanishi, H., & Kasai, H. (2007). Crystal and electronic structure of Li 15 Si 4. *Journal of applied physics*, *102*(5), 053704.

Laboni, D. S. M., & Obrovac, M. N. (2015). Li15Si4 formation in silicon thin film negative electrodes. *Journal of the Electrochemical Society*, *163*(2), A255.

Lee, S. W., McDowell, M. T., Choi, J. W., & Cui, Y. (2011). Anomalous shape changes of silicon nanopillars by electrochemical lithiation. *Nano letters*, *11*(7), 3034-3039.

Legerstee, W. J., Noort, T., van Vliet, T. K., Schut, H., & Kelder, E. M. (2022). Characterisation of defects in porous silicon as an anode material using positron annihilation Doppler Broadening Spectroscopy. *Applied Nanoscience*, 1-10.

Legerstee, W. J., Boekel, M., Boonstra, S., & Kelder, E. M. (2021). Scanning probe microscopy facility for operando study of redox processes on lithium ion battery electrodes. *Frontiers in Chemistry*, *9*, 505876.

Li, H., Song, Y., Lu, B., & Zhang, J. (2018). Effects of stress dependent electrochemical reaction on voltage hysteresis of lithium ion batteries. *Applied Mathematics and Mechanics*, *39*(10), 1453-1464.

Liu, X. H., Zheng, H., Zhong, L., Huang, S., Karki, K., Zhang, L. Q., ... & Huang, J. Y. (2011). Anisotropic swelling and fracture of silicon nanowires during lithiation. *Nano letters*, *11*(8), 3312-3318.

Liu, X. H., Fan, F., Yang, H., Zhang, S., Huang, J. Y., & Zhu, T. (2013). Self-limiting lithiation in silicon nanowires. *Acs Nano*, *7*(2), 1495-1503.

Lu, B., Song, Y., Zhang, Q., Pan, J., Cheng, Y. T., & Zhang, J. (2016). Voltage hysteresis of lithium ion batteries caused by mechanical stress. *Physical Chemistry Chemical Physics*, *18*(6), 4721-4727.

Ma, Z., Li, T., Huang, Y. L., Liu, J., Zhou, Y., & Xue, D. (2013). Critical silicon-anode size for averting lithiation-induced mechanical failure of lithium-ion batteries. *Rsc Advances*, *3*(20), 7398-7402.

Maranchi, J. P., Hepp, A. F., & Kumta, P. N. (2003). High capacity, reversible silicon thin-film anodes for lithium-ion batteries. *Electrochemical and solid-state letters*, *6*(9), A198.

McDowell, M. T., Ryu, I., Lee, S. W., Wang, C., Nix, W. D., & Cui, Y. (2012). Studying the kinetics of crystalline silicon nanoparticle lithiation with in situ transmission electron microscopy. *Advanced Materials*, *24*(45), 6034-6041.

McDowell, M. T., Lee, S. W., Nix, W. D., & Cui, Y. (2013). 25th anniversary article: understanding the lithiation of silicon and other alloying anodes for lithium-ion batteries. *Advanced Materials*, *25*(36), 4966-4985.

Melskens, J., Schouten, M., Mannheim, A., Vullers, A. S., Mohammadian, Y., Eijt, S. W., ... & Smets, A. H. (2014). The nature and the kinetics of light-induced defect creation in hydrogenated amorphous silicon films and solar cells. *IEEE Journal of Photovoltaics*, *4*(6), 1331-1336.

Melskens, J., Eijt, S. W., Schouten, M., Vullers, A. S., Mannheim, A., Schut, H., ... & Smets, A. H. (2017). Migration of open volume deficiencies in hydrogenated amorphous silicon during annealing. *IEEE Journal of Photovoltaics*, *7*(2), 421-429.

Obrovac, M. N., & Christensen, L. (2004). Structural changes in silicon anodes during lithium insertion/extraction. *Electrochemical and solid-state letters*, *7*(5), A93.

Obrovac, M. N., Christensen, L., Le, D. B., & Dahn, J. R. (2007). Alloy design for lithium-ion battery anodes. *Journal of The Electrochemical Society*, *154*(9), A849.

Obrovac, M. N., & Krause, L. J. (2006). Reversible cycling of crystalline silicon powder. *Journal of The Electrochemical Society*, *154*(2), A103.

Obrovac, M. N., & Chevrier, V. L. (2014). Alloy negative electrodes for Li-ion batteries. *Chemical reviews*, *114*(23), 11444-11502.

Ogumi, Z., & Inaba, M. (1998). Electrochemical lithium intercalation within carbonaceous materials: intercalation processes, surface film formation, and lithium diffusion. *Bulletin of the Chemical Society of Japan*, *71*(3), 521-534.

Ovejas, V. J., & Cuadras, A. (2019). Effects of cycling on lithium-ion battery hysteresis and overvoltage. *Scientific reports*, *9*(1), 1-9.

Ozanam, F., & Rosso, M. (2016). Silicon as anode material for Li-ion batteries. *Materials Science and Engineering: B*, *213*, 2-11.

Pharr, M., Suo, Z., & Vlassak, J. J. (2014). Variation of stress with charging rate due to strain-rate sensitivity of silicon electrodes of Li-ion batteries. *Journal of Power Sources*, *270*, 569-575.

Placke, T., Kloepsch, R., Dühnen, S., & Winter, M. (2017). Lithium ion, lithium metal, and alternative rechargeable battery technologies: the odyssey for high energy density. *Journal of Solid State Electrochemistry*, *21*(7), 1939-1964.

Ramakrishna, S., & Jose, R. (2022). Principles of materials circular economy. *Matter*, *5*(12), 4097-4099.

Seo, D. H., Urban, A., & Ceder, G. (2015). Calibrating transition-metal energy levels and oxygen bands in first-principles calculations: Accurate prediction of redox potentials and charge transfer in lithium transition-metal oxides. *Physical Review B*, *92*(11), 115118.

Sethuraman, V. A., Chon, M. J., Shimshak, M., Srinivasan, V., & Guduru, P. R. (2010[a]). In situ measurements of stress evolution in silicon thin films during electrochemical lithiation and delithiation. *Journal of Power Sources*, *195*(15), 5062-5066.

Sethuraman, V. A., Srinivasan, V., Bower, A. F., & Guduru, P. R. (2010[b]). In situ measurements of stress-potential coupling in lithiated silicon. *Journal of the Electrochemical Society*, *157*(11), A1253.

Shenoy, V. B., Johari, P., & Qi, Y. (2010). Elastic softening of amorphous and crystalline Li–Si phases with increasing Li concentration: a first-principles study. *Journal of Power Sources*, *195*(19), 6825-6830.

Shin, H. C., Corno, J. A., Gole, J. L., & Liu, M. (2005). Porous silicon negative electrodes for rechargeable lithium batteries. *Journal of power sources*, *139*(1-2), 314-320.

Uxa, D., Jerliu, B., Hüger, E., Dörrer, L., Horisberger, M., Stahn, J., & Schmidt, H. (2019). On the lithiation mechanism of amorphous silicon electrodes in Li-ion batteries. *The Journal of Physical Chemistry C*, *123*(36), 22027-22039.

Vu, A., Qian, Y., & Stein, A. (2012). Porous electrode materials for lithium-ion batteries–how to prepare them and what makes them special. *Advanced Energy Materials*, *2*(9), 1056-1085.

Wang, H., Wang, X., Xia, S., & Chew, H. B. (2015). Brittle-to-ductile transition of lithiated silicon electrodes: Crazing to stable nanopore growth. *The Journal of chemical physics*, *143*(10), 104703.

Wang, X., Fan, F., Wang, J., Wang, H., Tao, S., Yang, A., ... & Xia, S. (2015). High damage tolerance of electrochemically lithiated silicon. *Nature communications*, *6*(1), 1-7.

Woodard, J. C., Kalisvaart, W. P., Sayed, S. Y., Olsen, B. C., & Buriak, J. M. (2021). Beyond thin films: Clarifying the impact of c-li15si4 formation in thin film, nanoparticle, and porous si electrodes. *ACS Applied Materials & Interfaces*, *13*(32), 38147-38160.

Xie, J., Imanishi, N., Zhang, T., Hirano, A., Takeda, Y., & Yamamoto, O. (2010). Li-ion diffusion in amorphous Si films prepared by RF magnetron sputtering: A comparison of using liquid and polymer electrolytes. *Materials Chemistry and Physics*, *120*(2-3), 421-425.

Zhang, T., Zhang, H. P., Yang, L. C., Wang, B., Wu, Y. P., & Takamura, T. (2008). The structural evolution and lithiation behavior of vacuum-deposited Si film with high reversible capacity. *Electrochimica Acta*, *53*(18), 5660-5664.

Zhao, K., Pharr, M., Wan, Q., Wang, W. L., Kaxiras, E., Vlassak, J. J., & Suo, Z. (2011). Concurrent reaction and plasticity during initial lithiation of crystalline silicon in lithium-ion batteries. *Journal of The Electrochemical Society*, *159*(3), A238.

Zhao, K. J., Li, Y. G., & Brassart, L. (2013). Pressure-sensitive plasticity of lithiated silicon in Li-ion batteries. *Acta Mechanica Sinica*, *29*(3), 379-387.

# CHAPTER FIVE

## *Magnesium transfer between AFM probes and metal electrodes in aqueous alginate electrolytes*

This chapter is based on: Legerstee, W. J., Kiriinya, L., Kwakernaak, M., & Kelder, E. M. (2024). Magnesium Transfer between Atomic Force Microscopy Probes and Metal Electrodes in Aqueous Alginate Electrolytes. *Polymers*, *16*(12), 1615.

# Magnesium transfer between AFM probes and metal electrodes in aqueous alginate electrolytes

## Introduction

Due to the transition to green energy sources, the storage of electrical energy is becoming increasingly important. As a result, the development of lithium ion batteries has been accelerated in the last decade and finds its applications in various devices, from mobile phones and laptops to electric bicycles and vehicles. State-of-the-art commercial Li-ion batteries are approaching their theoretical capacities, and in order to bring these batteries to their practical maximum, solutions are being sought to implement the negative electrode of pure lithium allowing an ultra-high specific anode capacity (3862 $mA.g^{-1}$) [Shen et al. 2018]. Its development is especially complicated by the dendrite-forming property of lithium when it is electrochemically deposited, which after years of research still poses a major safety challenge [Zhang et al. 2019]. Although this development will further increase energy density, the increasing demand for energy storage solutions is a direct result of the energy transition and will lead to a shortage of the limited raw materials needed to assemble lithium-based batteries in the near future. In addition, a number of disadvantages of lithium-based batteries, such as high costs and fire hazard, give a significant impetus to the development of new types of batteries. As a result, scientists are looking for alternatives to lithium as an energy carrier, with special attention to the possibilities of metals such as sodium, aluminum and magnesium [Biemolt et al. 2020]. The latter two in particular are interesting candidates for use as pure metal electrode because experiments show that neither of them has a strong tendency to develop dendrites during the deposition process [Lin et al. 2015; Matsui 2011]. Of these two lithium alternatives, magnesium has the lowest atomic mass (Mg 24.305, Al 26.982) and the lowest reduction potential after lithium (Li -3 V, Mg -2.37 V, Al -1.68 V). In addition, the volumetric capacity of magnesium is high compared to lithium (Mg 3833 $mAhcm^{-3}$, Li 2046 $mAhcm^{-3}$). These properties together with the high abundance (magnesium is the eighth most abundant element) and the low cost make secondary magnesium batteries an attractive alternative to lithium ion batteries. However, besides the development of high performance electrode materials, the challenges for Mg-based batteries are mainly focused on finding a suitable electrolyte and overcoming the formation of passivation layers on the magnesium electrode. In contrast to the so called Solid Electrolyte Interphase (SEI) that forms on the anode surfaces in lithium ion

batteries, a layer is formed on the metallic magnesium electrode that completely blocks ions [Aurbach et al. 2001]. Preventing the formation of the passivation layer is therefore a crucial factor in the composition of electrolytes for magnesium batteries. The development of nonaqueous electrolytes is hindered by the poor cathode kinetics and the complex chemistry [Salama et al. 2018]. The presence of a very small amount of $H_2O$ in these electrolytes can already de-compose the electrolyte, while on the other hand, recent research shows that the presence of water can improve the kinetics at the cathode [Wang et al. 2017]. These conflicting facts make it interesting to look at aqueous electrolytes and so, involve the presence of water in the electrochemical system of the magnesium battery. The alternative we study here is an aqueous electrolyte based on alginate, a natural hydrophilic polymer extracted from sea-weed. We use this to electrochemically deposit Mg on different substrates. Atomic Force Microscopy (AFM) is then employed to research the reversible deposition of magnesium and to investigate the morphological structure of the deposited magnesium on a local scale. As we have developed and performed with lithium in previous work [Legerstee et al. 2021], we use the probe, the tip of the cantilever, as an active electrode. In the study presented here, the tip of the probe functions as a point source, providing insight into the distribution of the deposited magnesium over an (infinitely) large surface area. We then brought the results under these highly controlled conditions to the macro scale and per-formed stripping and deposition experiments on different substrates.



## Alginate structure

Alginic acid is a polysaccharide that is abundantly available, environmentally friendly, cost effective and nontoxic. It is found in the cell walls of brown algae and is composed of two anionic monomers: (1,4) linked α−L guluronic acid (G) and (1,4) linked β−D−mannuronic acid (M) (Figure 5.1). The carboxyl group in the G−monomer has the same orientation as the hydroxyl group, whereas in the M− monomer the carboxyl group is oriented perpendicular to the hydroxyl group. Alginic acid is well−known for its ability to bind multivalent cations, very efficiently forming alginate hydrogels in aqueous environments (Grant *et al.*, 1973). Upon deprotonation, the negatively charged carboxylate ($COO^-$) can chelate with cations. Multivalent cations can crosslink the alginate polymer chains ultimately, increasing the viscosity of the solution and in most cases resulting in the formation of a hydrogel. Gel formation has been shown to be greatly influenced by the interactions of the G−blocks (Haug *et.al.*, 1965*).* The linkage of two G−monomers creates a cavity, making it an ideal

place (cage) for a multivalent cation to reside. The crosslinking of the G−blocks by multivalent cations creates a tightly held junction, popularly referred to as 'egg−box model' (Haug *et al.*, 1965).

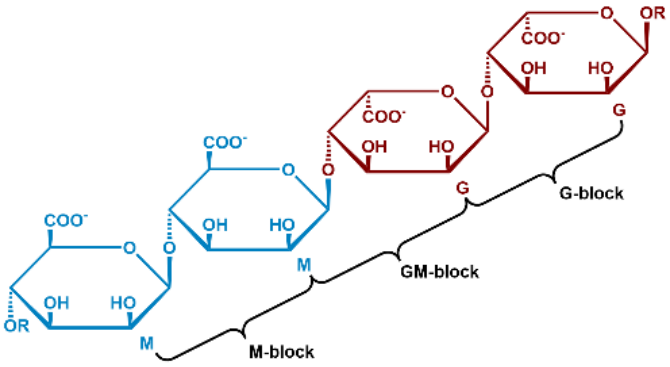


Figure 5.1: Structure of alginate polymers with monomer units mannuronic (M) and guluronic (G).



The binding of the cations to the alginate is influenced by the cation's properties: its charge, affinity to water, ionic radius and chemical affinity with the alginate. Bivalent alkaline earth cations ($Mg^{2+}$, $Ca^{2+}$ and $Sr^{2+}$) typically form ionic bonds. In contrast, bivalent transition metal ions ($Mn^{2+}$, $Co^{2+}$, $Cu^{2+}$, $Fe^{2+}$ and $Zn^{2+}$) and trivalent metal cations ($Fe^{3+}$, $Cr^{3+}$, $Al^{3+}$, $Ga^{3+}$, $Sc^{3+}$ and $La^{3+}$) usually form complex uronates via strong coordination covalent bonds (Brus et al., 2017). Alginate affinity for these bi-valent cations has been shown to increase as follows: Pb > Cu > Cd > Ba > Sr > Ca > Co, Ni, Zn, Mn > Mg (Haug et.al, 1965). Mg-alginate has for a long time been considered as a non-gelling alginate, however studies have found that Mg induces gelation in high G-content polymers with longer gelation times (Topuz et al., 2012). The Mg-alginates gels were however, not stable in water and dissolve fast. The present work investigates the magnesium transfer on micro scale between AFM probes and magnesium metal electrodes followed by macro scale deposition experiments on various substrates in aqueous Mg-alginate electrolyte.

## Magnesium surface reactions

In general, magnesium dissolves in aqueous environments by the following anodic reaction:

$$Mg_{(s)} \rightarrow Mg^{2+}_{(aq)} + 2e^{-} \qquad \text{(Eq 5.1)}$$

Followed by

$$2H_2O_{(l)} + 2e^- \rightarrow H_{2\,(g)} + 2(OH)^-_{(aq)} \quad \text{(Eq 5.2)}$$

Due to the rise of the pH on the magnesium surface, the following reaction forms magnesium hydroxide which can precipitate on the magnesium surface [Core *et al.* 2018]:

$$Mg^{2+}_{(aq)} + 2(OH)^-_{(aq)} \rightarrow Mg(OH)_{2\,(s)} \quad \text{(Eq 5.3)}$$



The result is perceived as a dark layer covering the surface of magnesium [Core *et al.* 2018; Salleh *et al.* 2015].

## Experimental details

### Mg-alginate electrolyte synthesis

Magnesium alginate was synthesised using alginic acid (Alg-acid; VWR International) and magnesium hydroxide ($Mg(OH)_2$ ; Merck Sigma). The Alg-acid powder was first weighed and 20 ml of methanol were added to one equivalent quantity of the Alg-acid. The addition of methanol serves to dissolve the Alg-acid. To deprotonate the Alg-acid, ammonia is added giving a thick slurry. In a separate beaker, $Mg(OH)_2$ was weighed and 5 ml of methanol was added. The mixture was then put in a sonication bath to accelerate the dissolution. The powder was then added to the Alg-acid slurry and stirred for one day at constant temperature of $40^0$C in order to minimize alginate decomposition. After decanting, the residue was air dried for 4 days and then vacuum dried for another 2 days. The vacuum drying process yielded a solid Mg-alginate. The solid Mg-alginate was ball-milled to a powder in a planetary ball mill (Fritsch, Pulverisette 7). The Mg-alginate was crushed in the ball mill for 15 hours at 240 RPM. The resulting Mg-alginate powder (Mg-Alg-P) was used to prepare the electrolyte. In order to do so, 2 w/o Mg-Alg-P was dissolved in water together with 5 w/o NaCl and 5 w/o $MgCl_2{\bullet}6H_2O$, where the $Cl^-$ ions act as the conducting electrolyte ions for charge compensation.

### Sample preparation for deposition and stripping experiments

Deposition experiments have been performed on substrates with a flat surface to avoid a preferred growth of the magnesium on seed-like features at the surface of the sample. As non-magnesium substrate we used single-sided high polished aluminum (Thickness 0.8 mm, Ra<0.05µm). An accurate and flat sample of pure

magnesium has been obtained by means of sputter deposition technique. A silicon wafer (Sigma-Aldrich; <100>, 50.8mm diameter, 0.5mm thickness, semi-conductor grade) was cleaned with acetone and isopropanol and placed into a sputter deposition system (AJA Int. ATC 1800) with a pressure of $<10^{-8}$ mBar and a high purity Mg target (Kurt J.Lesker, 99.95% pure, 2" diameter x 0.25" thick). After plasma cleaning (5 min. in Argon at 20 mBar and RF power of 24 W) a layer of magnesium of 500 nm was applied (26 min. in Argon at 5 mBar and RF power of 100 W). The silicon wafer sputtered with magnesium was then transferred to a glove box in an airtight container and stored there until needed for the experiments.

## Electro-chemical experiments using AFM

In our previous work [Legerstee *et al.* 2021] we described how we used AFM to perform local electrochemical measurements on electrodes of lithium ion batteries at sub-micron to nanoscale. We developed several methods to provide the tip of the AFM probe with a small amount of lithium so that non-faradaic measurements can be performed. In the work presented here, we use one of these techniques, the thin film method, to investigate reversible magnesium deposition between probe tip and substrate with the use of the alginate-based electrolyte.




Figure 5.2: Active probe AFM experiments (a) stripping the substrate and deposit on probe tip, and (b) stripping the probe tip to deposit on substrate.

We used a similar AFM system (NT-NDT NTegra P9) as in our previous study, with the main difference being that this setup is not housed in a protected glovebox environment due to conducting experiments with aqueous solutions. The used AFM has an accessible design for sample handling and is coupled with a galvanostat/potentiostat (Metrohm Autolab PG-STAT302F) to perform the electrochemical experiments between tip and substrate. All deposition experiments with AFM probe as an electrode described here were performed with a diamond-coated conductive probe (Nanosensors GmbH CDT-NCHR with nominal resonance frequency around 400 kHz and nominal force constant around 80 $N.m^{-1}$).

For detecting the presence of magnesium on the probe tip, we used the method described in our previous work [Legerstee *et al.* 2021]. Similarly, in the work presented here, the addition or removal of magnesium to or from the tip was monitored by measuring the resonance frequency of the cantilever after charging or discharging. For that purpose, the probe was lifted from the Mg-alginate film, and the AFM instrument was set in tapping mode. The resonance frequency could be determined automatically by a frequency sweep executed by the oscillating system. Since our goal is a qualitative analysis of the deposition of magnesium, we did not determine the amount of Mg (as we performed in our previous work) but used the resonance shift as an indication to determine whether deposition or stripping has occurred.



The magnesium transfer experiments were performed as shown schematically in Figure 5.2. For deposition to the probe tip, this probe tip was connected as the working electrode and the magnesium substrate as the counter electrode (Figure 5.2a), and vice versa for stripping magnesium from the probe tip to the substrate (Figure 5.2b). Mg-alginate has been applied to the substrate by wipeing a piece of tissue material soaked with Mg-alginate over the surface leaving a thin film on the substrate. The remaining film layer had a thickness between 5 and 8 µm and completely covered the substrate surface. With the AFM setup operating in contact mode, the probe was moved slowly to the surface of the Mg-alginate film while monitoring the moment of bending of the probe accurately with the detector of the laser-reflection signal. As soon as a small deviation of the probe was detected, the approach was immediately stopped, and the distance between sample and probe (z-axis) was manually adjusted to improve the contact between probe tip and electrolyte. When contact between probe tip and electrolyte had stabilized, a bias voltage was applied between tip and substrate to start the deposition process. The deposition was stopped by removing the bias voltage or lifting the tip of the probe from the electrolyte surface.

For the reversable deposition experiment we started with a fresh AFM probe and a flat and unused magnesium sputtered wafer substrate carefully covered with Mg-alginate. After a short deposition time, the presence of a small amount of magnesium on the probe tip was confirmed by the shift in the resonance frequency of the cantilever. The substrate was then rinsed with demi water to remove the Mg-alginate solution and the surface was investigated by AFM in imaging mode. A new substrate was mounted and carefully covered with Mg-alginate for the stripping experiment. Stripping of the tip is achieved by simply reversing the polarity between tip and substrate (Figure 5.2b).

Again, a shift in the resonance frequency of the cantilever was used to determine whether magnesium had been removed from the tip. After detecting a significant shift in the resonance frequency, the substrate was carefully rinsed clean with deionized water and then examined by scanning electron microscopy (SEM).

The deposition results on the substrates were examined using a different probe than used for electrochemical experiments: a more accurate non-conductive probe (Nano sensors PPP-NCHR, Resonance frequency 330 kHz, Force constant 42 N/m, tip radius <10 nm). Scanning electron Microscopy (SEM; JEOL JSM-IT100) and Energy Dispersive Spectroscopy (EDS) was used for investigating the results of deposition on the probe tip.

## Bulk stripping deposition measurements

Figure 5.3 provides a schematic representation of the bulk experiments performed in a dismountable laboratory cell (Figure 5.3c) with high purity magnesium foil (Sigma Aldrich; Purity 99.99%, thickness 0.015 mm) as counter and reference electrode, and the deposition substrate as the working electrode. The electrodes were separated by a porous glass fiber membrane (thickness 0.25 mm) in the first experiments. Because the glass fiber appeared to have an influence on the deposition (see results below), the separator material was removed in follow-up experiments and the spacing was obtained by applying a Teflon ring (thickness 0.25 mm, inner diameter 6 mm) between the layers, as shown in figure 5.3a.



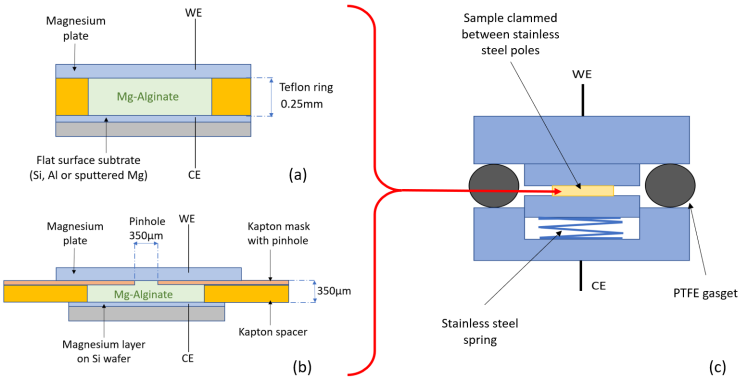


Figure 5.3: Bulk deposition experiments using Mg-alginate as an electrolyte. (a) Mg-alginate is situated between a magnesium plate as working electrode and a flat substrate as the counter electrode where deposition takes place. (b) symmetrical cell with a mask on the stripping side. (c) airtight laboratory cell consisting of separated stainless steel poles. The sample is clamped between the poles and pressed by a stainless steel spring.

To investigate the shape and distribution of the deposition more closely, a symmetrical cell (Mg plate at one side, sputtered Mg substrate on the other side) was provided with an extra mask, as shown in Figure 5.3b. On the working electrode side, an insulating mask (Kapton foil, thickness 50 μm) was provided with a pinhole (d=350 μm) in the middle and stacked together with a separation ring (Kapton spacer, thickness 300 μm) and the deposition substrate (counter electrode).

For stripping/deposition experiments, the laboratory cell was connected to a Maccor™ battery tester (Maccor 4000) which was used under constant current conditions (galvanostatic). Deposition on the substrate side was carried out with a current-density of 100 $\mu A.cm^{-2}$ during 15 minutes, with a fixed potential limit of 0.2 V vs. Mg for all samples. After deposition, the laboratory cells were carefully dismounted and samples were rinsed with demi-water to remove residual alginate on the surface, and followed by drying under vacuum for 30 minutes. After this cleaning procedure, the result of deposition on the sample surface was investigated by SEM. For the non-Mg substrates, the presence of magnesium was confirmed by EDS.



## Results and discussion

### Characterisation of Mg-alginate solutions

Characterization of the various Mg-alginates and Mg-alginate aqueous solutions is done by x-ray diffraction (XRD: X'Pert Pro PANalytical) and Fourier Transform Infrared spectroscopy (FTIR: Thermo Scientific Nicolet iS50 FTIR) which indicates that the solid samples do not contain residual Mg(OH)2 nor alginic acid (Figure 5.4c and 5.4d) (Kwakernaak et al 2025).

### Electrochemical characterisation

The ionic conductivity of the alginate aqueous solutions was measured at different temperatures, as shown in Figure 5.4a. The conductivity for all concentrations of electrolyte generally increases with temperature. The Mg-alginate concentration influences the conductivity strongly which can be understood by the strong dependency of the Mg-ion mobility on the concentration. Hence, the electrolyte conductivity seems to rely more on the ionic mobility than the concentration of the Mg-ions, e.g. addition of more charge carriers (Mg-alginate) does not improve the conductivity of the electrolyte.

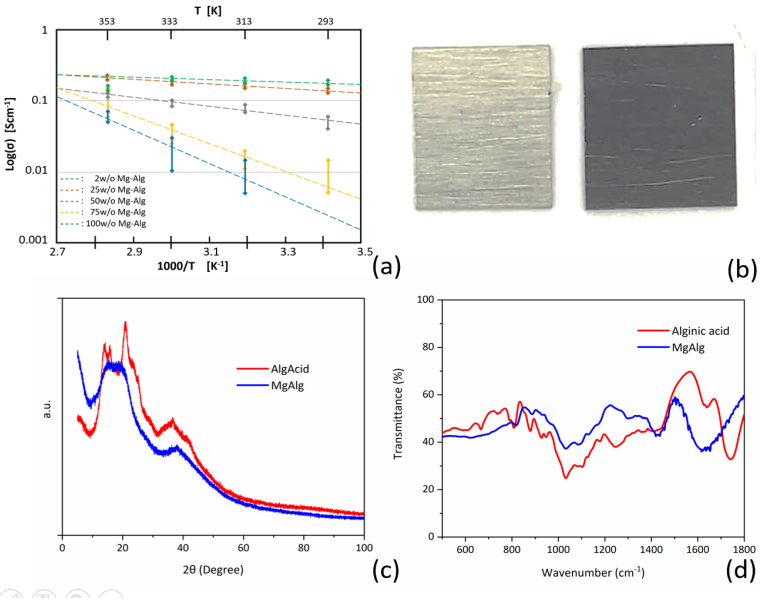


Figure 5.4: (a) Conductivity of electrolytes at different concentrations; (b) Bare magnesium surface compared with surface covered by the black layer after contact with Alginate solution; (c) X-ray diffraction analysis of Alginate Acid (red) and Magnesium Alginate (blue); (d) Fourier Transform Infrared spectroscopy analysis of Alginate Acid (red) and Magnesium Alginate (blue).



The Mg-alginate concentrations with the most promising conductivity (2 wt.% , 25 wt.% and 50 wt. %) were then chosen to perform cyclic voltammetry (CV) and Electrochemical Impedance Spectroscopy (EIS) measurements (Metrohm Autolab PGSTAT12). For characterization, EIS analyses was used to measure the internal resistance of the electrolyte and the interfacial resistance between the electrolyte and the magnesium electrodes. While running EIS and CV a dark layer was observed on the pristine magnesium electrodes (Figure 5.4b). This layer became more apparent with each experiment, and, so, the effect the layer had on the system was investigated. The EIS profiles using 2 w/o (Figure 5.5a), 25 w/o (Figure 5.5b) and 50 w/o (Figure 5.5c) show a significant change in the overall impedance. This seems to reduce the charge transfer resistance causing a subsequent reduction in the impedance but introduces a new process with its own time constant, which was clearly seen by the additional semicircle formed in the high frequency range (Figure 5.5a,b,c).

In Figure 5.5c, 5.5d and 5.5e, the CV curves for 2w/o , 25 w/o and 50 w/o are presented, respectively. Before formation of the black layer, the CV shows a low cycling efficiency due to the high impedance. After the formation of the black layer,

the impedance reduces causing the cycling efficiency to be improved. However, it looks like it is limited by the number of charge carriers. The same behavior is seen in Figure 5.5d, where cycling efficiency improves after the formation of the black layer. The CV curve for 25 w/o electrolyte however, does not seem to be affected by electronic conduction since the electrolyte contains more charge carriers. Figure 5.5f (black curve, before formation of black layer) presents a very low cycling efficiency due to the high impedance (see Figure 5.5c). The formation of the black layer does not seem to significantly improve the efficiency due to increased interfacial and charge transfer resistances (see Figure 5.5c).



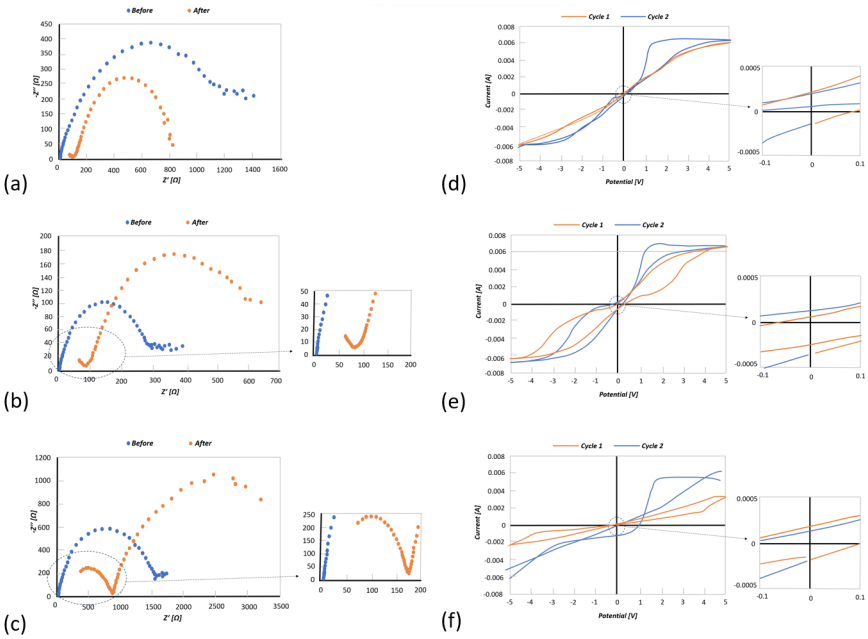


Figure 5.5: (a) EIS results for the 2 wt.% Mg-alginate electrolyte before (blue) and after (red) forming of the black layer; (b) EIS results for the 25 wt.% Mg-alginate electrolyte before (blue) and after (red) forming of the black layer; (c) EIS results for the 50 wt.% Mg-alginate electrolyte before (blue) and after (red) forming of the black layer; (d) CV curve for 2 wt.% Mg-alginate electrolyte before (blue) and after (red) forming of the black layer; (e) CV curve for 25 wt.% Mg-alginate electrolyte before (blue) and after (red) forming of the black layer and; (f) CV curve for 50 wt.% Mg-alginate electrolyte before (blue) and after (red) forming of the black layer.

### Electrochemical deposition of magnesium using an AFM probe as an electrode

Magnesium deposition on the probe tip has been performed as shown in Figure 5.2a. It should be noted that the performance of this process strongly depends on both the ion current and the contact area with the electrolyte. The latter is practically indeterminable in advance because the interaction between the probe tip and the electrolyte surface is influenced by a number of interdependent or variable parameters, such as, for example, the capillary forces between tip and liquid, the viscosity of the electrolyte, the deflection of the cantilever, and the setpoint of the control loop of the AFM. Therefore, the correct settings were searched for by trial and error until the right conditions occurred and the probe tip was deposited in the desired manner with magnesium. Figure 5.6a and b indicate two extremes of the deposition on the probe tip. Figure 5.6a shows the situation when the probe has landed on the electrolyte with a very sensitive adjustment so that the tip just touches the electrolyte and is not adjusted further. Only a small part of the liquid is in contact with the tip, resulting in a deposition of magnesium as a cone-shaped structure. This formation can be understood by the wetting of the tip, the deposition rate of magnesium and the exhausting of $Mg^{2+}$ ion in the solution in the formed cone at the tip as depicted in the schematic drawing of Figure 5.6a. It further proofs that the deposition must be indeed metallic magnesium, else electrons would not find their way to the rim of the cone. Figure 5.6b shows the situation when the probe has sunk just too deep into the electrolyte, with part of the cantilever in contact with the liquid. The deposition in the SEM photo shows complete coverage of the cantilever and the tip. Figure 5.6c shows the desired situation where the tip has just broken through the liquid surface and deposition only takes place at the end of the probe tip. Once this situation has been achieved, subsequent depositions can be reproduced with similar settings.

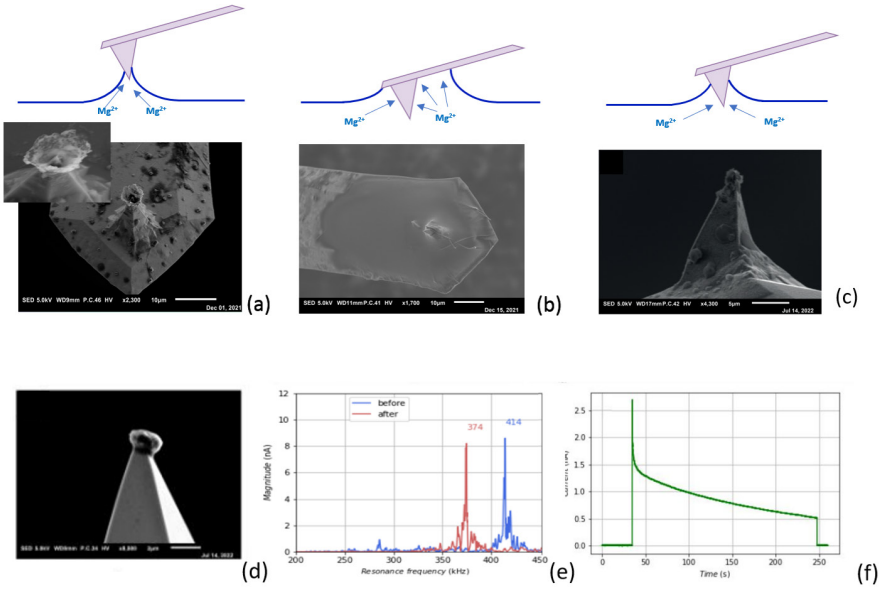


Figure 5.6: finetuning of the AFM settings for optimal deposition of Mg on the very end of the probe tip. (a) very small electrolyte contact aera results in cone form Mg deposition. Inset: cone in detail (up) and a schematical impression on how the Mg cone is growing due to exhausting of Mg2+ ions; (b) electrolyte contact area covers part of the cantilever which results in overall coverage of Mg on the cantilever; (c) Right settings resulting in a deposition on the tip-end; (d) subsequent deposition with the same settings as figure c; (e) shift of the resonance frequency of the cantilever caused by deposition of the tip; (f) registration of the current during deposition.

The AFM settings as used for the deposition of Figure 5.6c appear to give the best results and are also reproducible, as can be seen in one of the subsequent depositions with these settings (Figure 5.6d). Figure 5.6e shows a graph of the resonance frequency of the cantilever before and after deposition and Figure 5.6f shows the measurement of the current be-tween tip and substrate. Both indicate a successful deposition during the experiment.

AFM offers good opportunities to take a closer look at the morphological structure of a deposit, because the tip of the probe can be regarded as a point source. Deposition on the tip will result in a freely positioned spherical shape that can be viewed all around with SEM. To obtain an impression of the morphological structure of deposited magnesium when using Mg-alginate electrolyte, a long-term magnesium deposition was performed as can be seen in Figure 5.7a. For comparison, we have shown a similar deposition with lithium in Figure 5.7b (taken from our previous study: Legerstee et al. 2021).

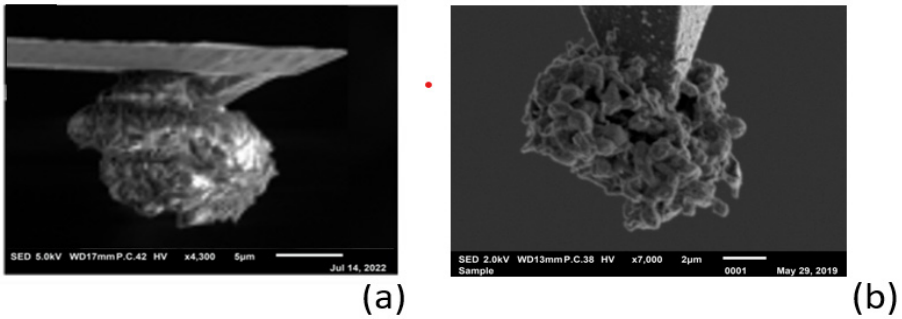


Figure 5.7: (a) Large amount of magnesium deposited on the tip; (b) Lithium deposition on the tip [Legerstee et al. 2021]

The difference in deposition morphologies between lithium and magnesium can be clearly seen on side view SEM pictures of the probe tip: Figure 5.7a shows a spherical massive magnesium deposit with a compact dendrite free structure, while in Figure 5.7b the lithium deposit shows a porous and dendrite-shaped spherical structure. These experimental findings are theoretically supported by modeling and DFT calculations in the work of Markus Jäckle and co-authors [Jäckle *et al.* 2018; Jäckle & Groß, 2014], which describes how magnesium tends to smooth surface growth because it exhibits lower diffusion barriers than lithium. The dendrite formation that occurs with electrodeposition of lithium is also influenced by the electrode/electrolyte interface upon long-term cycling. However, since the origin of dendrite formation is based on the characteristic differences between Li and Mg with regard to elemental properties relevant for growth, it can be concluded that the properties of the electrolyte in the case of magnesium do not significantly influence dendrite growth.



### Reversable magnesium deposition between probe tip and substrate

In our previous study [Legerstee et al. 2022] we have seen that it is not possible to electrochemically remove (strip) lithium from a shape in dendrite structure (as shown in Figure 5.7b). Inspection by SEM showed that the magnesium deposited on the tip has a dense structure without any dendrite formation which allows for reversible magnesium deposition. First, magnesium was taken from the substrate and deposited on the probe tip as schematically shown in Figure 5.2a. After this experiment the surface of the substate was scanned by AFM using the accurate probe that was selected for surface investigation. The image of Figure 5.8a shows the spot where the magnesium was taken during the experiment. Obviously, as can be seen

in this picture, is that magnesium is taken from a very small area, the size of which is comparable to the size of the probe tip. The probe with magnesium deposited on the tip was used for further experiments. Stripping of magnesium from the probe tip was performed as schematically shown in Figure 5.2b. Figure 5.8b shows an image of the magnesium feature which was electrochemically removed from the probe tip and deposited on the substrate. Again, the size and shape of the deposited material has the same dimensions as the probe tip, meaning that the ion current follows a very straight path through the electrolyte. Figure 5.8c gives the shift of the resonance frequency of the probe cantilever measured in tapping mode after each experiment. Although the distortion of the peak makes it difficult to determine the precise shift, the clearly discernible change in resonance frequency gives a good indication of the addition and removal of mass at the tip. This experiment clearly shows that reversible deposition of magnesium with an aqueous Mg-alginate based electrolyte is possible.



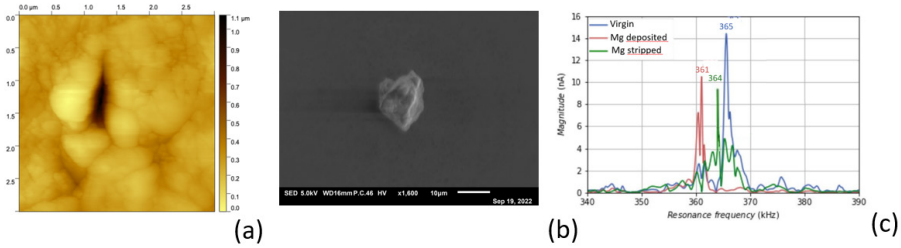


Figure 5.8: deposition and stripping experiment. (a) AFM image of ; (b) SEM picture of ; (c) Shift of Resonance frequency

## Electro chemical magnesium deposition on bulk level

The results of the AFM experiments on a sub-micron scale give reason to perform magnesium deposition on a macro scale as described in Figure 5.3. Figure 5.9 shows SEM pictures of the deposition of Mg on substrates of aluminum (Figure 5.9a) and Silicon (Figure 9b). The experiment on aluminum (Figure 5.9a) was performed using a glass fiber separator between substrate and stripping target. Due to the relatively high energy of the SEM electron beam used (20 keV), the seed on which the magnesium has deposited is visible inside the particle. To avoid the preferred deposition on a seed-like feature, further experiments were performed using the cell configuration of Figure 5.3a, where the separator material was replaced by a Teflon spacer. Figure 5.9b shows the apparently random deposition on a silicon substrate where magnesium appears to have a slight preference for clumping or accumulating on previously deposited material.

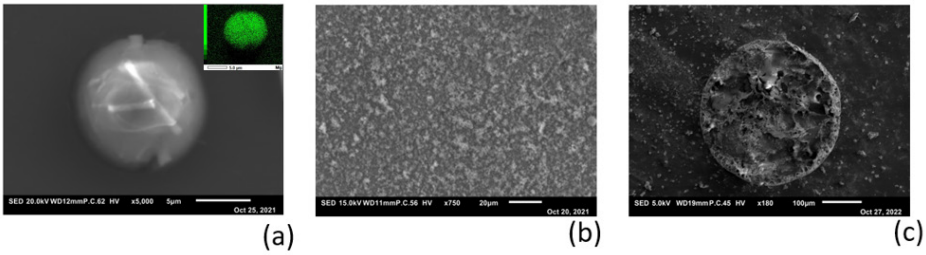


Figure 5.9: Deposition of Mg on different substrates with use of aqueous Mg-alginate electrolyte: (a) SEM picture of Mg on polished aluminum substrate. Inside the spherical particle a small piece of glass fiber from the separator is visible, which acted as a seed for deposition. The inset image shows the EDX scanning result for Mg ; (b) SEM picture of Mg on Silicon wafer. Deposition without a separator shows random oriented deposition on the substrate; (c) Mg deposited on sputtered Mg substrate by using a mask with pinhole of 350 µm

To verify the sub-micron-scale findings of Figure 5.8b, where the ion current through the electrolyte appears to follow a very straight path, a macro scale deposition on a flat magnesium substrate was performed using a mask (as schematically show in Figure 5.3b). The SEM image of Figure 5.9c shows the result of this experiment, where the magnesium forms a cylindrical projection of the mask, with the exact size of the pinhole (350 µm). The amount of magnesium that ended up next to the circular deposition is negligibly small.



## General conclusions

In the study described here we focused on the basic and critical phenomena that are needed to develop an alginate based aqueous secondary magnesium battery. The synthesized alginate powder was characterized by XRD and FTIR (figure 5.4c and 5.4d), after which different concentrations of Mg-alginate where dissolved in water and analyzed by EIS and CV. In general, we can conclude that the aqueous Mg-alginate solution shows electrolyte activity. Concentration of 2 w% Mg-alginate in water with ion conductivity of ~1 $mS.cm^{-1}$ was used further for testing.

A black layer forms on the interface between the aqueous Mg-alginate and the magnesium metal anode surface. The results indicate that this layer has a different composition than the $Mg(OH)_2$ normally formed at the interphase of magnesium and water because it does not seem to block Mg ions to and from the metal surface. However, the specific composition of the black layer is not fully understood because it is an amorphous layer. The layer may have a composition consisting

of magnesium, oxygen, carbon, and hydrogen. Further research using specific measuring techniques is required to characterize the precise composition of the layer. The black layer does not appear to have any adverse effect and may act as a passivation layer for the magnesium surface. Further research into this ion-permeable passivation layer and the contribution and necessity of the alginate in its formation is recommended.

We have successfully created an active AFM probe by providing the probe tip with metallic magnesium. With this active probe it is possible to apply controlled magnesium to a substrate by means of electrochemical deposition. Electrochemical deposition of magnesium using Mg-alginate electrolyte has been demonstrated. Because the AFM probe can be considered as an electrode point source with respect to the 2D infinite and plate-shaped electrode substrate, it was possible to analyze the deposition of magnesium both on the tip and on the substrate. These measurements provide insight into the way in which magnesium ions are transported through the alginate electrolyte. It appears that the magnesium has a strong preference for taking the shortest path, as evidenced by the shapes on both from stripping and deposition on the substrate (Figure 5.8a and 5.8b). The magnesium forms solid structures unlike lithium where unwanted dendrite formation occurs.



The strong preference for a non-dendritic morphology of magnesium provides good opportunities to use this deposition/stripping method for measuring ion current, which we showed in this work with a qualitative current signal (Figure 5.6f). It also opens the way for future experiments to perform non-faradaic impedance measurements on a local scale. Unlike with the use of lithium as we investigated in our earlier work [Legerstee et al. 2021], an AFM probe can be provided with a small amount magnesium in a relatively simple electrodeposition process. This makes it technically less complicated to measure the ion current while scanning over a surface with a magnesium containing probe tip, and thus to create an active-probe AFM image. The development of this 2D ion current scanning probe method creates a new and powerful analysis technique in the palette of AFM based measuring techniques. With advanced AFM equipment, cathode materials can be investigated in this way in scanning mode, providing insight into the relationship between the ion current and the morphology of the electrode material.

# References


Aurbach, D., Gizbar, H., Schechter, A., Chusid, O., Gottlieb, H. E., Gofer, Y., & Goldberg, I. (2001). Electrolyte solutions for rechargeable magnesium batteries based on organomagnesium chloroaluminate complexes. *Journal of the Electrochemical Society*, *149*(2), A115.

Biemolt, J., Jungbacker, P., van Teijlingen, T., Yan, N., & Rothenberg, G. (2020). Beyond lithium-based batteries. *Materials*, *13*(2), 425.

Brus, J.; Urbanova, M.; Czernek, J.; Pavelkova, M.; Kubova, K.; Vyslouzil, J.; Abbrent, S.; Konefal, R.; Horský, J.; Vetchy, D.; et al. Structure and Dynamics of Alginate Gels Cross−Linked by Polyvalent Ions Probed via Solid State NMR Spectroscopy. *ACS Biomac.* **2017**, *18*, 2478–2488. https://doi.org/10.1021/acs.biomac.7b00627

Gore, P., Raja, V. S., & Birbilis, N. (2018). Use of sodium bicarbonate as a chloride-free aqueous electrolyte to explore film formation and the negative difference effect on pure magnesium. *Journal of the Electrochemical Society*, *165*(13), C849.

Grant, G.T.; Morris, E.R.; Rees, D.A.; Smith, P.J.C.; Thom, D. Biological interactions between polysaccharides and divalent cations: The Egg−box model. *FEBS Lett.* **1973**, *32*, 195–198. https://doi.org/10.1016/0014−5793(73)80770−7.

Haug, A.; Smidsrod, O.A.; Larsen, B.; Gronowitz, S.; Hoffman, R.A.; Westerdahl, A. The Effect of Divalent Metals on the Properties of Alginate Solutions. II. Comparison of Different Metal Ions. *Acta Chem. Scand.* **1965**, *19*, 341–351. https://doi.org/10.3891/ACTA.CHEM.SCAND.19−0341.

Jäckle, M., Helmbrecht, K., Smits, M., Stottmeister, D., & Groß, A. (2018). Self-diffusion barriers: possible descriptors for dendrite growth in batteries?. *Energy & Environmental Science*, *11*(12), 3400-3407.

Jäckle, M., & Groß, A. (2014). Microscopic properties of lithium, sodium, and magnesium battery anode materials related to possible dendrite growth. *The Journal of chemical physics*, *141*(17), 174710.

Kurosawa, R., Takeuchi, M., & Ryu, J. (2021). Fourier-transform infrared and X-ray diffraction analyses of the hydration reaction of pure magnesium oxide and chemically modified magnesium oxide. *RSC Adv.*, 11(39), 24292–24311. https://doi.org/10.1039/D1RA04290D

Kwakernaak, M. C., Kiriinya, L. K., Legerstee, W. J., Berghmans, W. M., Hofman, C. G., & Kelder, E. M. (2025). Magnesium Alginate as an Electrolyte for Magnesium Batteries. *Batteries*, *11*(1), 16.

Legerstee, W. J., Boekel, M., Boonstra, S., & Kelder, E. M. (2021). Scanning Probe Microscopy Facility for Operando Study of Redox Processes on Lithium ion Battery Electrodes. *Frontiers in Chemistry*, *9*, 505876.

Lin, M. C., Gong, M., Lu, B., Wu, Y., Wang, D. Y., Guan, M., ... & Dai, H. (2015). An ultrafast rechargeable aluminium-ion battery. *Nature*, *520*(7547), 324-328.

**Matsui, M. (2011).** Study on electrochemically deposited Mg metal. *Journal of Power Sources*, *196*(16), 7048-7055.

**Salama, M., Attias, R., Hirsch, B., Yemini, R., Gofer, Y., Noked, M., & Aurbach, D. (2018).** On the feasibility of practical Mg–S batteries: practical limitations associated with metallic magnesium anodes. *ACS applied materials & interfaces*, *10*(43), 36910-36917.

**Salleh, S. H., Thomas, S., Yuwono, J. A., Venkatesan, K., & Birbilis, N. (2015).** Enhanced hydrogen evolution on Mg (OH) 2 covered Mg surfaces. *Electrochimica Acta*, *161*, 144-152.

**Shen, X., Liu, H., Cheng, X. B., Yan, C., & Huang, J. Q. (2018).** Beyond lithium ion batteries: Higher energy density battery systems based on lithium metal anodes. *Energy Storage Materials*, *12*, 161-175.

**Wang, F., Fan, X., Gao, T., Sun, W., Ma, Z., Yang, C., ... & Wang, C. (2017).** High-voltage aqueous magnesium ion batteries. *ACS central science*, *3*(10), 1121-1128.

**Zhang, X., Wang, A., Liu, X., & Luo, J. (2019).** Dendrites in lithium metal anodes: suppression, regulation, and elimination. *Accounts of chemical research*, *52*(11), 3223-3232.

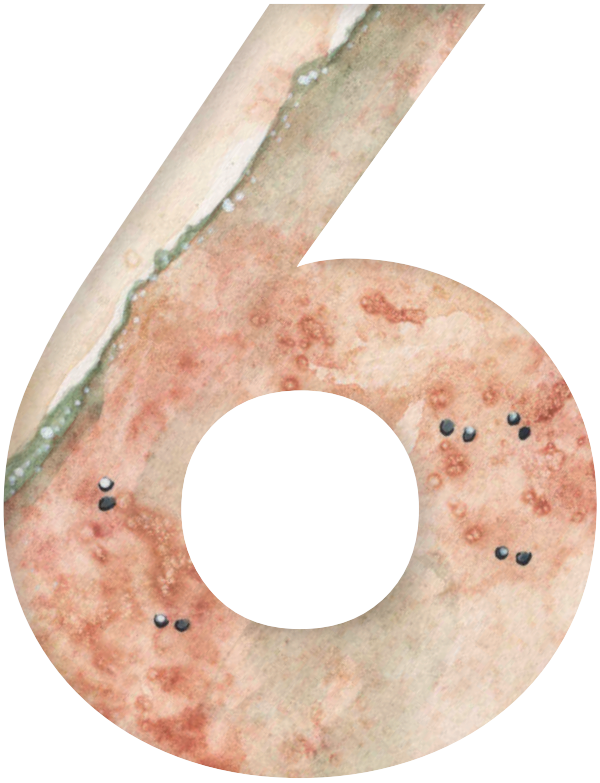

# CHAPTER SIX

*Outlook*

# Outlook

Measuring techniques are the tools that make technical science possible. Expanding this toolbox therefore influences the scope of research and directly determines the possibilities and impossibilities for scientists. The foundation for new measuring techniques and methods often lies with great scientists in history, but once the first successful measurements become reality, many variants and extensions of this discovery often arise, even decades later. It is therefore an honor to be able to expand two techniques, which originated with Nobel Prize winners, with new possibilities and applications.

## SPM

Many variations on the AFM principle have been developed and applied in recent decades, but as far as we know this is the first time a probe has been made part of the measurement in battery research by applying lithium or magnesium on the tip of the AFM probe. The study In this thesis has demonstrated that it is possible to use this technique to perform electrochemical experiments on a sub-micron to nano scale and is able to offer a new addition to operando measurement techniques. Despite the technical difficulties, it has proved possible that the resulting 'active probe' can be used to form a *sub-micron half cell battery* between lithiated tip and sample which can be used for non-faradaic ion current and impedance measurements. In addition, it has been shown that it is possible to accurately determine the amount of lithium at the tip by the shift of the cantilever resonance frequency. Demonstrating the measuring principle shows that a new *electrochemical Active Probe Microscopy* measuring method belongs to the technical possibilities. Developing an automated 2D mapping method in which topographical, ion current and impedance measurements can be performed simultaneously is just around the corner. A manufacturer of AFM equipment can further develop this technology into an automated measuring method. When worked out properly, this *Electrochemical Active Probe Microscopy* measurement-method can be a new operando technique for investigating battery processes on a sub-micron to nano scale.

## DBPAS

Positron annihilation techniques have emerged as valuable tools for investigating the formation of defects in materials. In the studies of chapter 3 and 4 we looked at the contribution this technology could make to the research on alloy forming electrode materials. Among these positron spectroscopy techniques, Doppler

Broadening Positron Annihilation Spectroscopy (DBPAS) was selected for its manageable measurement duration and the availability of beam time at the Variable Energy Positron facility (VEP) at the Reactor Institute Delft. DBPAS is especially useful due to its sensitivity to subtle changes in defect structures, making it possible to gain insights into how defects form and evolve in electrode materials as a result of repeated cycling. A two-material system comprising silicon and lithium was chosen to explore the potential of positron annihilation techniques in understanding defect formation. Silicon, a potential anode material in Li-ion batteries, was examined in this context. Positron annihilation proved to be an effective probe for detecting defects in porous silicon anodes under different lithiation conditions. The positron-electron momentum distribution changed when a new type of defects appeared, enabling precise identification of their origins. However, the relationship between the distribution of electron momentum at the annihilation site and the electrode processes needs to be further investigated. Therefore, additional measurement techniques are needed to complement positron annihilation and provide a more comprehensive understanding of the results.



## Future battery research

In general, both techniques can make a unique contribution to battery research, and thus further improve scientific insights into the complex world of electrochemistry.

The SPM techniques have been applied to both lithium and magnesium based battery systems, but can of course be applied to the entire range of metal ion batteries. In addition, the technology also offers opportunities for application in related areas, such as research into hydrogen fuel cells and redox flow battery systems. SPM techniques can be used to examine fundamental issues related to deposition principles and very local dynamic processes, whereby relationships between morphology and growth processes can be examined in detail.

Positron annihilation techniques offer new insights into the behavior of defects within the bulk of electrode materials, making It a promising method for advancing battery research, particularly in the context of systems where damage occurs as a result of chemical changes, or where the progress of processes has consequences for the defect structure. The technology applied to the lithium-silicon alloy process can be used without changes on alloy anodes for Na-ion batteries because the research questions are virtually the same or are in line with each other. The research described here is only a start in investigating the bulk of a material based on the

positron depth profile. The technique also offers opportunities to distinguish between multiple layers with different *S* and *W* values, or to look even closer to the surface because the progression of the *S* and *W* parameter from the surface to the deeper bulk can also contain useful information. In addition, a related and promising technique of the DBPAS, the Positron Annihilation Lifetime Spectroscopy (PALS), can also be used in the investigations. This technique offers more options with regard to the size of defects and their development in the material. Further studies integrating PAS techniques into their palette of measurement methods will enhance our understanding of the interactions of positrons with battery materials and tell us even more about the role of defects in battery processes.


6

# APPENDICES

# Summary

The use of batteries as an energy carrier has increased enormously in the last decade due to the transition to sustainable energy sources. The rechargeable lithium ion battery with its high energy density is the most commonly used solution for both mobility purposes and stationary energy storage systems. The disadvantages of lithium give reason to look for alternative solutions, such as the Na ion and the Mg ion battery, collectively called metal-ion batteries. These developments require advanced research methods and measurement techniques. In this thesis, two measurement techniques are examined and expanded with new possibilities and insights, expanding the range of measurement techniques for research into metal-ion batteries.

In Chapter 2, new methods and techniques are Investigated to perform advanced measurements on the surface of electrode materials with an Atomic Force Microscope (AFM). The use of scanning probe techniques has been introduced in the last decade in battery research. Until now, Scanning probe microscopy techniques are used to determine surface properties where the moving probe makes full or partial contact with the surface to be examined and the probe as a measuring instrument has as little influence as possible on the surface to be examined during these measurements. However, for electrochemical research it may be desirable for the probe to make an active contribution to the process to be investigated. Therefore, it was examined whether the probe can be provided with a small amount of lithium, so that it becomes part of the electro-chemical process. An Atomic Force Microscope (AFM) is combined with a special designed glovebox system and coupled to a Galvanostat/Potentiostat to allow measurements on electrochemical properties. An open cell design with electrical contacts makes it possible to reach the electrode surface with the cantilever so as to perform measurements during battery operation.

A combined AFM-Scanning Electro-Chemical Microscopy (AFM-SECM) approach makes it possible to simultaneously obtain topological information and electrochemical activity. Several methods have been explored to provide the probe tip with a small amount of lithium. The "wet methods" that use liquid electrolyte appear to have significant drawbacks compared to dry methods, in which no electrolyte is used. Two dry methods were found to be best applicable, with one method applying metallic lithium to the tip and the second method forming an alloy with the silicon of the tip. The amount of lithium applied to the tip was measured by determining the shift of the resonance frequency which makes it possible to follow

the lithiation process. A Finite Element Method (FEM)-based probe model has been used to simulate this shift due to mass change.

The AFM-Galvanostat/Potentiostat set-up is used to perform electrochemical measurements. Initial measurements with lithiated probes show that we are able to follow ion currents between tip and sample and perform an electrochemical impedance analysis in absence of an interfering Redox-probe, a so called non-faradaic measurement. The active probe method developed in this way can be extended to techniques in which AFM measurements can be combined with mapping electrochemical processes with a spatial resolution of less than 100 nanometer.

In chapter 3 Positron Annihilation Doppler Broadening Spectroscopy (DBPAS) is presented as a powerful method to analyse the origin and development of defect processes in porous silicon structures. Silicon is a promising negative electrode material due to it's high capacity. The main drawback is the extreme expansion when alloying with lithium. The volume changes cause cracks in the electrode material, resulting in accelerated degradation. Several prepared anodes were lithiated (discharged against $Li^+/Li$) and de-lithiated (charged) with different capacities followed by a distinct treatment procedure and an analysis using the Delft Variable Energy Positron Beam. The results presented here show that we can distinguish two different processes attributed to *(1)* structural changes in silicon as a result of the alloying process, and *(2)* the formation of defects that initiate degradation of the material. The limit at which the porous material can be used for at least the first two cycles without the occurrence of damage can thus be accurately determined by using the DBPAS technique.



The long-term performance and degradation of porous silicon anodes under repeated lithiation and delithiation (cycling) was investigated in chapter 4. Employing X-ray diffraction (XRD) and positron annihilation spectroscopy as complementary measurement techniques, 20 samples where cycled between 5 and 76 times and lithiated to capacities of 1000, 1200, and 1500 $mAh.g^{-1}$, representing 28%, 33.5%, and 42% of silicon's theoretical capacity, respectively. XRD results show an increase in amorphization upon cycling, evidenced by diminishing normalized silicon peak intensities. This is accompanied by a simultaneously decreasing positron S-parameter, which indicates that amorphization results In a decrease in defects. Higher end capacitances show faster amorphization, which may be related to the plastic deformation around the pores that is exacerbated due to mechanical stress.

The study highlights the potential of positron annihilation as an indirect measure of amorphization, although additional techniques are essential to elucidate the complex interactions in silicon cycling.

The methods developed in Chapter 2 are extended and applied to the Mg ion battery in chapter 5. It is shown that magnesium can be electrochemically deposited in aqueous solutions with alginate-based additives to protect the magnesium. Atomic Force Microscopy is used to investigate the morphological structure of magnesium deposits on a local scale, by using the probe – the tip of a cantilever – as an active electrode, during charging and discharging. We showed that deposition on the probe can be performed in a relatively simple manner compared to the lithiation of the probe in chapter 2. With magnesium no dendrite formation occurs, which would hinder the stripping process.

The future of battery research is set to benefit significantly from advanced measurement techniques which is expanded in this thesis with (i) Electrochemical Active Probe Microscopy (EAPM) and (ii) Doppler Broadening Positron Annihilation Spectroscopy (DBPAS). Active Probe Microscopy, which integrates an AFM probe tip as an active element into a measurement, opens up new possibilities for real-time, nanoscale electrochemical measurements, allowing researchers to explore battery dynamics in unprecedented detail. As development continues, automated 2D mapping for simultaneous topography, ion current, and impedance analysis could become a reality, making this method a powerful tool for "operando" studies.

Similarly, DBPAS presents promising potential in monitoring defect evolution in silicon-based anodes. Its sensitivity to minute structural changes provides insight into how defect dynamics unfold during the charging and discharging cycles of lithium-ion batteries. Further development of these techniques, alongside complementary methods, is likely to enhance our understanding of material stability, paving the way for improved battery longevity and performance through deeper knowledge of degradation mechanisms.

# Samenvatting

Het gebruik van batterijen als energiedrager heeft het laatste decennium een enorme vlucht genomen vanwege de transitie naar duurzame energiebronnen. Hierbij is de herlaadbare lithium ion batterij met zijn hoge energie dichtheid de meest gebruikte oplossing voor zowel mobiliteitsdoeleinden als ook stationaire energie opslagsystemen. De nadelen van lithium geven aanleiding om alternatieve oplossingen te zoeken, zoals bijvoorbeeld de Na ion en de Mg ion batterij, samenvattend metaal-ion batterijen genoemd. Deze ontwikkelingen vragen om geavanceerde onderzoeksmethoden en meettechnieken. In dit proefschrift worden twee meettechnieken onderzocht en uitgebreid met nieuwe mogelijkheden en inzichten waardoor het scala van meettechnieken voor het onderzoek naar metaal ion batterijen wordt vergroot.

In hoofdstuk 2 worden nieuwe methoden en technieken onderzocht om geavanceerde metingen op het oppervlak van elektrodematerialen uit te voeren met een Atomic Force Microscope (AFM). Het gebruik van scanning probe-technieken is het afgelopen decennium geïntroduceerd in batterijonderzoek. Tot nu toe worden scanning probe-microscopietechnieken gebruikt om oppervlakte-eigenschappen te bepalen, waarbij de bewegende probe volledig of gedeeltelijk contact maakt met het te onderzoeken oppervlak en de probe als meetinstrument zo min mogelijk invloed heeft op het te onderzoeken oppervlak. Voor elektrochemisch onderzoek kan het echter wenselijk zijn dat de probe actief bijdraagt aan het te onderzoeken proces. Daarom is onderzocht of de probe kan worden voorzien van een kleine hoeveelheid lithium, zodat deze deel uitmaakt van het elektrochemische proces. Een Atomic Force Microscope (AFM) wordt gecombineerd met een speciaal ontworpen handschoenboxsysteem en gekoppeld aan een galvanostaat/potentiostaat om metingen van elektrochemische eigenschappen mogelijk te maken. Een open celontwerp met elektrische contacten maakt het mogelijk het elektrodenoppervlak met de cantilever te bereiken om metingen tijdens batterijwerking uit te voeren. Een gecombineerde AFM-Scanning Electrochemical Microscopy (AFM-SECM)-benadering maakt het mogelijk om tegelijkertijd topologische informatie en elektrochemische activiteit te verkrijgen. Verschillende methoden zijn onderzocht om de probe-tip te voorzien van een kleine hoeveelheid lithium. De 'natte methoden' die vloeibare elektrolyt gebruiken, hebben aanzienlijke nadelen vergeleken met droge methoden waarbij geen elektrolyt wordt gebruikt. Twee droge methoden bleken het meest toepasbaar: een methode waarbij metallisch lithium op de tip wordt aangebracht en een methode waarbij een legering wordt gevormd met het silicium van de tip. De hoeveelheid lithium

op de tip werd gemeten door de verschuiving in resonantiefrequentie te bepalen, wat het mogelijk maakt om het lithiatieproces te volgen. Een op de Finite Element Method (FEM) gebaseerd probemodel is gebruikt om deze verschuiving als gevolg van massaverandering te simuleren.

De AFM-galvanostaat/potentiostaat-opstelling wordt gebruikt om elektrochemische metingen uit te voeren. Eerste metingen met ge-lithieerde probes tonen aan dat we ionstromen tussen tip en monster kunnen volgen en een elektrochemische impedantie-analyse kunnen uitvoeren zonder een storende redox-probe, een zogenaamde niet-faradaïsche meting. De op deze manier ontwikkelde actieve probemethode kan worden uitgebreid naar technieken waarbij AFM-metingen kunnen worden gecombineerd met het in kaart brengen van elektrochemische processen met een ruimtelijke resolutie van minder dan 100 nanometer.

In hoofdstuk 3 wordt Doppler Broadening Positron Annihilation Spectroscopy (DBPAS) gepresenteerd als een krachtige methode om het ontstaan en de ontwikkeling van defectprocessen in poreuze siliciumstructuren te analyseren. Silicium is een veelbelovend negatief elektrodemateriaal vanwege de hoge capaciteit. Het grootste nadeel is de extreme uitzetting bij legering met lithium. De volumeveranderingen veroorzaken scheuren in het elektrodemateriaal, wat leidt tot versnelde degradatie. Verschillende voorbereide anodes werden gelithieerd (ontladen tegen Li+/Li) en gedelithieerd (opgeladen) met verschillende capaciteiten, gevolgd door een specifieke behandelingsprocedure en een analyse met behulp van de Delft Variable Energy Positron Beam. De hier gepresenteerde resultaten tonen aan dat we twee verschillende processen kunnen onderscheiden, namelijk (1) structurele veranderingen in silicium als gevolg van het legeringsproces en (2) de vorming van defecten die de degradatie van het materiaal initiëren. De grens waarbij het poreuze materiaal ten minste de eerste twee cycli zonder schade kan worden gebruikt, kan met behulp van de DBPAS-techniek nauwkeurig worden bepaald.

De prestaties op lange termijn en de degradatie van poreuze siliciumanodes onder herhaalde lithiation en delithiation (cycli) worden onderzocht in hoofdstuk 4. Door gebruik te maken van röntgendiffractie (XRD) en positron-annihilatiespectroscopie als complementaire meetmethoden werden 20 monsters onderzocht die tussen 5 en 76 keer werden gecycled en gelithieerd tot capaciteiten van 1000, 1200 en 1500 $mAh.g^{-1}$, wat respectievelijk 28%, 33,5% en 42% van de theoretische capaciteit van silicium vertegenwoordigt. XRD-resultaten tonen een toename van amorfisering bij

cycli, wat blijkt uit afnemende genormaliseerde piekintensiteiten van silicium. Dit gaat gepaard met een gelijktijdige afname van de positron *S*-parameter, wat erop wijst dat amorfisering resulteert in een afname van defecten. Hogere eindcapaciteiten tonen snellere amorfisering, wat mogelijk gerelateerd is aan de plasticiteit rond de poriën door mechanische spanningen. Deze studie benadrukt het potentieel van positron-annihilatie als een indirecte maat voor amorfisering, hoewel aanvullende technieken essentieel zijn om de complexe interacties bij siliciumcycli te verduidelijken.

De methoden ontwikkeld in hoofdstuk 2 worden uitgebreid en toegepast op de magnesium-ionbatterij in hoofdstuk 5. Er wordt aangetoond dat magnesium elektrochemisch kan worden afgezet in waterige oplossingen met alginaat-gebaseerde additieven om het magnesium te beschermen. Atomic Force Microscopy wordt gebruikt om de morfologische structuur van magnesiumafzettingen op lokale schaal te onderzoeken door de probe – de tip van een cantilever – als actieve elektrode te gebruiken tijdens het laden en ontladen. We toonden aan dat de afzetting op de probe op een relatief eenvoudige manier kan worden uitgevoerd in vergelijking met de lithiatie van de probe in hoofdstuk 2. Bij magnesium vindt geen dendrietvorming plaats, wat het afstripproces zou bemoeilijken.



De toekomst van batterijonderzoek zal aanzienlijk profiteren van geavanceerde meetmethoden die in dit proefschrift zijn uitgebreid met (i) elektrochemisch actieve probemicroscopie (EAPM) en (ii) Doppler Broadening Positron Annihilation Spectroscopy (DBPAS). Actieve probemicroscopie, die een AFM-probetip als actief element integreert in een meting, opent nieuwe mogelijkheden voor realtime elektrochemische metingen op nanoschaal, waardoor onderzoekers batterijdynamiek in ongekende details kunnen bestuderen. Naarmate de ontwikkeling vordert, kan geautomatiseerde 2D-mapping voor gelijktijdige topografie-, ionstroom- en impedantieanalyse realiteit worden, wat deze methode tot een krachtig instrument maakt voor "operando"-studies.

Evenzo biedt DBPAS veelbelovend potentieel voor het monitoren van defectontwikkeling in siliciumgebaseerde anodes. De gevoeligheid voor kleine structurele veranderingen biedt inzicht in hoe defectdynamiek zich ontvouwt tijdens de laad- en ontlaadcycli van lithium-ionbatterijen. Verdere ontwikkeling van deze technieken, samen met complementaire methoden, zal naar verwachting ons begrip van materiaaleigenschappen verbeteren, wat de weg vrijmaakt voor een langere levensduur en betere prestaties van batterijen door meer inzicht in degradatiemechanismen.

# Acknowledgements

Here I would like to express my gratitude to the people who helped me and contributed in this PHD process. The process that I went through is different from the regular PHD because I did this in addition to my job as a teacher at the Rotterdam University of Applied Sciences. The fragmented workload that arises as a result of combining these two professions made me extra dependent on the help and goodwill of people around me, both professionally and privately. I am therefore very grateful to everyone who has helped me in any way to accomplish this. Below I thank everyone in more or less random order.

First of all I would like to thank my supervisor Erik Kelder for his positive and very pleasant attitude and his experienced scientific insights and discussions towards my project. From the moment I asked if I could complete a PHD program based on a teacher grant, he helped and assisted me with advice and scientific input to draw up a suitable project. Under his supervision I was given all the necessary cooperation and opportunities to complete my PHD trajectory. I would also like to thank Prof. Eckes Bruck for making this process possible within his FAME department. When I asked him whether I could carry out a PHD program at TU Delft, he put me in touch with Erik to draw up a proposal. Eckes also assisted me during the process to comply with the Graduate School formalities in a pragmatic but correct manner. Moreover, his review of the thesis was a useful and important step in completing it. I am extremely grateful for the help Marcel Bus gave me in developing and carrying out AFM experiments, and for his insightful and substantive discussions about the possibilities of applying AFM for electrochemistry. Marcel introduced me to working with an AFM, after which I was technically able to carry out the project. However, during the project I was always able to contact Marcel, after which he enthusiastically helped me to convert the apparent impossibilities into new challenges. Without Marcel, no lithium would have reached the tip of a cantilever through a liquid electrolyte. The support of an enthusiastic technician is important for a project where a facility needs to be adapted in a creative way, and I was lucky that Reinier den Oudsten helped me with this. From adjusting the glovebox to making sample holders and other useful tools, with his technical insight and skills, Reinier made an unthinkably important contribution to my PHD project. I would also like to thank Prof. Marnix Wagemaker for the hospitality of allowing me to work within the SEE group and use the laboratories and instruments. I would also like to thank Frans Ooms for his general technical support, making materials

and equipment available for AFM and EIS measurements inside a glovebox and for his willingness to provide a laboratory introduction to the many students who worked on my project. I am extremely grateful to Henk Schut for his help with the scientific and experimental challenges on positron measurements and analyses, and the scientific discussions we had that lead to the Insights described In this thesis. A number of times I needed thin layers of high quality, Herman Schreuder sputtered great layers of magnesium for me, and Evert Merkx sputtered silicon for my AFM samples, both of which I am very grateful for. I would also like to thank my co-authors Mark Kwakernaak and Lindah Kiriinya for their contribution regarding alginates to the magnesium deposition article, and Fride Vullum-Bruer who gave me a real deep dive into magnesium batteries at the beginning of my PHD. Also many thanks to Sergey Lehmeshko with his outstanding expertise of the AFM instrument I used, and to the company Emagy BV, and especially to Axel Schonecker and Peter Kalisvaart for making the porous silicon material (E-magy™) available for defect research with positrons.



Of course I would like to thank Rotterdam University of Applied Sciences for making this research possible by granting me a PHD voucher. Especially my colleagues from the Automotive study program who have always supported me and Involved me In all kind of projects that contributed to my insights into practical battery applications. I would also like to thank Frank Rieck, who helped me to obtain the necessary contacts and who ensured that my research proposal passed the assessments of the Rotterdam University of Applied Sciences without delay. My special thanks go to Liek Voorbij, the former director of "Kenniscentrum Duurzame Havenstad". With her pragmatic attitude, Liek has helped to create space for conducting scientific research in the everyday hustle and bustle of an educational job on Rotterdam University of Applied Sciences, and understood the value that battery research can have for a practice-oriented knowledge institute. I would also like to thank Annemarieke Lokhorst for organizing the writing retraits, the motivational conversations, and of course the catch-up drinks at all kinds of typical Rotterdam pub locations. At the start of my project I was very grateful with the Input of Jolanda Dwarswaard, who helped me with setting up a successful research proposal that passed the commission without any adjustments.

Last but not least, I would like to thank all students who contributed to this PHD research. In random order: Tjitte Noort, Bram Heijblok, Leonie Michielsen, Mark Boekel, Steven Boonstra, Winok Bergmans, Firos Mohamedhousein, Dionne Breure,

Tobias van Vliet, Annika Zijlstra, Alex Uittenbogaard, Yigit Akpinar, Sven Tesselaar, Tess van Berkum, Michel de Jongh, Tom van Nispen tot Pannerden, Nick Klein, Sander van Haagen, Thomas Wigmans, Bhavya Shetty, Jorick Baljeu, Abe Wieringa and Myrthe Breedijk.

*Constructive cooperation leads to the best results.*

*Thank you all,*

*Walter Legerstee*

# About the Author

Walter Jacob Legerstee was born on the 31th of march 1968 in Delft. He completed high school at the Oranje Nassau Mavo in Delft, after which he followed a mechanical engineering course at the Rijnmond MTS in Schiedam. He studied applied physics at TH Rijswijk, where he obtained his bachelor's degree in 1994. After military service, he started as a researcher in non-destructive measuring methods at Fokker Aircraft Schiphol In 1995, after which he worked from 1996 to 1997 on developing a laser reflection measuring instrument for 3-phase reactors at the 'Bio-process technology' department of the Kluyver laboratory at TU Delft. In 1997 he started as a research technician at inorganic chemistry department TU Delft, where he carried out a feasibility study for the development of a fully ceramic battery on behalf of Shell. Over the next four years he worked on the development of this battery. In 2002 he started as a research engineer at the 'Defects in Materials' department of the Interfaculty Reactor Institute Delft, where he worked on the development of an electrostatic positron beam combined with a scanning electron microscope to perform local in-depth material analyses, after which he worked on hydrogen storage in thin metal layers from 2008 to 2012. After working for a short time as an office manager of an international metal company, he started as a lecturer in the Automotive study program at Rotterdam University of Applied Sciences in 2014. In 2017 he followed the internal workshop for obtaining a PHD voucher, after which he wrote a research proposal for a study in the battery field in collaboration with the FAME department of TU Delft. In May 2018, the research proposal was approved by the PHD committee of Rotterdam University of Applied Sciences, after which he started his PHD program at TU Delft in November 2018 for two days a week, in addition to his job as a lecturer. In January 2024 he has ended his working relationship with Rotterdam University of Applied Sciences, after which he works now as an independent consultant for battery-related issues.

# List of Publications

Related to this Thesis

Legerstee, W. J., Kiriinya, L., Kwakernaak, M., & Kelder, E. M. (2024). Magnesium Transfer between Atomic Force Microscopy Probes and Metal Electrodes in Aqueous Alginate Electrolytes. *Polymers*, *16*(12), 1615.

Legerstee, W. J., Noort, T., van Vliet, T. K., Schut, H., & Kelder, E. M. (2022). Characterization of defects in porous silicon as an anode material using positron annihilation Doppler Broadening Spectroscopy. *Applied Nanoscience*, *12*(11), 3399-3408.

Legerstee, W. J., Boekel, M., Boonstra, S., & Kelder, E. M. (2021). Scanning probe microscopy facility for operando study of redox processes on lithium ion battery electrodes. *Frontiers in Chemistry*, *9*, 505876.

Legerstee, W., & Kelder, E. (2018). In-situ and operando Scanning Probe Facility for the study of redox processes on nanometer scale in Lithium Ion batteries-First measurement results for in situ and operando characterisation of Lithium Ion Batteries by AFM techniques. In *31st International Electric Vehicle Symposium and Exhibition, EVS 2018 and International Electric Vehicle Technology Conference 2018, EVTeC 2018*.

Not related to this Thesis

Kwakernaak, M. C., Kiriinya, L. K., Legerstee, W. J., Berghmans, W. M., Hofman, C. G., & Kelder, E. M. (2025). Magnesium Alginate as an Electrolyte for Magnesium Batteries. *Batteries*, *11*(1), 16.

Legerstee, W. J., De Roode, J., Anastasopol, A., Falub, C. V., & Eijt, S. W. H. (2012). In-situ hydrogen sorption 2D-ACAR facility for the study of metal hydrides for hydrogen storage. *Physics Procedia*, *35*, 22-27.

Vons, V. A., Anastasopol, A., Legerstee, W. J., Mulder, F. M., Eijt, S. W. H., & Schmidt-Ott, A. (2011). Low-temperature hydrogen desorption and the structural properties of spark discharge generated Mg nanoparticles. *Acta Materialia*, *59*(8), 3070-3080.

Vons, V. A., Leegwater, H., Legerstee, W. J., Eijt, S. W. H., & Schmidt-Ott, A. (2010). Hydrogen storage properties of spark generated palladium nanoparticles. *International journal of hydrogen energy*, *35*(11), 5479-5489.

Vons, V. A., Schmidt-Ott, A., Leegwater, H., Legerstee, W. J., & Eijt, S. W. H. (2010). Spark production of magnesium nanoparticles for hydrogen storage. In *World Congress on Particle Technology* (pp. 1-4). NurnbergMesse.

Eijt, S. W. H., Kind, R., Singh, S., Schut, H., Legerstee, W. J., Hendrikx, R. W. A., ... & Dam, B. (2009). Positron depth profiling of the structural and electronic structure transformations of hydrogenated Mg-based thin films. *Journal of Applied Physics*, *105*(4).

Vons, V. A., Leegwater, H., Legerstee, W., Eijt, S., & Schmidt-Ott, A. (2009). Coated highly porous metal hydride nanoparticle layers for hydrogen storage. In *EAC 2009*.

Vons, V. A., Leegwater, H., Legerstee, W. J., Eijt, S. W. H., & Schmidt-Ott, A. (2009). Production of metallic magnesium using spark discharge. In *EAC 2009*.

Nanu, D. E., Legerstee, W. J., Eijt, S. W. H., Haije, W. G., Vente, J. F., Tucker, M. G., & Böttger, A. J. (2008). Insights into the relation between crystal structure and deuterium desorption characteristics of Pd–Au–D alloys. *Acta materialia*, *56*(20), 6132-6140.

Vons, V. A., Eijt, S., Legerstee, W. J., & Schmidt-Ott, A. (2008). Coated highly porous nanoparticle layers for hydrogen storage. In *NSM Science Day*.

Singh, S., Eijt, S. W. H., Zandbergen, M. W., Legerstee, W. J., & Svetchnikov, V. L. (2007). Nanoscale structure and the hydrogenation of Pd-capped magnesium thin films prepared by plasma sputter and pulsed laser deposition. *Journal of alloys and compounds*, *441*(1-2), 344-351.

Singh, S., Eijt, S. W., Zandbergen, M. W., & Legerstee, W. J. (2007). VL Svetchnikov J. *Alloys Comp*, *441*, 344-351.

Singh, S., Eijt, S. W. H., Zandbergen, M. W., Legerstee, W. J., Schut, H., & Svetchnikov, V. (2005). Phase transformations and nanoscale structure of magnesium hydride. In *WWF-DISE Seminar" Natuur en nieuwe energie-werken aan een kansrijk klimaat"*.

Zandbergen, M. W., Eijt, S. W. H., Legerstee, W. J., Schut, H., & Svetchnikov, V. L. (2004). Nano-Columnar Mg Thin Films Created by Plasma Sputter Deposition for Improved Hydrogen Kinetics and Storage Properties. *MRS Online Proceedings Library (OPL)*, *837*, N1-3.

Abadjieva, E., Schut, H., van Veen, A., & Legerstee, W. J. (2001, July). An electrostatic variable-energy positron beam for Re-moderation experiments. In *Materials Science Forum* (Vol. 363).

Legerstee, W. J., & van Veen, A. (2001). Characterisation of high strength steels from Nedsteel by hydrogen permeation.

Jak, M. J., Ooms, F. G., Kelder, E. M., Legerstee, W. J., Schoonman, J., & Weisenburger, A. (1999). Dynamically compacted all-ceramic lithium-ion batteries. *Journal of power sources*, *80*(1-2), 83-89.

Jak, M. J. G., Kelder, E. M., van Landschoot, R. N., Legerstee, W. J., & Ooms, F. G. B. (1998). Magnetic pulse compacted wound Li-ion batteries, periodic report 1/9-31/12/98.